Fall 2019

Application of Halloysite Nanotubes in Bone Disease Remediation and Bone Regeneration

Yangyang Luo

APPLICATION OF HALLOYSITE NANOTUBES IN BONE DISEASE REMEDIATION AND BONE REGENERATION

by

Yangyang Luo, M.S.

A Dissertation Presented in Partial Fulfillment
of the Requirements of the Degree
Doctor of Philosophy

COLLEGE OF ENGINEERING AND SCIENCES
LOUISIANA TECH UNIVERSITY

November 2019

LOUISIANA TECH UNIVERSITY

THE GRADUATE SCHOOL

Date

We hereby recommend that the dissertation prepared under our supervision by

Yangyang Luo M.S.

entitled **Application of Halloysite Nanotubes in Bone Disease Remediation and Bone Regeneration**

be accepted in partial fulfillment of the requirements for the Degree of

Doctor of Philosophy in Molecular Science and Nanotechnology

David K. Mills, Supervisor of Dissertation Research

Gergana Nestorova
Head of Molecular Sciences and Nanotechnology

Members of the Doctoral Committee:
Rebecca Giorno
William Wolf
Teresa A. Murray
Steven A. Jones

Approved:

Hisham Hegab
Dean of Engineering & Science

Approved:

Ramu Ramachandran
Dean of the Graduate School

GS Form 13a
(10/18)

ABSTRACT

Customized patient therapy has been a major research focus in recent years. There are two research fields that have made a significant contribution to realizing individualized-based treatment: targeted drug delivery and three-dimensional (3D) printing technology. With benefit from the advances in nanotechnology and biomaterial science, various drug delivery systems have been established to provide precise control of therapeutic agents release in time and space. The emergence of three-dimensional (3D) printing technology enables the fabrication of complicated structures that effectively mimic native tissues and makes it possible to print patient-specific implants. My dissertation research used a clay nanoparticle, halloysite, to develop a drug delivery system and 3D scaffold which may contribute to individualized-based treatment.

Halloysite nanotubes (HNTs) are naturally occurring tubular nanoparticles with a hollow lumen. They possess a high aspect ratio, thermal stability, and unique oppositely charged inner and outer surfaces. These inherent features enable them to be used as a bulk filler to improve the performance characteristics of many polymers. Besides, HNTs are biocompatible and have a demonstrated capacity to delivery growth factors, RNA, DNA and other chemical substances; therefore, HNTs have received extensive attention in the development of drug delivery systems. In this dissertation, HNTs were applied in the development of medical devices for bone disease remediation, tissue regeneration, and restoration of bone function.

Osteomyelitis is a bone infection and mainly caused by *Staphylococcus aureus (S. aureus)*. Gentamicin is the antibiotic commonly used to against gram- negative and positive bacteria, which includes *S. aureus*. When gentamicin was loaded into HNTs and incorporated with chitosan, the hybrid chitosan/HNTs hydrogels provided a sustained drug release and successfully inhibited the growth of *S. aureus*. Simultaneously, the addition of HNTs improved chitosan mechanical properties.

Osteosarcoma is the most common cancer tumor occurring in bone tissue. Through surface modification, HNTs were conjugated with folic acid and fluorochrome (FITC). The bi-functionalized HNTs (bHNTs) were then doped with anticancer drugs, methotrexate (MTX). MTX-doped bHNTs showed a high drug loading efficiency and selectively targeted cancer cells. MTX-loaded bHNTs efficiently inhibited osteosarcoma proliferation without harm to normal type cells (pre-osteoblasts).

Osteoporosis is the most common bone disease as the bone formation fails to keep up with the bone resorption rate. Bone fractures happen as a result of long-term bone defection. Three dimensional printed scaffolds that support bone regeneration could be a viable alternative to bone grafting, which is limited by insufficient supplies and issued with infection. Metal-doped HNTs were combined with PLA and printed with a specific pore size and porosity design. After surface modification, 3D printed HNTs/PLA scaffolds encouraged cell adhesion and osteogenic differentiation. Furthermore, surface coating of gentamicin had a long stock life to inhibit bacterial growth and promoted osteogenesis.

APPROVAL FOR SCHOLARLY DISSEMINATION

The author grants to the Prescott Memorial Library of Louisiana Tech University the right to reproduce, by appropriate methods, upon request, any or all portions of this Dissertation. It is understood that "proper request" consists of the agreement, on the part of the requesting party, that said reproduction is for his personal use and that subsequent reproduction will not occur without written approval of the author of this Dissertation. Further, any portions of the Dissertation used in books, papers, and other works must be appropriately referenced to this Dissertation.

Finally, the author of this Dissertation reserves the right to publish freely, in the literature, at any time, any or all portions of this Dissertation.

Author ______________________________

Date ______________________________

TABLE OF CONTENTS

LIST OF FIGURES

ACKNOWLEDGMENTS

First and foremost, I would like to thank my super advisor Dr. David Mills. He has given me many suggestions regarding my research and offered me the opportunities to learn the instruments and technologies that advanced my dissertation research.
Dr. Mills gave me enough space to develop my own ideas. He is always patient to teach me skills I need and help to improve my problem-solving ability. Without his support and guidance, I could not have completed this work.

Second, I want to express my heartfelt thanks to all my great labmates, colleagues and professors. I am particularly grateful to Dr. Kevin Holly, Ahmed Humayun, Xuan Liu, Ben Kemp, Mengcheng Liu, Antwine W. McFarland JR, Anusha Elumulai, and Mychal Miller. I have received invaluable help from you all.

Finally, I would like to extend my deep gratefulness to my parents. They always encouraged me to archive my goals, and they have always supported me every decision I have made. They are my strongest advocates.

CHAPTER 1

INTRODUCTION

1.1 Halloysite Nanotubes

1.1.1 Halloysite Nanotube Structure

Halloysite was first discovered in Belgium and received substantial research interests as a mineral material in the 1940s [1]. Since 2012, it has gained increased attention due to its nano size hollow tubular structure. Halloysite is aluminosilicate clay ($Al_2Si_2O_5(OH)_4nH_2O$), it naturally folded to form nanotubes. Halloysite nanotubes (HNTs) are multi walls consisted by octahedrally coordinated Al^{3+} and tetrahedrally coordinated Si^{4+} in a 1:1 stoichiometric ratio [2]. The particle size of HNTs is 0.5-2 μm in length with an inner diameter of 10-30nm and external diameter of 50-70nm [2]. As **Figure 1-1** shows, aluminons are folded inside towards the lumen, while siloxanes are exposed on the outer surface; therefore, the lumen of HNTs are positively charged, while the external surface of HNTs are negatively charged.

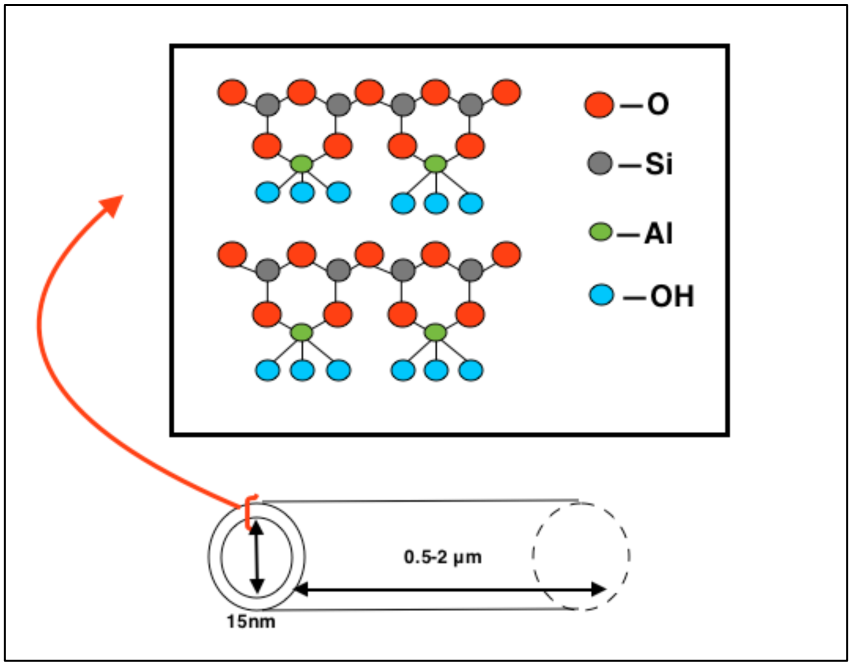

Figure 1-1: Halloysite nanotubes structure. The tubular structure formed by the conjunction of silicone dioxide and aluminum oxide layers.

Due to its high aspect ratio, hollow tubular structure, and different charges of inner and outer surface, HNTs have various applications as ceramic raw materials [3], nanocontainers for active compounds, catalysts, adsorbents [4–8], and polymer fillers [9–12]. It has been largely reported that HNTs is biocompatible, thus its application has been expanded to tissue engineering, drug delivery, and biomaterial compositions [1,13–15].

1.1.2 Halloysite Nanotubes Application — Drug Delivery

HNTs is thermal stable, their hollow tube microstructure is a good candidate for sensitive or toxic drugs carrier. Drugs can be loaded into the lumen with a circulating process of vacuum and sonication. Drugs encapsulated in HNTs could be continually released for 30-100 times longer than applying drugs directly into surrounding solutions [1]. Furthermore, with the modification of aminopropyltriethoxysilane (APTES), HNTs can conjugate with other chemicals, such as folic acid and magnetite nanoparticles and release drug at specific pH environment [13]. The inner surface can be modified by phosphonic acid, which targets alumina, to enlarge the capability of encapsulating neutral and hydrophobic guest molecules. Simultaneously, the out surface can be modified to be solid polar with the treatment of salinizing agents, which results in a stable dispersion of HNTs in water [14].

1.1.3 Halloysite Nanotubes Application — Bulk Filler

HNTs are excellent nanofillers to reinforce variety of materials. Their surface stiffness, thermal stability, strength and modulus can be improved due to the nanoscale, high strength and high aspect ratio of HNTs [1]. In addition, HNTs are eco-friendly and low-cost material and have abundant storage in natural.

1.1.4 Halloysite Nanotubes Application — Tissue Engineering

Due to the enhancement of mechanical properties, HNTs have been employed in tissue engineering to cooperated with traditional materials for a better performance. Porous chitosan-gelatin-agarose hydrogels combined with HNTs have been demonstrated to be biocompatible both *in vitro* and *in vivo.* In addition, it promoted the formation of novel blood vessels and can be absorbed in 6 weeks *in vivo* [15].

1.1.5 Halloysite Nanotubes Application in My Study

In my projects, HNTs were employed as drug carriers and reinforcement additions. Through incorporating with other polymers or working as its own, we assessed the influence of HNTs in the application to address three bone diseases: osteomyelitis, osteosarcoma, and osteoporosis.

1.2 Bone Diseases

The control mechanisms for skeletal systems can be disrupted in many ways and lead to a number of clinically important bone diseases.

1.2.1 Osteomyelitis

Osteomyelitis is a bone infection mostly caused by bacteria or rarely by fungi. It may be caused by open wound contamination, intravenous drug abuse, diabetes, prosthetic implants, surgery, hemodialysis, and removal of the spleen [16]. Humans of any age are susceptible to osteomyelitis. The epiphysis (growth plate) of bones of the legs and arms are the most frequently affected bone sites in children and teens. While, the vertebrae of the spine or the pelvis are often affected in adults [17].

In children, osteomyelitis is generally acute, which develops over several days or weeks. Osteomyelitis in adults can be either acute or chronic. Chronic osteomyelitis usually occurs if the acute osteomyelitis has not been completely remediated, and it can last as long as several months or even years [17]. Patients with osteomyelitis suffer from fever, fatigue, redness and tenderness, swelling, and pain associated with the affected sites. The persistence of microorganisms at diseased bones causes bone destruction and necrosis, which often results to amputation [16].

1.2.2 Osteosarcoma

Osteosarcoma is the most common cancerous tumor in the bone. In general, 80% to 90% of osteosarcoma arises in the long bones such as the femur, tibia, and humerus; while less than 1% are found in hands and feet bones; more rarely, it may occur in the soft tissue [18]. Teenagers and young adults are more frequently affected by osteosarcoma compared to children and adolescents. The etiology of osteosarcoma has not been completely studied, the only verified environmental agent that causes osteosarcoma is ionizing radiation [19]. The presence of retinoblastoma may also increase the risk of osteosarcoma in the patients and their descendants [20]. In addition, a constitutional germline mutation of p53 was found in 3% to 4% of children who suffered with osteosarcoma [21]. Most patients with osteosarcoma suffered with pain. Due to the deep-seated tumor, localized swelling may not be apparent, but continuously bone destruction are happening, which results in bone fracture. Pediatric patients are more vulnerable with a sudden bone fracture than adult patient [18].

1.2.3 Osteoporosis

Osteoporosis is the most common bone disease and is characterized by bone loss, because bone formation fails to keep up with the rate of bone resorption. The deterioration of bone structure and long-term bone mass loss increase the risk of bone fracture. Osteoporosis can develop in a number of ways including aging, race, lifestyle and medical condition. Age-related osteoporosis is the most common form of this disease and is referred as "primary osteoporosis". Osteoporosis that is caused by specific diseases or medications is classified as "secondary osteoporosis" [22]. Bone fractures in the spine, wrist, and hip are usually associated with osteoporosis. Severe bone fracture introduces chronic pains, and patients may be disabled and require long-term hospitalization.

1.3 Disease Treatments and Bone Regeneration

1.3.1 Current Treatments for Osteomyelitis

Osteomyelitis is inflammation of the bone and marrow that is caused by bacteria or fungus infection. *Staphylococcus aureus* (*S. aureus*) is the most commonly involved microorganism in all forms of osteomyelitis [23]. Clinically, a sterilized environment, standard preoperative sterilization, and prophylactic antibiotic treatment have successfully decreased the infection rate of implanted prostheses to 0.5-2.0% [17]. However, insufficient osseointegration frequently happens after orthopedic implant surgeries. The appearance of interval between native tissue and prosthesis gives a chance for microorganism invasion. Once they form biofilm, a revision surgery is necessary to remove the foreign implant. The revision operation would bring more pain and high medical cost to patients and decrease their life quality.

1.3.2 Current Treatments for Osteosarcoma

In the past, patients with osteosarcoma were often treated by amputation, which created significant pain and only had a cure rate of less than 10% [18]. After decades of development, advanced diagnostic methods provide more information to evaluate the extent of tumors and decide the treatment strategy. Localized osteosarcoma, where cancer cells have not spread to other tissue beside the initial site, is currently treated by surgery and combined with pre- and postoperative chemotherapy [18]. However, the rate of local recurrence is as high as 25% and it will be higher if adequate surgical margins are not achieved [24]. When cancer cells spreading to other tissue (metastatic osteosarcoma) such as the lung and forming pulmonary nodules, the affected tissues need to be excised together with the primary tumor to prevent recurrence [18].

1.3.3 Current Treatments for Osteoporosis

Osteoporosis is an accumulation process of bone mass loss with gradual bone deterioration. The imbalance between bone resorption and bone formation leads to a thinner cortical bone and damages to the trabecular bone structure. Osteoporosis is asymptomatic unless bone fractures happened. Osteoporosis can be prevented or delayed by a healthy lifestyle that includes a nutritious diet, adequate calcium and vitamin D intake, and regular physical exercise [22]. Prescription medications can slow bone loss (bisphosphonates, raloifene, alendronate, raloxifene) or promote bone formation (teriparatide), but these drugs have associated side effects [25].

1.3.4 Disadvantages of Current Bone Disease Treatments

Other than removing the infected tissues by surgery and giving a systemic drug treatment when post-surgical infection arising, there is no efficient strategy to eliminate bacterial contamination that originates from implants and give antibiotics at the surgical site. Our first study focused on the development of a hydrogel drug delivery system that could address this problem. The final product of hydrogels could also be utilized for the surface coating of implants and provide a sustained and local drug release, which would dramatically decrease the risk of bacterial infection.

A similar problem exists in the treatments for osteosarcoma. Surgery is the primary approach to excise tumors and continuing with low efficiency and painful chemotherapy. Conventional cancer drug administration goes through blood system or gastrointestinal system. In other words, drugs travel throughout the body before they attack cancer cells at tumor site. Usually higher dosage is required to reach tumor region. Consequently, healthy tissues are exposed to highly toxic pharmaceutical agents that disrupt the regular physiological activities and result in various side effects, such as fatigue, hair loss, anemia, infection, easy bruising and bleeding, numbness, tingling, pain and so on. Our second study of cancer target therapy is a promising solution to address this pain point. HNTs will be modified to selectively bind cancer cells and bring preloaded toxic drugs to the targeted cells. This method protects healthy cells from the harmful effects of the toxic drugs.

Osteoporosis is not as dangerous as osteomyelitis and osteosarcoma until severe fractures occur. Bone grating is one of the most commonly used surgical methods to provide rigid support for fractured bones. It also can be used as joint augmentation or replacement for pain relief and function improvement [26]. Bone grating may be also applied in treatment of osteomyelitis and osteosarcoma as the replacement of the excised bone portion. Due to the aging of populations and trauma caused by accident or exercise, over two million patients are suffered from bone injuries annually worldwide and await a bone graft for defect repair [27]. Currently, in clinically available grafts, autografts are considered the gold standard because of their excellent properties in osteo-conduction, osteo-induction, and osteogenesis [28]. However, concerns of limited supply and the attendant risks of donor site morbidity are still maintained [29]. Allografts are another group of candidates for orthopedic implants. Nearly one third of all bone grafts used in North America are allografts [30]. They are primarily osteoconductive but with less osteo-inductivity, which increases the risk of nonunion and infection [31,32]. Our third study of 3D bioprinting scaffold has great potential to change the source of bone grafts from autografts and allografts to variable biomaterials. Abundant resources of biomaterials enable 3D printed implants to be freely from supply limitation, even better, it provides customized printing based on individual requirement.

1.4 Objectives

My dissertation research has a diverse range of objectives with a unified goal of exploring the application of halloysite nanotubes in bone disease treatment.

- Objective 1: Develop a drug delivery system using chitosan/halloysite hybrid materials to prevent bacterial growth, which can be applied in implant coating.
- Objective 2: Modify halloysite nanotubes to target osteosarcoma and reduce cancer cell growth.
- Objective 3: Dope halloysite with metal nanoparticles and combine them with PLA to build a 3D scaffold for bone regeneration.

1.5 Organization of Dissertation

This dissertation is composed of five chapters. Chapter one is a brief introduction to the clay mineral, halloysite, three bone diseases and the status of current clinical treatments. Chapter two focused on enhancing chitosan mechanical properties with HNTs. The final hybrid hydrogels were used as a drug delivery system to inhibit bacterial growth. Chapter three focused on halloysite surface modification. The modified halloysite nanotubes successfully delivered anticancer drugs to cancer cells without harm of healthy cells. Chapter four focused on the 3D printing of composed PLA/HNTs. The addition of HNTs improved bone regeneration in three-dimensional cell culture. Chapter five discussed the potential applications of HNTs in medical devices for clinical treatment of bone disease and proposed future works.

CHAPTER 2

THE EFFECT OF HALLOYSITE ADDITION ON THE MATERIAL PROPERTIES OF CHITOSAN-HALLOYSITE HYDROGEL COMPOSITES

The sections of this chapter have been published in: Luo and Mills, "The Effect of Halloysite Addition on the Material Properties of Chitosan–Halloysite Hydrogel Composites," Gels, vol. 5, no. 3, p. 40, 2019.

2.1 Introduction

Oral ingestion and intravascular injection of antibiotics have a lengthy application history and are primarily used in the control of post-surgical infection. However, there is a high risk of negative side effects [33,34]. These side effects are principally due to systemic administration through the blood vascular system, which is not directly to the target tissue [35]. In many cases, frequent administration of antibiotics is required to achieve the dosage levels needed to eliminate the infection, and this regimen has the potential to severely impact unaffected tissues resulting in additional medical issues for the patient, such as gastric, hematological, neurological, dermatological, allergic and other disorders [35]. An implantable drug delivery system that can provide a defined drug load directly to the affected tissue is one strategy to resolve this problem. Key design considerations in building such a drug delivery system include biocompatibility, biodegradability, mechanical stability, and the ability to provide sustained drug release. In this study, chitosan and halloysite were used to construct and test composite hydrogels that differed in percent concentration of these materials.

Chitosan is a naturally derived hydrogel, usually produced by alkaline deacetylation and is biodegraded by human enzymes [36]. Chitosan has been proven to be non-toxic, possesses a lack of immunogenicity, possesses the ability to sequester bioactive factors, and has the capability of assembling a tissue-specific extracellular matrix (ECM) [36–38]. It also exhibits some antibacterial properties [39]. This antimicrobial ability makes chitosan a suitable candidate for implant coatings, wound dressing, and drug delivery applications, but chitosan has a major flaw which is its inherent mechanical weakness [40–42]. Many approaches, such as the addition of various polymers [43,44], carbon nanotubes [45,46], or clay nanoparticles [47,48], have been studied as a means to improve chitosan's mechanical properties, and these additives increased the roughness of the scaffold which enhanced cell attachment, proliferation and differentiation [49–51].

Halloysite nanotubes (HNTs) are naturally occurring nanotubes composed of silica and alumina [52], and exhibits a high degree of cytocompatibility hemocompatibility, and biocompatibility [53–55]. They are 1D nanomaterials with a unique hollow tubular morphology that has an external diameter of 50-200nm, luminal diameter of 5-30 nm and a length of 0.5-2 μm [52]. The electrokinetic behavior of HNT at pH 7 is defined by the negative surface potential of SiO_2, with a small contribution from the positively-charged Al_2O_3 inner surface [56–58]. As a polymer filler, HNTs have been shown to significantly improve the material properties of polymers and resins such as alginate [51], calcium phosphate cement [59], epoxy [12], nylon [11], poly(methyl methacrylate) [10], and rubber [60]. The unique hollow tubular structure enables HNTs to be used as drug carriers. The HNT lumen can serve as a reservoir for the loading and releasing of a diverse set of biologically active molecules, including small molecules, enzymes, nucleic acids, and proteins [4,6–8,61]. Moreover, the loading capacity of HNTs can be further enlarged by chemical etching, thus increasing its cargo-carrying capacity [3].

Chitosan (CS) combined with different types of nanoparticles have been extensively studied [62]. Recent studies have shown that these nanocomposites are biocompatible, antimicrobial, and mucoadhesive and can be fabricated into various forms including coatings [63], films [64], hydrogels [51], and membranes [65]. Furthermore, CS, with the addition of HNTs, has also been shown to significantly increase strength, tensile modulus, hardness, and toughness [49,66]. However, these studies only reported on the effects that HNT addition had on polymer mechanical properties, however, the influence of chitosan and HNT concentration and the corresponding impact of different percent combination of these materials on the mechanical properties and cellular behaviors has yet to be established.

In this study, chitosan was chosen to be cell growth scaffold due to its polycationic property and antibiotic potential [39,42]. The drug-carrying capacity of HNTs was employed as additives to improve chitosan hydrogel mechanical properties. The resultant changes in hydrogel surface structure, tensile strength, stiffness, and degradability were studied. Gentamicin was selected as a model drug to assess drug release in CS/HNTs hydrogels of different compositions. Escherichia coli (E. coli) and Staphylococcus aureus (S. aureus) were used as a means for testing the bacterial growth inhibition capacity of the different hydrogels and in estimating drug efficacy. Pre-osteoblasts (MC3T3) were selected to study the potential cytotoxicity of CS/HNTs nanocomposites.

2.2 Materials and Methods

2.2.1 Drug Loading

For drug loading, gentamicin sulfate (GS, Sigma Aldrich, St. Louis, MO, USA) was vacuum loaded into HNTs. HNTs (250 mg/ml.) were mixed with a 2 ml GS solution (250 mg/ml). The mixed suspension was placed in a vacuum and the suspension was vacuumed overnight. The gentamicin contained in the supernatant was measured to determine the drug loading efficiency.

$$\text{Drug loading efficiency} = \frac{\text{gentamicin in supernatant}}{\text{total amount of gentamicin}} \qquad \text{Equation 2-1}$$

2.2.2 HNTs-Chitosan Hydrogel Construct

Low molecular weight chitosan (Sigma Aldrich) was dissolved in 4% critic acid solution (Fisher Scientific, Houston, TX, USA) to form three chitosan concentrations: a 3%, 4% and 5% *w*/*v* solution. Different concentrations of chitosan were combined with HNTs, with the concentration of HNTs ranging from 1% to 5%. Hydrogels were formed by crosslinking the mixture solution with 10% tripolyphosphate (TPP) (Sigma Aldrich).

2.2.3 Scanning Electron Microscopy (SEM) Study

The HNTs-chitosan mixture and pure chitosan solution (200 μL) were dropped into a 10% TPP solution to produce similar sized droplets. After 10 minutes, the beads had formed. They were then frozen at −20 °C for 24 hours and then lyophilized. The structures of hydrogel beads were studied using SEM (AMRAY SEM, Model: 1830, SEMTech Solutions, North Billerica, MA, USA).

2.2.4 Degradation Analysis

0.25 ml hydrogels were cross-linked into micro-beads and incubated in PBS at 37 °C for 24 hours first. Their initial weights were measured W_{d1} after beads air-dried for 30 minutes on filter paper. Then, the hydrogels were divided in two groups, one group was incubated in PBS, another group was incubated in 1 mg/ml lysozyme/PBS solution at 37 °C. Their weights were measured every 2 to 3 days and recorded as W_{dx}. This study was continued for 14 days. The remained weight ratio for each sample was calculated as:

$$\text{Weight ratio} = \text{Wdx}/\text{Wd1} \qquad \text{Equation 2-2}$$

2.2.5 Tensile Properties

The chitosan-HNTs mixture and pure chitosan solution were poured into the same size mold, after they had totally dried, a 10% TPP solution was added for cross-linking chitosan. The crosslinked hydrogels washed with DI water for 3 times, then put on filet paper for air-drying. The prepared films were cut into similar sizes (10 mm × 20 mm), and the average thickness was 0.02 mm. The tensile strength (σ) and elongation (ε) of hydrogels was measured by CellScale Unit with 200 N load cell at a speed of 10mm/min. Young's modulus (E) was calculated based on the equation of $E = \sigma / \varepsilon$. At lease 3 tests for each composite.

2.2.6 Drug Release Study

10 mg of drug loaded HNTs were mixed with 0.5 ml chitosan solution and cross-linked with 10% TPP solution for 30 minutes. The samples were then rinsed with DI water 3 times to get rid of excess TPP solution. Then drug loaded hydrogel samples were incubated in 2 ml PBS at 37 °C to enable drug released from hydrogel to PBS. With designed incubation time, 2 ml PBS was collected and filled with fresh PBS. To measure

drug concentration, gentamicin containing PBS were combined with o-ophthalaldehyde (OPTA) solution and 50% isopropyl at a ratio of 1:1:1 by volume, the absorbance values were measured at 340 nm wavelength. A group of gentamicin solution with known concentration was used to establish standard calibration curve.

2.2.7 Swelling Ratio

Hydrogel beads composed of pure chitosan and chitosan/HNTs composites were prepared as above. Each hydrogel bead was incubated in 200 µL phosphate buffered saline (PBS) at 37 °C for 5 days. At day 1, 3, and 5, the swelling ratio of chitosan and chitosan/HNTs hydrogel composites were determined by the following equations, where, W_s represents the weight of swollen hydrogel after incubation in PBS, and W_d represents the weight of dried hydrogel after swelling.

$$\text{Swelling ratio} = (Ws - Wd)/Wd \qquad \text{Equation 2-3}$$

2.2.8 Bacterial Inhibition Growth Test

Cross-linked hydrogel beads, consisting of CS/HNTs and drug-loaded CS/HNTs, were placed in 1ml *Escherichia coli (E. coli)* and *Staphylococcus aureus (S. aureus)* suspension and incubated with nutrient broth (NB) and Mueller Hinton broth respectively at 37 °C for 24 hours. Pure bacteria suspension without any treatment was set as control, and pure broth was the blank. The absorbance value of samples were measured at wavelength of 630nm at time point of 0, 3, 16, and 24 hours. Each sample has three replicates.

2.2.9 Live/Dead Cytotoxicity Assay

48 well plates were pre-coated with CS or CS/HNTs hydrogel films on which MC3T3 cells (ATCC) were seeded at a density of 1×10^5/ml. Culture wells without any

film coating were used as controls. All cultures were then incubated at 37°C with 5% CO_2 for 24 h. The Live/Dead assay (Life Technologies, Carlsbad, CA, USA) was applied according to manufacturer's directions to assess any potential for cytotoxicity.

2.2.10 Statistical Analysis

Statistical analysis was conducted by using one-way ANOVA or Student's *t*-test. All of the quantitative experiments were performed in triplicate or repeated three times. Data were expressed as "mean ± standard error". Significance between experimental groups and/or controls was determined by one-way analysis of variance. A *p*-value less than 0.05 was considered statistically significant.

2.3 Results

2.3.1 SEM Studies

Chitosan (CS) and chitosan/HNTs (CS/HNTs) hydrogels were dropped into 10% tripolyphosphate (TPP) solution. The ionic cross-linking happened between the NH_3^+ site of chitosan and OH^- site on TPP. After 10 minutes of cross-linking process, spherical hydrogel beads were formed with an average diameter of 3.38 ± 0.28mm. For SEM analysis of surface and structural features of the hydrogel beads, beads were pretreated by lyophilization. The pressure changes in the vacuum chamber during lyophilization caused some hydrogel bead formulations to collapse and lose their spherical shape. A low concentration of chitosan (3% CS, **Figure 2-1** A) was barely able to preserve its original spherical shape as the hydrogel walls collapsed. However, as the chitosan concentration increased, the hydrogel beads structure provided some resistance to deformation and collapse of the hydrogel wall structure (**Figure 2-1** C and E). In contrast, the increased addition of HNTs may have enabled the CS/HNT hydrogels to resist deformation and preserve a more rounded microbead shape. HNTs may have interacted with chitosan to form stronger walls and provide more support to the hydrogel matrix. Also, increased HNTs produced a rougher surface (compare **Figure 2-1** D and F).

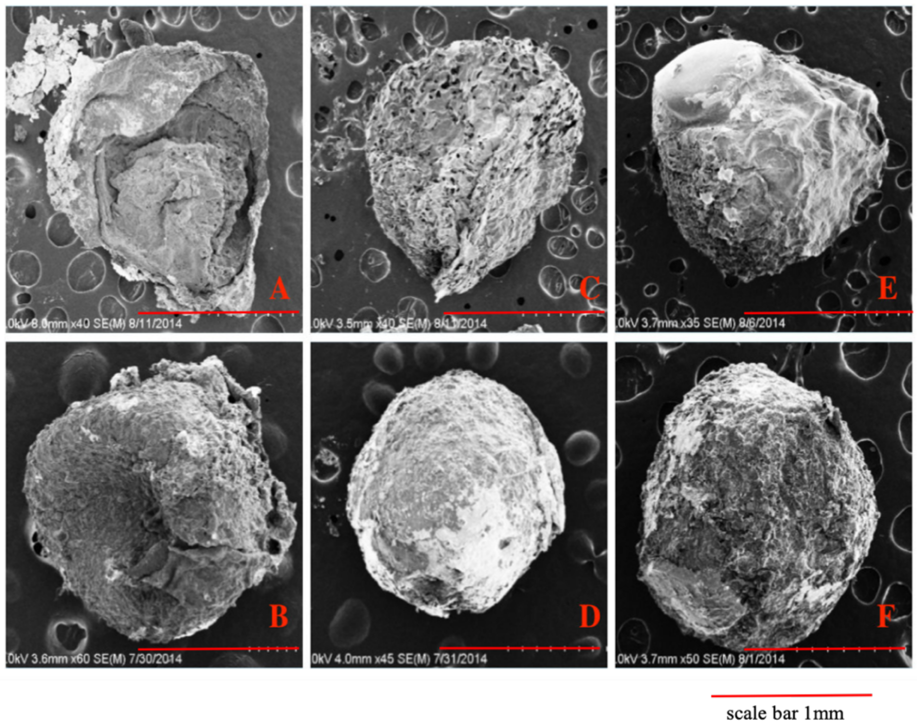

Figure 2-1: SEM images of pure chitosan hydrogel beads with increased chitosan concentration (A, C, E) and chitosan/ Halloysite nanotubes (HNTs) wt./wt. composites (B, D, F). (A) 3% chitosan (CS), (B) 3% CS/2% HNTs, (C) 4% CS, (D) 4% CS/2% HNTs, (E) 5% CS, (F) 5% CS/ 2% HNTs.

2.3.2 Degradation

CS and CS/HNTs hydrogel beads did not exhibit any weight loss when incubated in PBS without lysozyme (data not shown). When the hydrogel beads were incubated with lysozyme, they degraded gradually as expected, and their weight ratio decreased, as shown in Figure 2. Among the pure CS group (**Figure 2-2** A), 3% CS degraded fast after the first 3 days, and this speed was significantly faster than 4% and 5% CS (one-way ANOVA, $p = 2.37\times10^{-6}$). However, after 14 days incubation, the final weight ratios were not significant different (*p* = 0.09). These results show that the biodegradation ability of chitosan does not change with CS concentration. Simultaneously, weight ratios between CS (5%) and CS/HNTs (5% / 1%–5%, *wt.*/*wt.*) were not significantly different (**Figure 2-2** B). The addition of HNTs did not affect CS biodegradability.

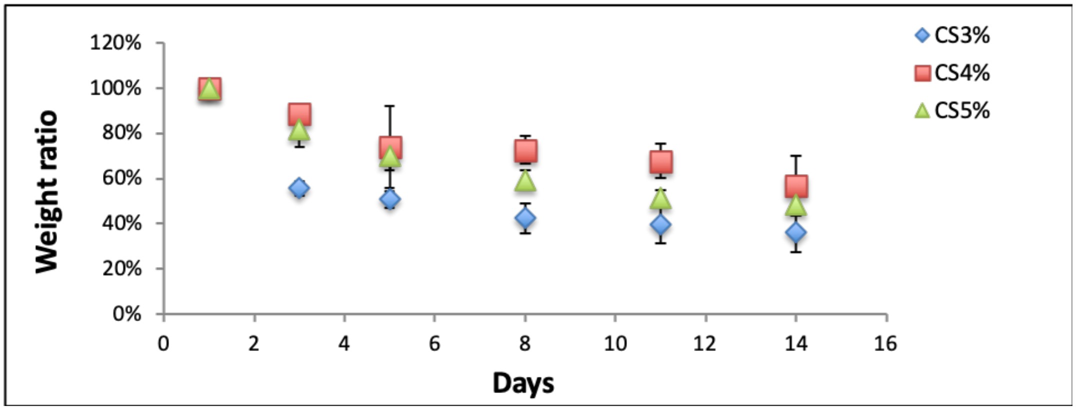

(A)

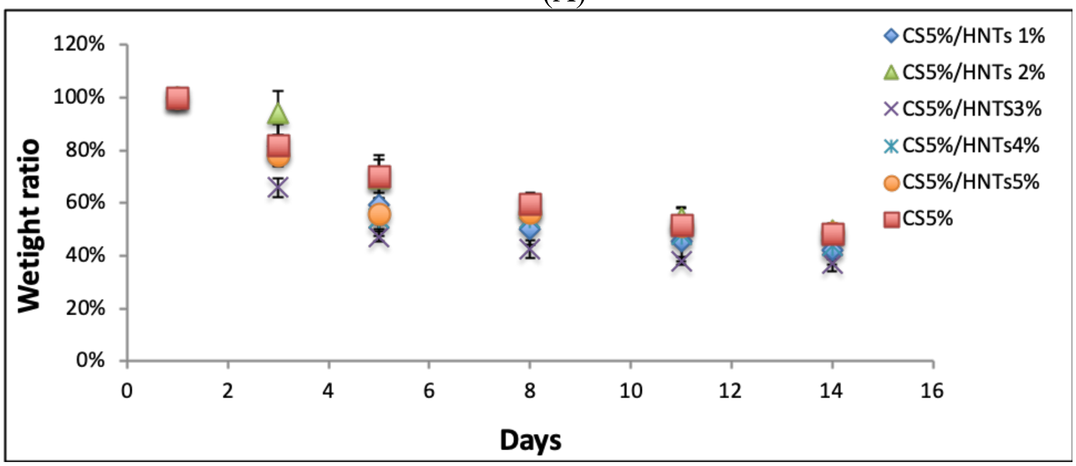

(B)

Figure 2-2: Biodegradability of CS and CS/HNTs in a lysozyme solution (1mg/ml). (A). The weight ratio of hydrogel beads consisted of pure chitosan (3%–5%). (B). The weight ratio of hydrogel beads consisted of 5% CS with different ratios of HNTs (1%–5% wt./wt.).

2.3.3 Tensile Property

CS and CS/HNTs hydrogels (10 mm × 20 mm × 0.02 mm) were subjected to uniaxial testing using a CellScale Univert™ material testing device at a speed of 10mm/min (**Figure 2-3** A, B). As expected, higher chitosan concentrations imparted higher tensile stress resistance (σ), which is represented as MPa, while a lower concentration provided higher elongation (ε) represented as strain (%) in **Figure 2-3** A. The addition of HNTs (2% *w*/*v*) enabled higher force loading but reduced elongation. When 5% chitosan was mixed with HNTs at different ratios (from 1% to 5% *w*/*v*), a lower concentration of HNTs increased the nanocomposites tensile strength and elongation, while this reinforcement decreased with increasing HNT addition. When the HNTs were increased to 5%, the CS/HNTs nanocomposite showed even weaker resistance than pure chitosan (**Figure 2-3** B).

The Young's modulus values were calculated as σ/ε. Based on three repetitive measurements, the average values and standard deviation of Young's modulus were calculated, and the differences were compared and are presented in **Figure 2-4**. A one-way ANOVA analysis demonstrated a significant difference in Young's modulus among the different chitosan concentrations (p = 0.00002) supporting the conclusion that chitosan concentration is a crucial factor affecting Young's modulus. In addition, HNT addition significantly improved the tensile strength of CS, (p = 0.038, 3% CS vs. 3% CS/2% HNTs; p = 0.001, 4% CS vs. 4% CS/2% HNTs; p = 0.00006, 5% CS vs. 5% CS/2% HNTs). However, increases in tensile resistance after HNT addition gradually decreased as the concentration of HNTs increased to 5%, there was a weakening in hydrogel material properties.

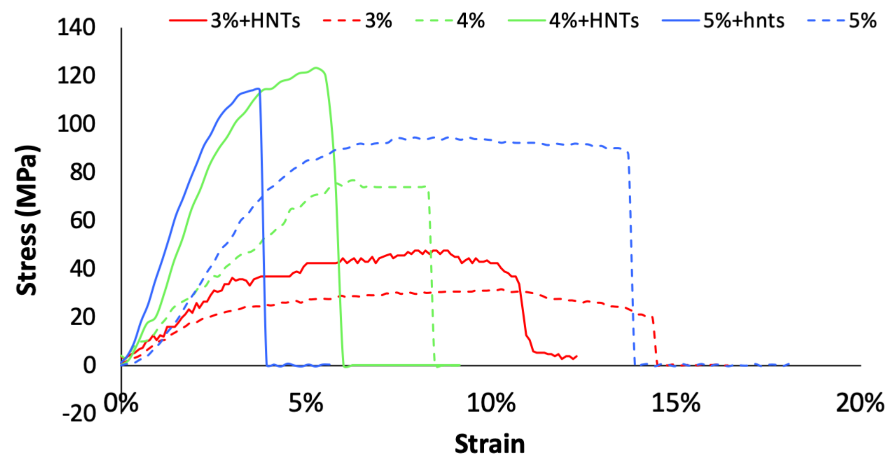

(A)

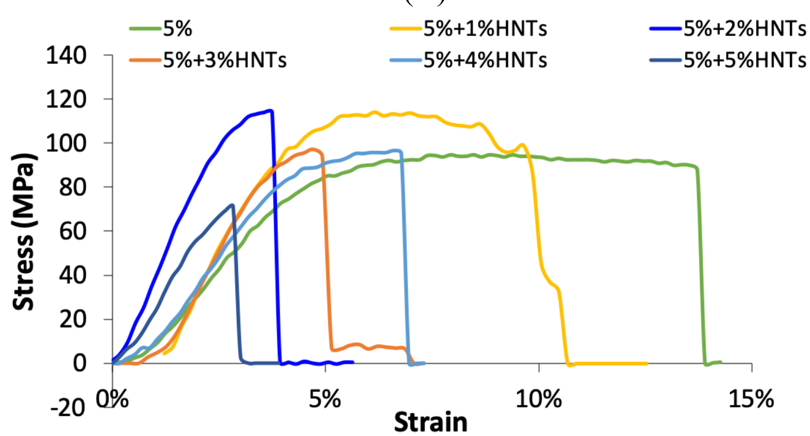

(B)

Figure 2-3: The stress-strain profile of CS and CS/HNTs. (A) Tensile test of pure chitosan (CS) with the HNT additive groups (CS/HNTs). In this graph, every CS/HNT compound has a higher stress value compare to CS group. (3% CS/2% HNTs > 3% CS, 4% CS/2% HNTs > 4% CS, 5% CS/2% HNTs > 5% CS). Simultaneously, a higher concentration of chitosan showed higher stress values (5% > 4% > 3%), however, the strain values displayed a different response (5% < 4% < 3%). (B) 5% CS/1% HNTs showed a major improvement in elongation, while 5% CS/2% HNTs showed the greatest improvement in strength. Increasing the number of HNTs gradually decreased its reinforcement ability, until at these concentrations (CS/HNTs (5% CS/ 5% HNTs), the nanocomposites was weaker and more fragile than pure CS. The stepwise failure behavior (slippage) at the end of each profile represents the fracture point of each specimen.

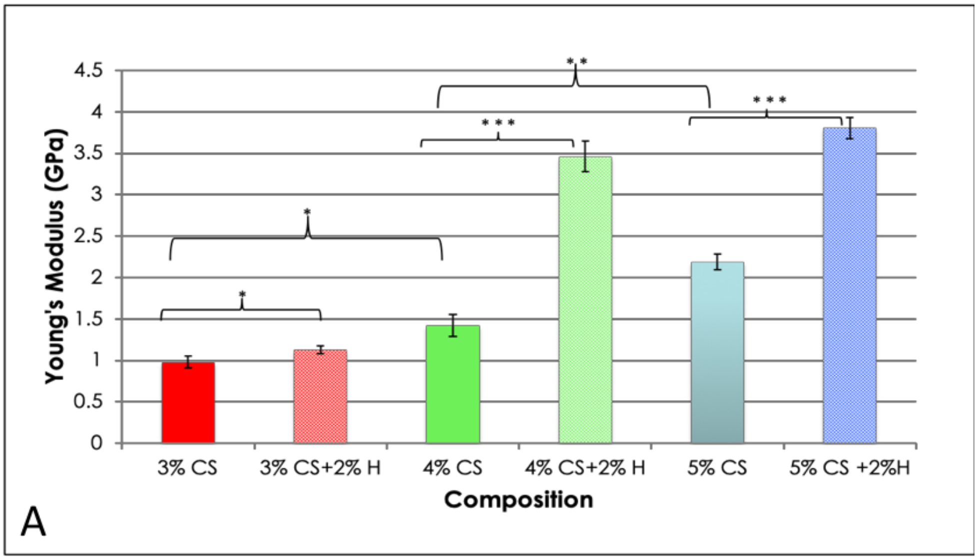

(*, p<0.05; ** p<0.005; *** p<0.0005, n=3)

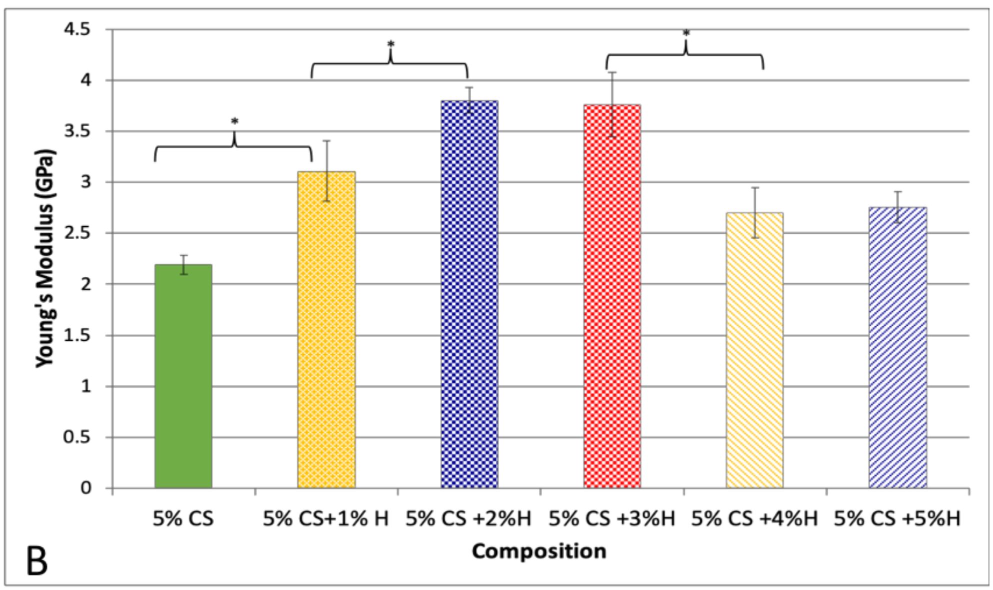

(*, p<0.05; ** p<0.005; *** p<0.0005, n=3)

Figure 2-4: Young's Modulus values of CS and CS/HNTs. (A) Different concentration of chitosan (3%–5%) and their combination with 2% HNTs wt./wt. (B) 5% CS combine with HNTs at different ratio (1%–5%). The changes are similar to the stress-strain profile. Young's modulus value increased with HNTs increasing at low concentration (1%, 2%), as HNTs over 3% in composition Young's modulus value decreased significantly.

2.3.4 Swelling Ratio

Swelling behavior is a consequence of the interaction between a hydrogel and water. The rate of swelling is determined by several of the hydrogel's physicochemical parameters, including its porosity, the nature of its porous structure, and the interactions between its polymer chains and the water molecules. A higher swelling ratio indicates more free volume exists in the hydrogel, and the free volume between knots are affected by the crosslink density. Thus, swelling ratio is also used to measure crosslink density. In this study, swelling ratio was calculated using the fractional increase in the weight of the hydrogel. In **Figure 2-5**, after 1, 3, and 5 days incubation, the swelling ratio of low chitosan concentration (3%CS) is significantly higher than the hydrogel that is composed of high chitosan concentration (3% CS> 4% CS> 5%CS). The addition of HNTs significantly reduced hydrogel swelling ratio (3%CS >3%CS + 2%HNTs, 4%CS > 4%CS + 2%HNTs, 5%CS >5%CS+2%HNTs). Thus, lower concentration of chitosan had less crosslink density, and the addition of HNTs increased the crosslink density. Furthermore, the swelling ratio change indicates that the porosity and porous structure were also affected by chitosan concentration.

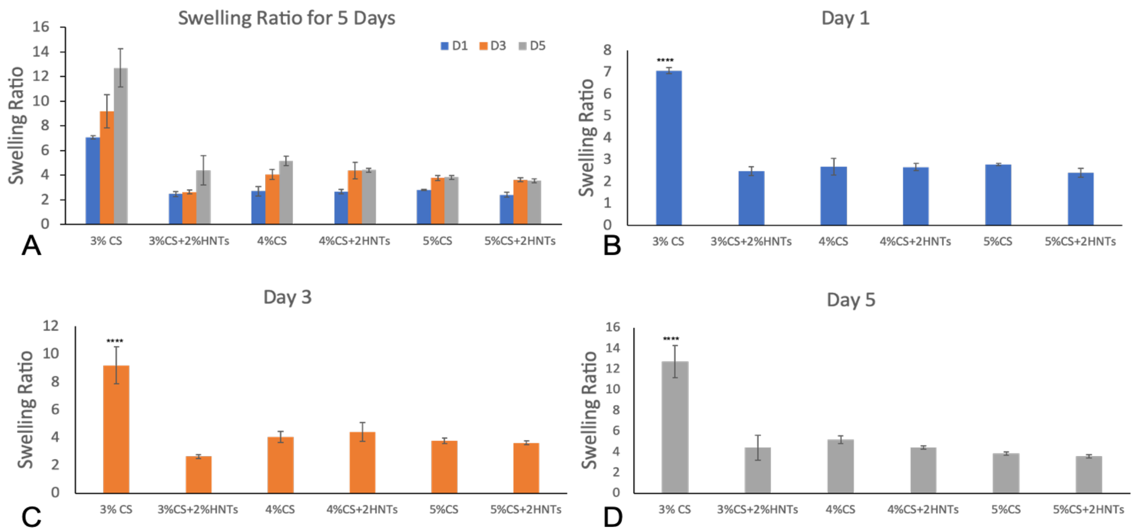

Figure 2-5: Swelling ratio for each hydrogel. The overall changes are presented in summary figure (A). The swelling ratio for Day 1, Day 3 and Day 5 (B–D, respectively). The symbol **** indicates a significant difference ($p < 0.0001$, $n = 3$). Error bar represents standard deviation.

2.3.5 Drug Release

Gentamicin was selected as a model for drug release. The final drug loading efficiency of gentamicin loaded into HNTs was 13.96 ± 1.1%. The pattern of gentamicin release from the chitosan/HNT beads was used to validate what composition would serve optimally as a drug delivery system. As **Figure 2-6** illustrates, gentamicin released from HNTs had a burst release in the first 10 hours, while CS/HNTs provided a more stable and extended drug release profile. According to one-way ANOVA analysis, differences in drug release capability among 3% CS, 4% CS, and 5% CS at first 56 hours were not statistically significant, but at 104 hours, there was a significant difference between them ($p = 0.018 < 0.05$), according to Turkey's multiple comparisons test, 5% CS is significant different from 3% CS and 4% CS, which indicates high concentration of chitosan could provide a longer drug release time.

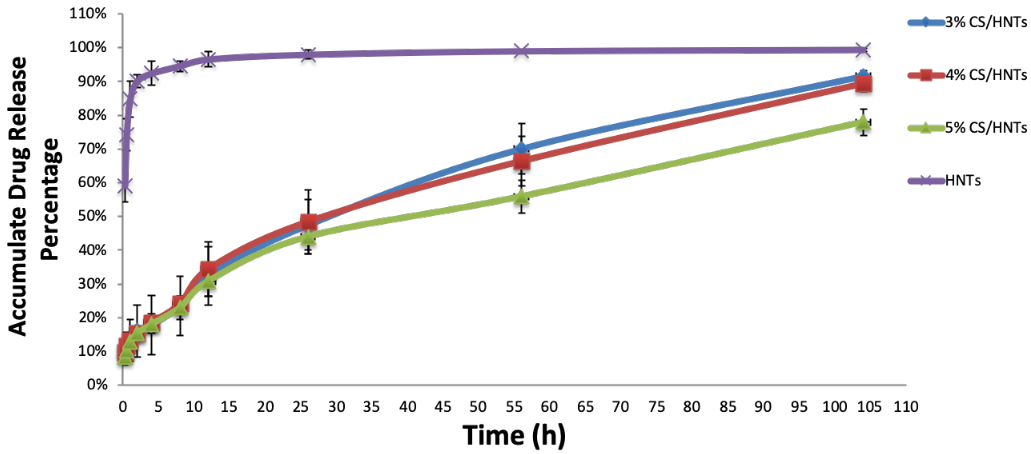

Figure 2-6: Accumulated drug release profiles for CS/HNTs hydrogels and pure drug loaded HNTs. Every group contained the same amount of drug loaded HNTs.

2.3.6 Live/Dead Assay

The Live/Dead assay was applied to pre-osteoblast cultures as a means for estimating the cell viability after exposure to the chitosan and chitosan/HNT composite films. Cell cultures were then photodocumented and the fluorescently-labeled cells also provided an excellent opportunity to observe and record cell adhesion and spreading. As the graphs in **Figure 2-7** show, when compared to control culture wells, cells cultured on CS/HNTs substrates showed excellent cytocompatibility with little cytotoxicity. Observed cellular behavior is not significantly different among control and hydrogel groups with the exception of the 3% CS and 3% CS/ 2%H (H is short for HNTs) groups. Cells cultured on these films appeared to cluster and form small colonies (**Figure 2-8**). This behavior may due to surface features or physicochemical properties of the films. As is shown in **Figure 2-9**, among three different concentrations, 3% chitosan has more wrinkles. This observation is consistent with what we found above: a lower concentration of chitosan had weaker mechanical properties. When cell culture plates were coated with different concentrations of chitosan, lower concentrations of chitosan also presented a reduced degree of stiffness as observed during manual handling of these films. Furthermore, it was more difficult for the softer material to maintain its scaffold structure. During the crosslinking process, multiple micro-scale wrinkles were formed in 3% CS and 3% CS / 2% HNT hydrogels. The substrate surface features and physicochemical properties may have cellular behaviors resulting in the observed cell clusters **Figure 2-7**.

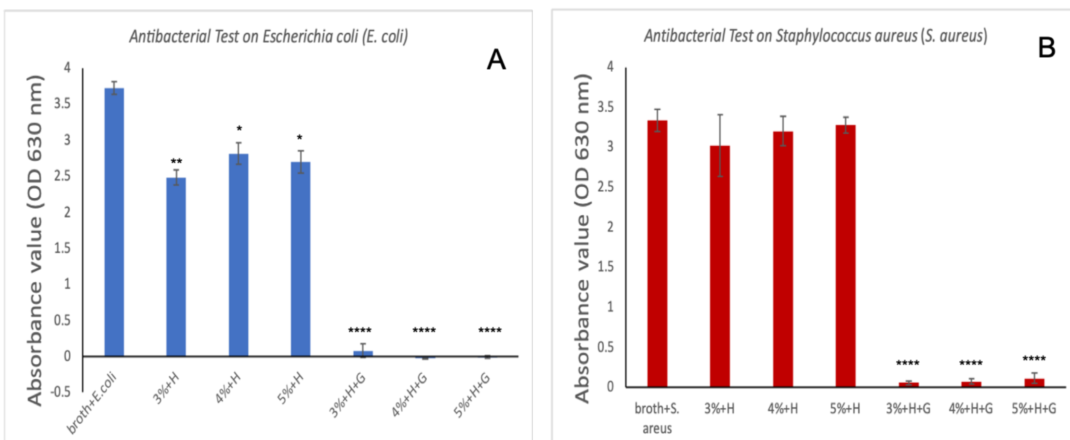

Figure 2-7: Antibacterial test on *E.coli* (A) and *S. aureus* (B). The absorbance values at 630 nm for: pure bacteria suspension (broth + *E. coli,* broth + *S. aureus*); CS/HNTs without antibodies (3%+H, 4%+H, 5%+H), CS/HNTs with antibodies (3%+H+G, 4%+H+G, 5%+H+G). Error bar with standard deviation. (* $p < 0.05$; ** $p < 0.005$; **** $p < 0.00005$, $n = 3$).

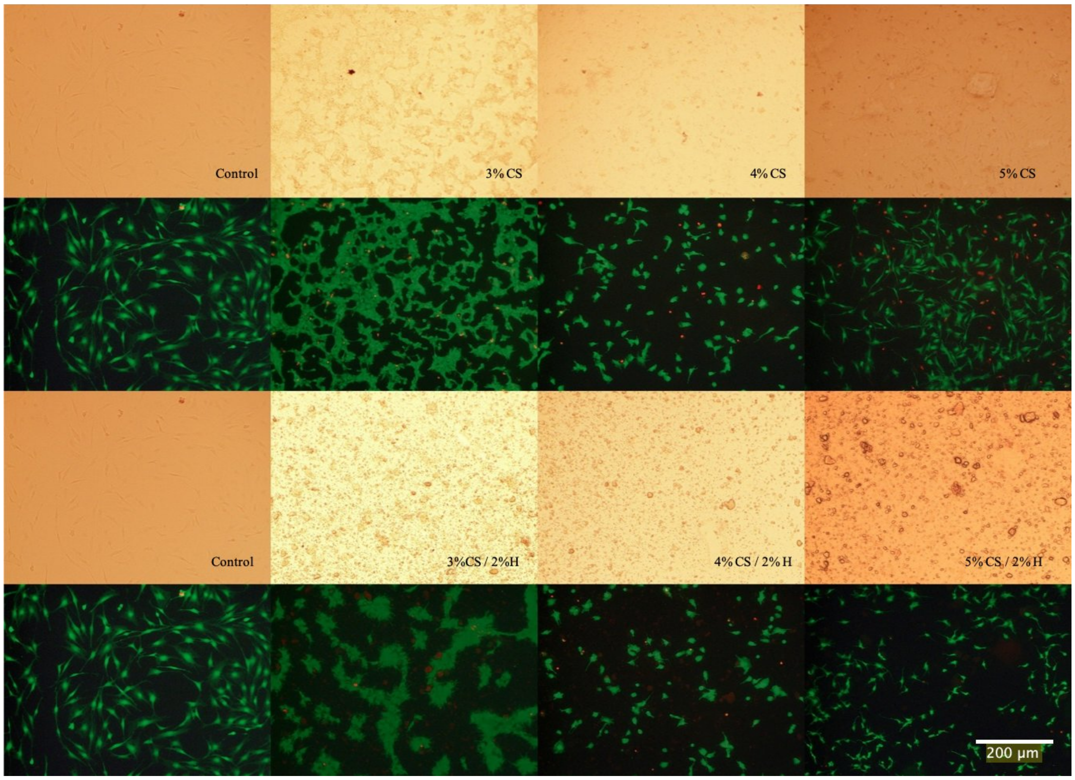

Figure 2-8: Live/Dead Assay of cells cultured on CS and CS/HNTs. Compared to control, there are live cells (green) are observed on the film-coated plates, but the number of dead cells (red) has increased as compared with the control plate but remain few in number. This indicates cells can adhere and proliferate on CS and CS/HNTs substrate. However, cellular morphology was influenced by the surface features and physicochemical properties of substrate.

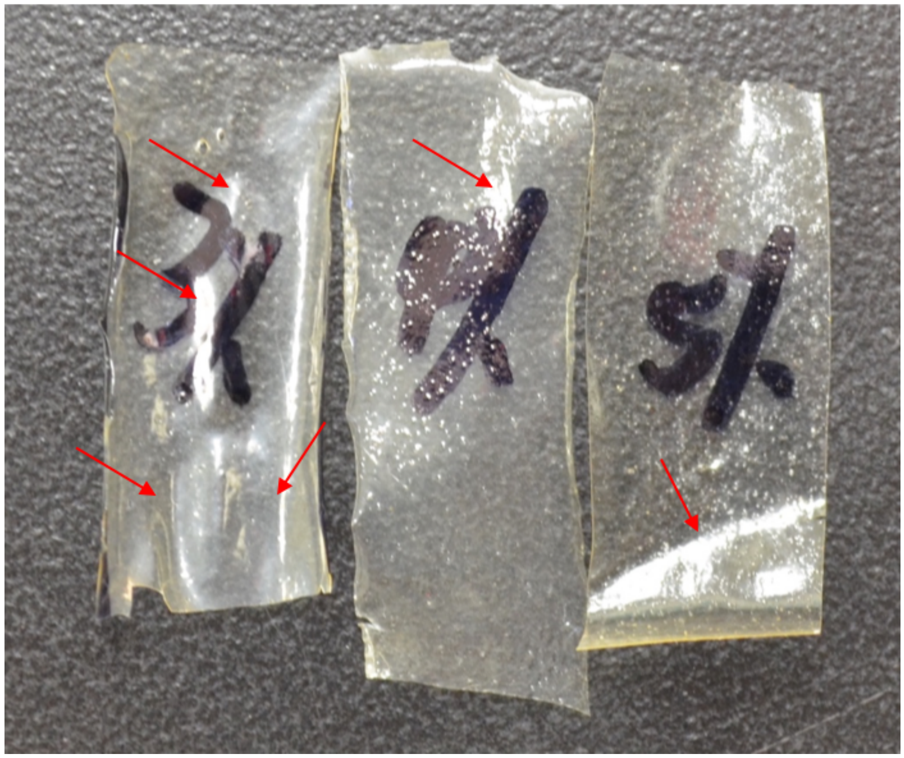

Figure 2-9: Picture for chitosan films after they were crosslinked and dried. The red arrows point to the wrinkles on the film.

2.4 Discussion

The goal of this study was to fabricate a nanoclay-enhanced hydrogel for use as a biodegradable drug delivery system. Critical in our design was to produce hydrogel films with suitable strength enabling a range of application such as topical application or injection. Clay nanoparticles are present in nature in several different morphologies depending on the nature of their layered structure. Clay nanoparticles are being actively studied for their potential in a variety of biomedical applications, in particular, drug delivery. The most well-known of these nanoparticles include kaolinite, montmorillonite, and halloysite [67,68]. Kaolinite is an abundant and inexpensive clay mineral and has a long history in drug delivery applications [69]. Kaolinite has been used in many pharmaceutical applications either as an excipient or an active ingredient because of its excellent physical, chemical, and surface physicochemical properties [68,69]. Its application within composite drug delivery systems include antimicrobial [70], anticancer [71], skeletomuscular and geriatric diseases [69] as well as a bioactive agent for the treatment of some common diseases. Kaolinite and chitosan nanocomposites have seen significant research activity [72,73].

Montmorillonite clay (MMT) belongs to the smectite group with tetrahedral silica sheets layered between alumina octahedral sheets at a ratio of 2:1, respectively [74]. It has a large specific surface area, exhibits good absorbance ability, high cation exchange capacity, adhesiveness, and drug-carrying capability [73,74]. Drug incorporation into MMT can occur by adsorption both within its interlayer-spaced structure, by replacement of the water molecules, and on the surface. The most important interactions taking place between the two components of the hybrid system are ionic [74,75]. Chitosan MTT composites have developed as drug delivery systems for antimicrobial [76], cancer [77], gastrointestinal [77], osteoarthritis [78], and wound healing applications [79]. Emerging in 2012 as a potent nanocarrier and nanocontainer, halloysite is tubular aluminosilicate nanoparticle that has been under intense study as an agent for the sustained release of antibiotics, chemicals, chemotherapeutic agents, and growth factors [74,75]. HNTs typically display an inner diameter ranging from 15 to 50 nm, an outer diameter ranging from 30 to 50 nm, and lengths between 100 and 2000 nm [80–82]. HNTs have been shown to serve as a nanocontainer with vacuum-trapped drugs, bioactive agents, and other substances, and these are released in a sustained manner [83–86].

In this study, the effects of chitosan and HNTs concentration and combination ratios of these materials on the mechanical properties of a hydrogel composite and its drug release capability were analyzed. Our results suggest that a higher chitosan concentration produced a more uniform bead shape and a greater drug release capability. Other studies have shown that ionic gelation [63,64] (Al^{3+}, Ca^{2+}, and Zn^{2+}) or chemical cross-linking [87,88] can also produce strong beads with a more spherical shape. Lower concentrations of chitosan and HNTs produce beads that were very soft and irregular in shape.

Higher chitosan concentration also created a hydrogel with smaller pore sizes. Hydrogels with smaller pores were also less deformable than gels with larger sized pores. A similar finding was reported by Chiu et al., (2013) with poly (ethylene glycol)-co-(l-lactic acid) hydrogels [89]. To verify this potential explanation, we took the cross-section SEM images for the hydrogel beads. In **Figure 2-10**, both 4% and 5% chitosan and their HNTs composite hydrogels have numerous small pores. There is no significant different in pore size between 4% and 5% chitosan and its HNTs composites. However, 3% chitosan and its HNTs composite hydrogels have numerous bubbles instead of pores, and the bubbles are much larger than the pores formed in 4% and 5% chitosan hydrogels. Those bubbles were formed during the drying process. If all the bubbles break, larger pores remain. This observation partly supports our hypothesis.

As expected, the deformability decreased with diminishing of polymer content, since polymer content has an influence on cross-link density. This finding agrees with other two literatures [90,91]. The mechanical properties also diminished rapidly during incubation, suggesting a bulk mechanism of degradation, which is consistent with our swelling (**Figure 2-5**) and pore size observations (**Figure 2-10**). The addition of HNTs to chitosan did not affect pore structure or porosity of the scaffolds, a result also reported by

Liu et al.. [49]

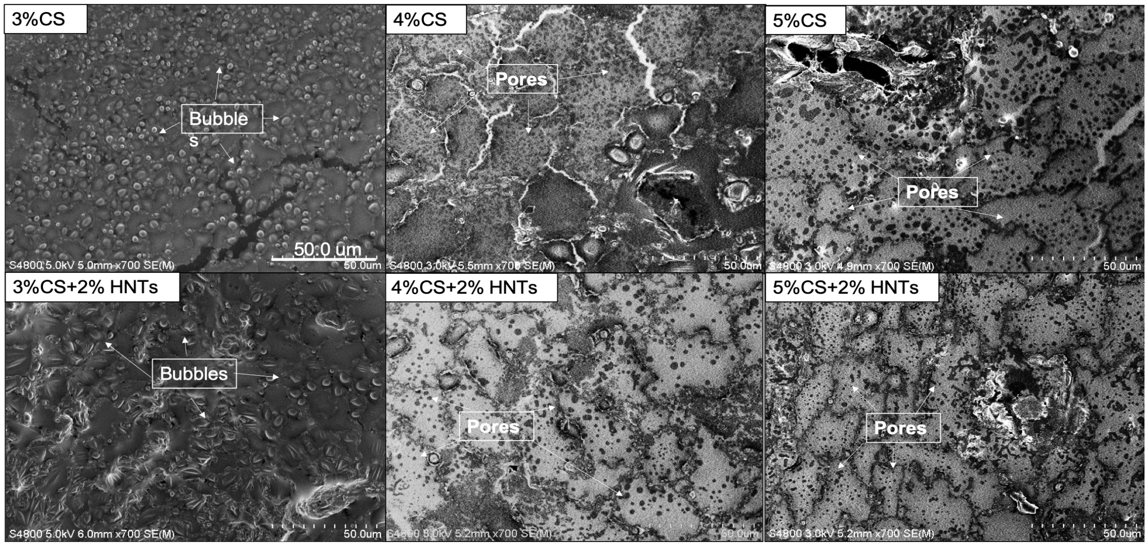

Figure 2-10: SEM images of cross-section for different hydrogel composites. The arrows in the picture of 3% chitosan (3%C) and its HNTs composites (3%CS + 2%HNTs) point to the example of bubbles. The arrows in the picture of 4% chitosan (4%C) and 5% chitosan (5%C) and their hydrogel composites (4%CS + 2%HNTs and 5%CS + 2%HNTs point to the example of pores.

The objective of the degradation study was to determine whether the HNTs addition inhibited or increased chitosan degradation. Our research showed no significant effect with HNT addition on degradation, indicating that the stability of the chitosan/HNT and the predictability of biodegradation rates depend on the final composites. As anticipated, HNT addition contribute to improve chitosan hydrogel tensile properties. In two previous studies, HNT addition to the chitosan matrix also significantly enhanced compressive strength, compressive modulus, and thermal stability [66,88]. HNTs are widely used as a polymer bulk filler added to significantly improve the mechanical, swelling, water uptake, thermal, drug-loading efficiency of the composite matrices [7,49,56].

In this study, however, when HNT concentration exceeded a threshold value, hydrogel deformability decreased sharply. A 2% wt./wt. combined ratio showed the best response to tensile testing. The results of degradation can also be explained along the same lines. The 2% wt./wt. HNTs-chitosan hydrogels also showed the slowest rate of degradation. Our observation of HNT response to deformability may be caused by inadequate dispersion of HNTs in the chitosan matrix [37]. The interfacial binding between HNTs and chitosan is achieved by hydrogen bonding and electrostatic interactions [49]. A uniform dispersion results in a uniform interfacial-binding matrix, which is favorable to force conduction. In contrast, too many nanotubes inhibit the dispersion state and create interfacial gaps, which are easy to break. This phenomenon is clearly presented in Figure 11: 5% chitosan combined with HNTs at different rations (1% to 5%), HNTs clusters were observed by SEM. The hydrogel films with higher concentration HNTs have larger and more HNTs clusters. Those clusters resist the force conduction and may result in gaps, which is shown in the insert picture of **Figure 2-11** 4% HNTs. Instead of reinforcing the biomaterials, exceeded addiction of HNTs weakened the biomaterials original mechanical properties.

In terms of the chitosan/HNT composite's potential as a drug delivery system, the results of the drug release profile analysis showed a doped drug could be released in a sustained fashion, and bacteria growth inhibition tests indicate that the release of gentamicin was able to inhibit bacterial growth. In summary, the chitosan-HNTs hybrid hydrogel exhibited better mechanical properties than pure chitosan hydrogels, and their combination showed a more sustained ability in drug release. Chitosan and HNTs are eco-friendly and biocompatible materials [44,45,51,54,55], and with increases in their mechanical properties, they will have increased use in clinic treatments. For instance, coating implants and providing a long-term drug delivery to prevent wound infection.

Furthermore, instead of antibiotics HNTs could be loaded with growth factors designed to direct cell migration by chemotaxis or induce differentiation.

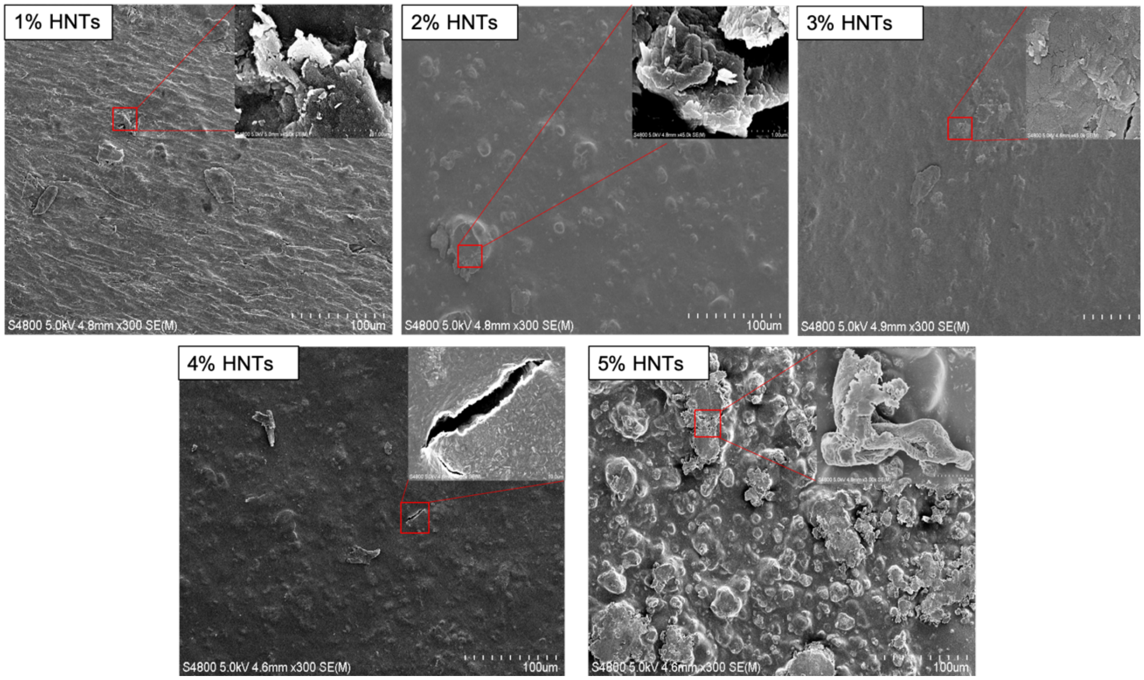

Figure 2-11: SEM images of hydrogel surface that consisted by 5% chitosan and combined with HNTs at different rations (1% to 5%). The pictures in the right corner are the zoom in pictures of the selected areas.

2.5 Conclusions

Chitosan-based hydrogels are being used for their biodegradable properties and their ability to that mimic the extracellular matrix of many tissues. However, the use of chitosan hydrogels has been limited by their inherent mechanical weakness. This study examined the effects of increased chitosan and HNT concertation on selected mechanical properties of chitosan/HNT hydrogels, with and without gentamicin addition. HNTs are widely employed as a bulk filler to improve the performance characteristics of many polymers. HNTs have also been shown to be a viable nanocontainer able to provide sustained release of antibiotics, chemicals, and growth factors. The addition of HNTs to chitosan hydrogels improved the gels' mechanical properties. Chitosan/HNT gentamicin-doped hydrogels enabled sustained drug release and were effective in reducing bacterial growth. Our doped clay/chitosan nanocomposite may overcome the limitations of traditional anti-bacterial hydrogels by providing a focal drug delivery and sustained release of drugs, singly or in concert, or a suite of drugs or drug/growth factor combinations.

CHAPTER 3

BI-FUNCTIONALIZED HNTS: CELLULAR UPTAKE ANALYSIS AND CHEMOTHEREUTIC POTENTIAL

3.1 Introduction

Cancer is the second leading cause of death in the United States [92]. While radiation and surgery treatments have advanced cancer treatment, chemotherapy is still one of the leading treatment modalities [93]. Unfortunately, current chemotherapeutic agents adversely affect healthy cells at the target site as well as elsewhere in the body [94]. Chemotherapy drugs work by impairing cell division and are effective treatments for early-stage tumors when cancer cells are rapidly multiplying. However, they also produce a range of unpleasant side effects. Systemic toxicity is an undesired consequence for the majority of chemotherapeutic drugs [92 93]. The development of a multi-functional drug delivery system (DDS) that can provide extended, controlled, and selective drug release is at the forefront of current cancer therapy research [9394]. Targeting chemotherapeutic drugs directly at the tumor cells would increase drug effectiveness and reduce side effects.

Recent advances in nanoparticle (NP) research have shown promise in remediating many of these adverse effects [95–97]. A key challenge for scientists is to design cancer nanoparticles that target cancer cells only and are retained at tumor sites. Cytotoxic chemotherapies have a narrow therapeutic window, with high peaks and troughs of plasma concentration. Novel nanoparticle formulations of cytotoxic chemotherapy drugs can enhance pharmacokinetic characteristics and facilitate passive targeting of drugs to tumors via the enhanced permeability and retention effect, thus mitigating toxicity [96,97]. By design, these nanoparticle types can directly carry cancer drugs to cancer tumors, thereby improving the ability to kill cancer cells and hence leading to more effective treatment outcomes. Nanoparticle currently in clinical use or undergoing clinical investigation for anticancer therapies include liposomes, polymeric micelles, protein-drug nanoparticles, and dendrimers [98,99]. Surface modification of NPs with suitable ligands or targeting agents has the potential to improve therapeutic efficacy and reduce the unwanted side effects of systemic delivery [100,101]. Recent studies on the interaction between surface-functionalized nanoparticles and animal cells have shown great potential for using these nanomaterials for various biomedical and biotechnological applications, such as cell type recognition, disease diagnosis, intracellular imaging, and drug/gene delivery.

Multifunctional nanoparticles, with both diagnostic and therapeutic functions, show great promise towards personalized nanomedicine. Folate receptors (FRs) are overexpressed in numerous cancers but are under expressed or nonexistent in most normal tissues. Thus, folic acid is considered as one of the best-characterized ligands to use in targeted drug delivery. Halloysite nanotubes (HNTs) have been widely studied as a drug carrier as they provide sustained drug release for a variety of bioactive factors. Halloysite nanotubes are naturally occurring nanotubes composed of silica and alumina [102]. They typical inner diameter, outer diameter, and length of these tubes are 1-30 µm, 30-50 nm, and 100-200 nm, respectively [82]. Halloysite nanotubes have a large external surface area and an internal pore volume capable of encapsulating and delivering large quantities of biogenic molecules. HNTs were chosen as they are an effective nanocontainer and nanocontainer that can entrap a range of bioactive agents and drugs within the inner lumen or in an outer coating for film, followed by their sustained release [51,103,104].

An essential aspect of HNTs that allows these nanotubes to be considered in the design of a multi-functional DDS is their lack of cytotoxic effects [105]. Halloysite nanotubes were added to different cell cultures for toxicity tests. The data showed that HNTs had low cytotoxicity, rendering it a suitable candidate for household materials and medicine [81]. In another study, HNTs were added to cultures of epithelial adenocarcinoma and human breast cancer cells up to a concentration as high as 75µg/mg, and cell proliferation was not affected [54]. HNTs have also shown biocompatibility in other organisms such as *Caenorhabditis elegans* (*C. elegans*) and did not appear to cause any damage to cell organelles [106,107]. All these studies support the observation that HNTs can be placed within an organism without any observable adverse side effect [108,109].

Surface modification of HTNs for drug delivery purposes has also seen significant research interest [109,110]. One widely used for HNT surface modification is the addition of silanes to the surface [111,112]. In contrast, the area of chemical modification of HNTs via covalent bonding, is an area that has seen only a few studies using bioactive molecules [110]. Covalently functionalized halloysite nanotubes have molecules grafted onto the HNTs surface [111,112]. In a previous study, a method was developed to attach folic acid (FA) to the HNT surface with the addition of a second molecule, of fluorescein isothiocyanate (FITC) to create a bi-functionalized HNT (b-HNT) [113]. The bHNT were characterized by

FTIR, ^{13}C CPMAS NMR spectrum, and UV-Vis, and the data demonstrated that folic acid (FA) and fluorescein isothiocyanate (FITC) covalently bonded to the HNT surface [113].

Conjugation of NPs with antibodies and ligands such as folic acid (FA) allows for the specific targeting of NPs to the cancer cells, which overexpresses the receptor for the targeting ligand [114,115]. Numerous studies have shown that FA is an attractive targeting agent which is specific to the FA receptors (FRs) [116,117]. FA receptors are overexpressed in several cancers such as in breast, brain, colon, lung, kidney, and cancers [117,118]. The expression level of FA receptors is around 150–300 times more than that of the healthy tissues [118,119]. Folic acid (FA), an oxidized form of folate, can bind to FRs and increase cellular uptake in cancer cells, while the FA receptor is poorly expressed in healthy tissues. Owing to this distinguishing property, FA has emerged as a suitable targeting agent for cancer treatment [116].

With tailored surface modification, HNTs can be developed into a targeted drug delivery system [120–122]. In our design of a bi-functionalized HNT (b-HNT) drug delivery system, FA would allow for selective targeting of tumors while the effectiveness of the targeted system can be determined via a second ligand, FITC, for imaging [113]. We tested our b-HNT for cell viability, proliferation, cell uptake efficiency and, the ability to deliver an anti-tumor agent, methotrexate (MTX). MTX is a folic acid antagonist and it has a therapeutic effect on many cancer types. It is widely used as a major chemotherapeutic agent for lymphoblastic leukemia, lymphoma, osteosarcoma, and breast, lung, head, and neck cancers [123–125].

In this study, colon cancer cells (CT26WT) were used to assess the proper dosage of bHNT. Cell viability decreased below 80% at high dosage (150 mg/ml), the cause of cell death was further analyzed. We also found that the size of nanoparticle has a significant effect on cells uptake efficiency. Extracellular particles get into cells mainly through clathrin- and caveolae- dependent endocytosis. Two inhibitors chlorpromazine (CPZ) and filipin were used to disrupt clathrin- and caveolae- dependent endocytosis, respectively. The fluorescent signals express by cells were measured to confirm the cell uptake mechanism for bHNTs. Observations made by multi-photon microscopy indicated that bHNTs were present and distributed throughout the cellular cytoplasm inside the cells. Methotrexate was loaded into the bHNTs lumen and delivered into cells. One untransformed cell line, preosteoblast (MC3T3-E1), and two cancer cell lines, colon cancer cells (CT26WT) and osteosarcoma (K7M2 WT), were selected to assess bHNTs target ability and drug efficiency.

3.2 Materials and Methods

3.2.1 Materials

All cell culture materials and reagents were purchased from Sigma Aldrich, St. Louis, MO. Cell culture dishes, pipettes and other disposable plastics were purchased from Mid Sci, St. Louis, MO. CT-26 murine colorectal cancer cells.

3.2.2 Production of Shortened HNTs

10 g of commercially purchased HNTs were immersed in 50 ml PBS for 24 hours and ultra-sonicated for 30 mins by Qsonica Sonicators at 70% power. After they were relaxed for 30 mins, HNTs were ultra-sonicated for another 30 minutes. Then the mixture

was transferred to 50 ml centrifuge tube and centrifuged at 100 g for 10 minutes. The deposition was collected and dried at 60 °C for 2 days.

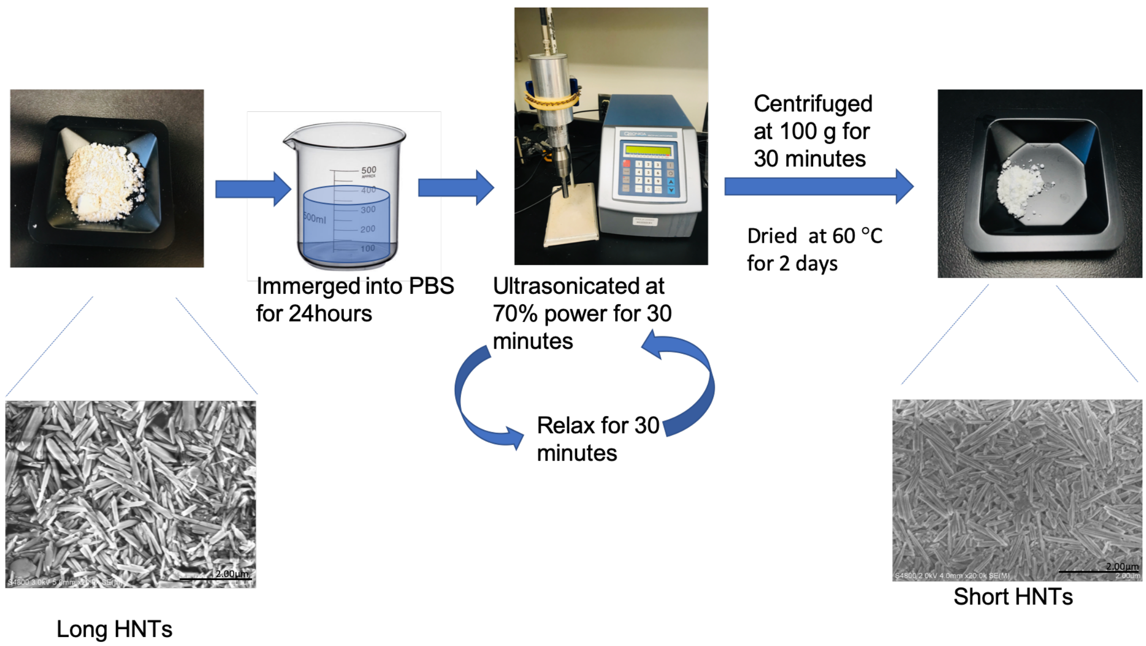

Figure 3-1: The process of short HNTs fabrication.

3.2.3 FA/FITC-HNTs Synthesis

The FA/FITC-HNTs were synthesized by the same methods as our previous study. Briefly, HNTs were reacted at reflux with N-[3-(trimethoxysilyl)propyl] ethylenediamine (DAS) in toluene for 24 hours. Then, the HNT-DAS composite was reacted with FA in the presence of 1-ethyl-3-(3-dimethylaminopropyl)carbodiimide (EDC) in DI water overnight. Finally, the complex reacted with FITC in acetone overnight. Between each step, the complex was washed and filtered by using methanol, sodium chloride solution, sodium bicarbonate solution, and distilled water (DI) water.

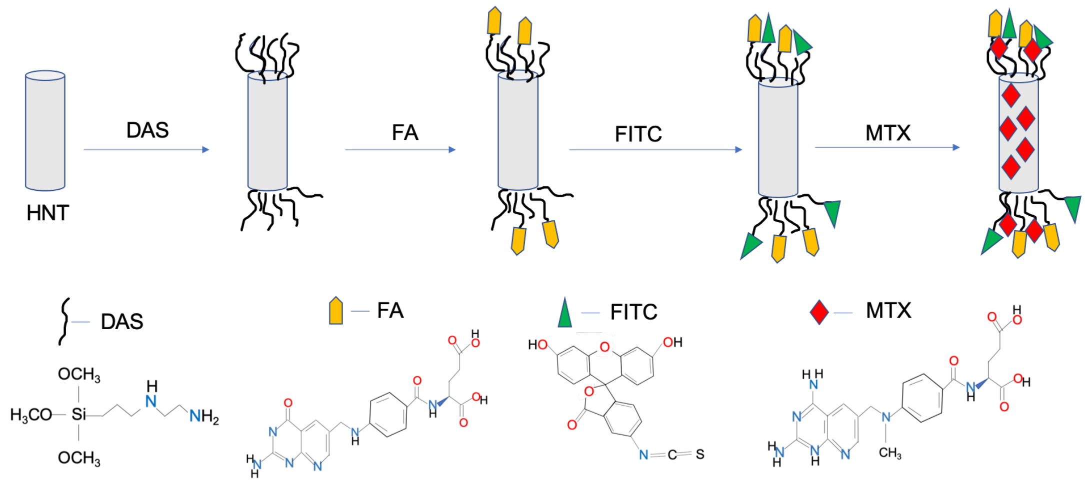

Figure 3-2: Schematic representation of the conjugation of both FA and FITC to DAS which is attached to the surface of the HNTs. Methotrexate (MTX) was doped into the HNT lumen. DAS =N-[3-(trimethoxysilyl)propyl) ethylenediamine, FA = folic acidity = fluorescein isothiocyanate.

3.2.4 FA/FITC-HNTs Characterization

The infrared spectrum (FTIR) was recorded at a resolution of $4s^{-1}$ with 16 scans using a Thermo Scientific NICOLET™ IR100 FT-IR Spectrometer (Thermo Fisher Scientific; Waltham, MA). Thermo Scientific OMNIC™ software was used to study the stretching bands.

SEM images of original size of HNTs and shortened HNTs were analyzed by ImageJ and also used to measure particle size.

3.2.5 Cell Culture

Cytotoxicity of functionalized (coated) HNTs were studied in CT26-WT murine colorectal cancer, K7M2-WT osteosarcoma cells, and MC3T3-E1 preosteoblast cells. All cells came cryopreserved from ATCC. Cryovials were thawed and allowed to equilibrate in a water bath, all the cells were cultured in 25 cm^2 tissue culture flask and incubated at 37°C under humidified 5% CO_2 and 95% air. CT-26 cells were cultured in RPMI 1640 medium containing 10% FBS and 1% penicillin (complete medium). Osteosarcoma cells were fed by complete DMEM containing 10% FBS and 1% penicillin. Preosteoblast cells were incubated in complete alpha-MEM containing 10% FBS and 1% penicillin. Subconfluent cells were passaged with 0.25% trypsin, collected by centrifugation, suspended in cell culture medium and cultured at a 1:4 split into 25 cm^2 tissue culture flasks. All three types of cells underwent passage four before use.

3.2.6 MTS Assay

Cell proliferation ability affected by HNTs and FA/FITC HNTs were assessed by MTS assay. Cells were seeded into 48-well plate at a concentration of 1 X 10^5 cells/ well and cultured for 24 hours. Different amounts of pure HNTs or functionalized HNTs were added into cell culture plates (0, 50, 100, 150, 200, 250 μg/ml). 40 μl MTS stock solution were added to each well and cultured for 2 hours at 37 °C in darkness. 200 μl of supernatant of each sample were transferred to 96-well plates and absorbance values were read at 490 nm by microplate reader.

3.2.7 XTT Assay

The cytotoxicity of HNTs and FA/FITC HNTs were studied by XTT Cell Viability Assay Kit (BIOTIUM). Cells were cultured and treated following the same procedure as MTS assay. 100 μl of cell suspension were added into 96-well tissue culture plates, then added 25 μl activated XTT solution were added and the combination were incubated for 2 hours. Absorbance values were measured at 450nm; background absorbance was measured at 630nm. The final normalized absorbance values were obtained by subtracting background absorbance from signal absorbance.

3.2.8 Cell Uptake Efficiency

CT26WT, murine colorectal cancer cells, were selected to assess cell uptake efficiency. Cells were seeded into 48 wells at concentration of 1.5×10^5 cells/well and incubated for 24 hours. Then, biofunctionalized FA/FITC-HNTs were added into cell culture medium at a finial concentration of 25 μg/ml and incubated for another 24 hours. Cell fluorescent intensities were measured by fluorescent microplate reader at 490/525 nm (Ex/Em) at designed time points. Before measuring, cells were washed with fresh RPMI 1640 3 times to wash away FA/FITC-HNTs that did not uptake by cells. The cell numbers were measured.

3.2.9 Cell Uptake Mechanism

CT26WT cells were seeded into 24 wells at concentration of 2×10^5 cells/well and cultured for 24 hours. Two inhibitors chlorpromazine and filipin were selected to assess cell uptake mechanism. Cells were pre-cultured with chlorpromazine (CPZ) (7 μg/ml) or filipin (5 μg/ml) for 2 hours. Cells treated without any inhibitor served as the control. FA/FITC-HNTs (25 μg/ml) were added to each well and incubated for another 24 hours. Fluorescent intensities expressed by cells were measured as above.

3.2.10 Multi-photon Image

CT26WT cells were seeded on a glassed slide at a concentration of 1×10^5 cells/ml and cultured for 24 hours. FA/FITC-HNTs were added into cell culture plate (25 μl/ml) and continually incubated for 12 hours. DiOC18(7) (DiR) (ThermoFisher Scientific) working solution were prepared by following the company protocol. Cells were washed by DPBS for 3 times, then DiR working solution was added into each cell culture well (1 μg/ml) and incubated for 2 hours. Then cells were fixed by 4% paraformaldehyde for multi-photon images.

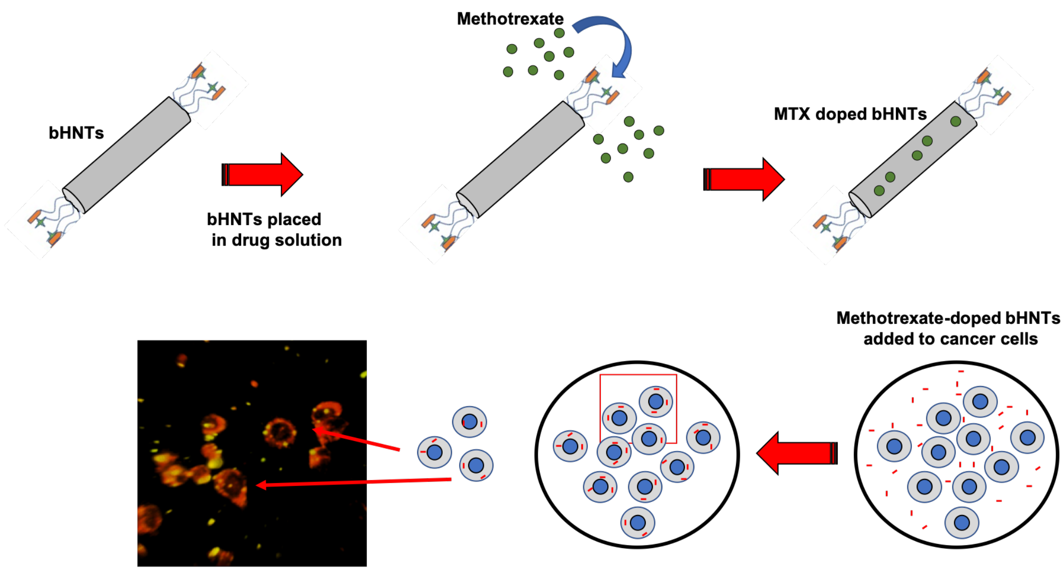

Figure 3-3: Schematic representation of multi-photon images.

3.2.11 Apoptosis and Necrosis

In our previous study, FA/FITC-HNTs at high concentration, 150 ug/ml, significantly reduced cell viability below 80%. The mechanism of cell death was further analyzed by Annexin V-FITC Apoptosis Kit (BioVision). In brief, Ct26wt cells were seeded into 24 wells at a concentration of 2×10^5 cells/well and cultured for 24 hours. Then, a large amount of FA/FITC-HNTs was added into cell culture medium (150 μg/ml) and incubated for 24 hours. Then 3×10^5 cells were collected and suspended in 500 μl of 1X Binding Buffer, then mixed with 5 μl of Annexin V-FITC and 5 μl of propidium iodide. Cell suspension mixtures were incubated in a dark environment at room temperature for 5 minutes. Then samples were examined by flow cytometry at 488/530nm (Ex/Em).

3.2.12 Drug Loading

Methotrexate was dissolved in PBS (1mg/10ml) and stirred with FA/FITC-HNTs (200mg) for 12 hours. Then, the mixture was vacuumed for 24 hours and centrifuged. The bottom deposited FA/FITC-HNTs were collected and washed by PBS for 3 times and air-dried. The supernatant liquid was collected and stored at -20 °C for drug loading efficiency determination.

3.2.13 Drug Loading Efficiency and Drug Release

20 mg of drug loaded FA/FITC-HNTs were added into 2ml PBS. 1 ml of PBS was collected at certain time period and replaced by 1ml of fresh PBS. The collected samples were stored at -20 °C until they were measured by MTX Elisa kit (ENZ-KIT 142-0001, Enzo Life Science). Drug loading efficiency were determined by the following equation:

$$\text{Loading Efficiency} = \frac{\text{total amount of MTX} - \text{supernatant MTX}}{\text{total amount of MTX}} \times 100\% \qquad \text{Equation 3-1}$$

3.2.14 Target Specific Cancer Cells and Inhibit Cancer Growth

Methotrexate-loaded FA/FITC-HNTs (50ug/ml) were cocultured with murine colorectal cancer (CT26WT), osteosarcoma cells (K7M2WT), and pre-osteoblast cells (MC3T3-E1) separately at 48 wells tissue culture plates (1×10^5 cells/well). After 24hours incubation, cell viability of each cell type was assessed by MTS agent as above (3.2.6). Cells cultured without HNTs served as the control.

3.2.15 Statistical Analysis

Data were obtained from 3 parallel experiments and are expressed as mean ± standard deviation (S.D.). Each experiment was repeated 3 times to check the reproducibility if not otherwise stated. Statistical analysis was performed by two-tailed Student's t-tests between two groups. The significant level was set as $p<0.05$.

3.3 Results

3.3.1 Proper Dosage Determination

The fabrication method of FA/FITC-HNTs (bHNT) was reported in our previous study, [113] in which we did a live/dead assay and found that cell cytotoxicity was increased with bHNT loading concentration. In order to confirm the proper dosage range of bHNT, we employed MTS assay and XTT assay to assess cell proliferation and viability when cells co-cultured with pure HNTs and bHNT at different concentrations. Both tests presented similar results: cell viability changed with the concentration of HNTs nanoparticles. In the MTS assay (**Figure 3-4** A, B), cell proliferation was improved when the concentration of nanoparticles was below 100 μg/ml, but when the concentration increased to 150 μg/ml, the proliferation ability significantly decreased 20%. The XTT assay showed the similar results (**Figure 3-4** C, D), cell viability decreased with the increasing concentration of HNTs. But the XTT assay showed that CT26WT cells have a higher tolerance concentration to HNTs, the significant cytotoxicity exhibited above 200 μg/ml. Both results suggested that the highest dosage of bHNT is 150 μg/ml.

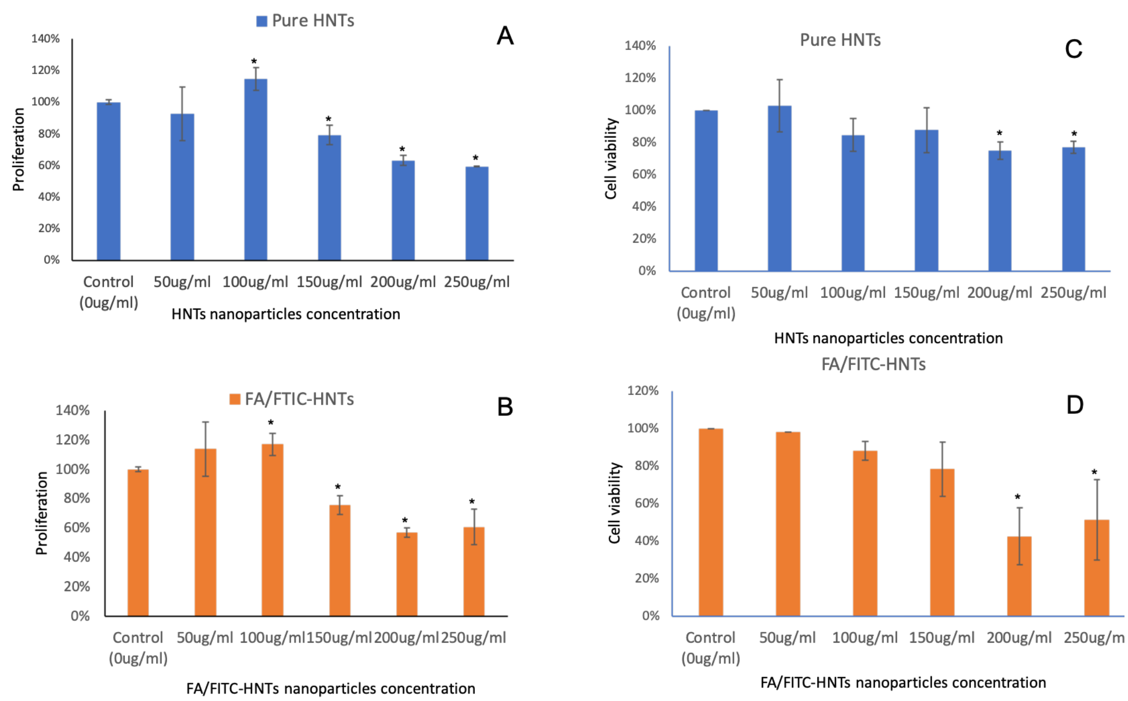

Figure 3-4: CT26WT cells cultured with pure HNTs (A) and bHNT (B) at different concentration then applied with MTS assay. Cell proliferation ability at each different concentration was calculated by comparing to the control group. CT26WT cells cultured with pure HNTs (C) and bHNT (D) at different concentration then applied with XTT assay. Cell viability at each different concentration was calculated by comparing to the control group. (error bar with standard deviation, n=6).

3.3.2 Nanoparticle Size Determination

Halloysite nanotubes are naturally formed nanoparticles, their original length is around 1-1.5 μm. Recent studies have used shortened HNTs [66,115,126]. Rong et al. introduced a detailed procedure to produce homogeneous and length controllable HNTs [127]. Thus, we hypothesize different sizes of HNTs would affect cell behaviors. Due to the low production of Rong's method, which is less than 1%, we fabricated the short HNTs in another way for larger yield. Dynamic light scattering (DLS) is the most commonly used technique to determine nanoparticle size, however, DLS prefers to analyze spherical nanoparticles instead of virgate nanotubes. Thus, we took the SEM of the HNTs and used Image J to measure their size and plotted the data into histogram graph (Figure 5). As it shown in **Figure 3-4**, the lengths of commercially-purchased HNTs were distributed in a wide range, the average size is 0.914±0.45 μm, n=102 (**Figure 3-5** A), while the size of short HNTs focus on 0.715± 0.25 μm, n=80 (**Figure 3-5** B). Compared the two different sources of HNTs, we can easily find the size distribution of shortened HNTs are more concentrated, which means they are more homogeneous. Size controlled nanoparticles could help to reduce the manual errors and provide accurate evaluation of its application in biomedical researches.

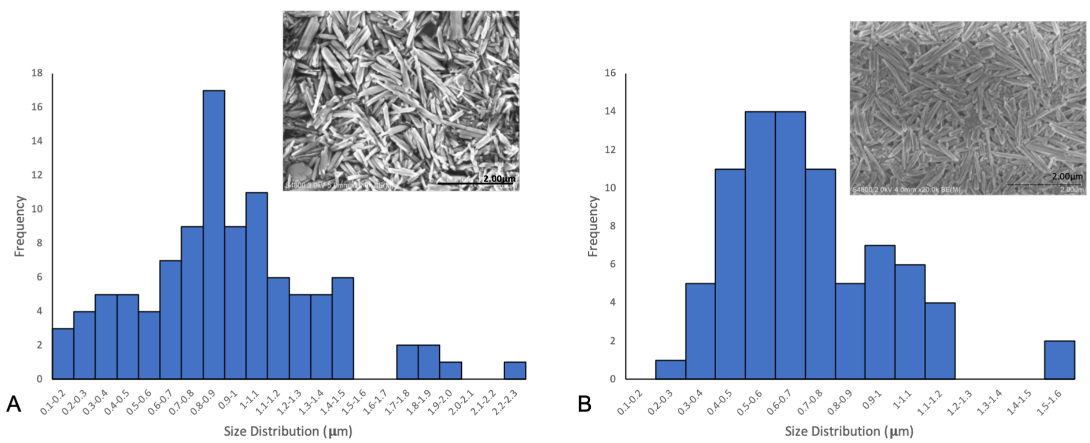

Figure 3-5: Histogram graph of size frequency of long HNTs (A) and short HNTs (B).

3.3.3 Cell Interaction to Long and Short HNTs

In our hypothesis, the size of HNTs would affect cell reaction to biofunctionalized HNTs. Cell uptake efficiencies of two difference size of HNTs were analyzed. Fluorescent intensity of cells (cell number = $4.46\times10^5 \pm 0.063\times10^5$) were detected after 24 hours incubation (**Figure 3-6** A). We monitored the fluorescent intensity changes in 24 hours. Cellular uptake efficiency for both size of HNTs exhibited similar changes along with time. In the end, more amount of short-HNTs are detected in cells, which indicates smaller size of HNTs are more easily to be absorbed by cells.

3.3.4 Apoptosis & Necrosis

Our previous cell cytotoxicity study had shown that cell viability significantly decreased when the concentration of HNTs reached to 150 μg/ml. In order to distinguish cell death mechanism, apoptosis or necrosis, we did a further study by incubating CT26WT cells with long and short bHNT and applied with Annexin V-FITC Apoptosis Kit. Fluorescents signals of apoptosis and necrosis were assessed by flow cytometry. As **Figure 3-6** B and C shows, in cells cultured with long bHNT, 20%±1.5% of cells death was caused by apoptosis and 10%±0.5% was caused by necrosis; cells cultured with short bHNT led to 23%±1.3% in apoptosis and 13%±0.6% in necrosis. Thus, apoptosis takes the main role in cell death. In addition, short bHNT results in a higher cell death percentage. This interesting finding leads us to think about the results of cell uptake efficiency. As shown above, cells accumulated shorter bHNT inside their body compare to long bHNT, and short bHNT results in more cells death. This phenomenon indicates that excessive accumulation of bHNT inside cells lead to apoptosis.

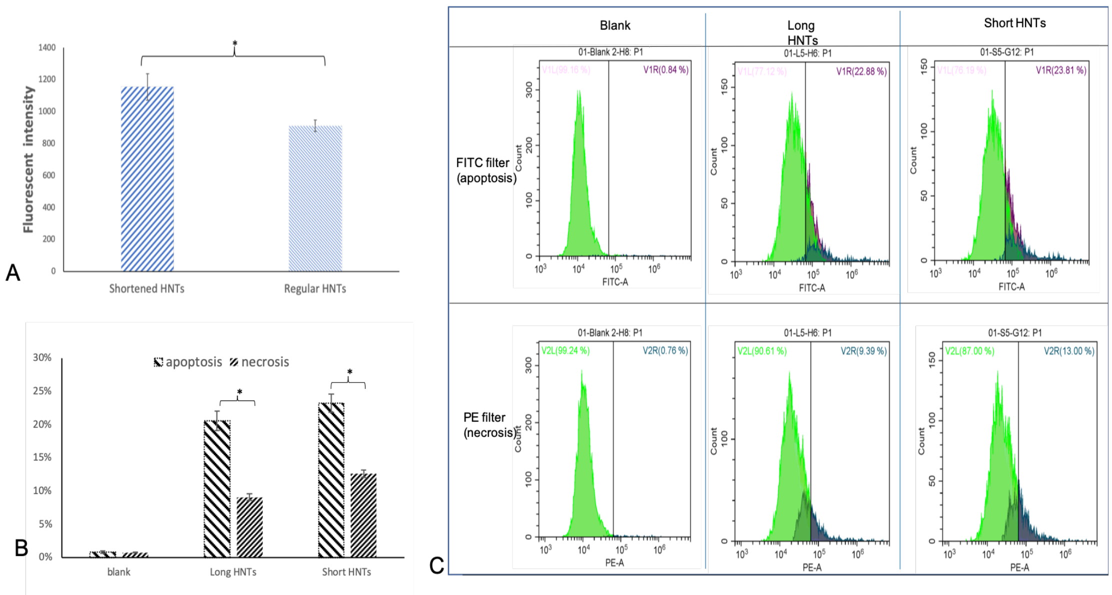

Figure 3-6: A. Fluorescent intensity of FITC detected from CT26WT cells after 24 hours incubation (cell number for each test = $4.46\times10^5 \pm 0.063\times10^5$, each group had 9 tests, error bar with standard deviation). B. CT26WT cells co-cultured with long or short bHNT, death caused by apoptosis and necrosis were assessed by flow cytometer. (cell number for each test $=3\times10^5$, each group had 6 tests, error bar with standard deviation) C. Flow cytometer observation applied with FITC filter for apoptosis (first row) and PE filter for necrosis (second row). Dead cells were in the right side of the shed line. Cell death percentage of apoptosis or necrosis was presented in the right corner of each graph.

3.3.5 Endocytosis Mechanism

After FA/FITC-HNTs binds to folate receptors, it may initiate cellular uptake mechanisms in two different ways, clathrin-mediated endocytosis or caveolae-mediated endocytosis. Chlorpromazine (CPZ) can the ability to disrupt clathrin on the cell membrane; while filipin can inhibit caveolae formation. CT26WT cells were pretreated with those two inhibitors and co-cultured with bHNT, their final fluorescent intensity was compared to cells without inhibitor treatment. As the result showed in **Figure 3-7** illustrates, the addition of CPZ promoted HNTs absorption in first 12 hours, then the cell uptake ability decreased. On other hand, filipin presented an inhibition in whole testing time period. This indicates cells absorption for FA/FITC-HNTs may mainly depend on caveolae-mediated endocytosis and assist with clathrin-mediated endocytosis.

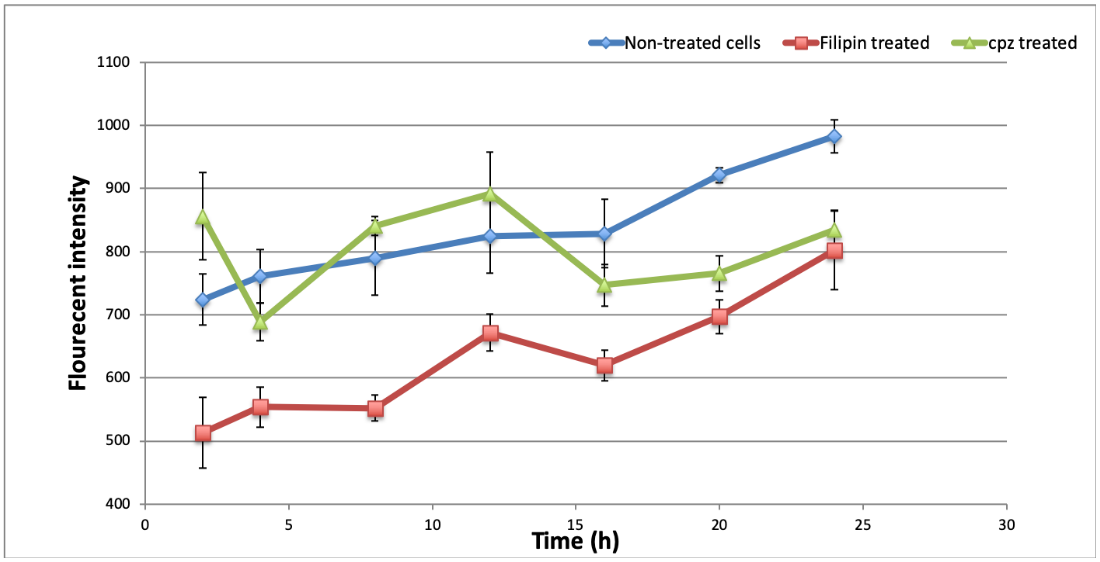

Figure 3-7: Fluorescent intensity of FITC included in cells that were pretreated by CPZ or filipin and cocultured with FA/FITC-HNTs for different incubation time. (error bar with standard deviation, n=6).

3.3.6 Intracellular Location of bHNTs

All above studies have shown bHNT were taken up by cells. In order to confirm the intracellular location of bHNT, we co-cultured CT26WT with bHNT for 24 hours, and stained the cell membranes with DiR, then detected the fluorescent bHNT by multi-photon microscopy. As shown in Figure 8, the red circular rings represent cell membranes, and the yellow particles represent bHNT. Multi-photon pictures provided a 3D picture of cells, according to the front view (**Figure 3-8** A and D) and side view (**Figure 3-8** B,C,E,F). These images show that some FA/FTIC- HNTs nanoparticles are embedded in cell membrane, and some of them are cell cytochylema.

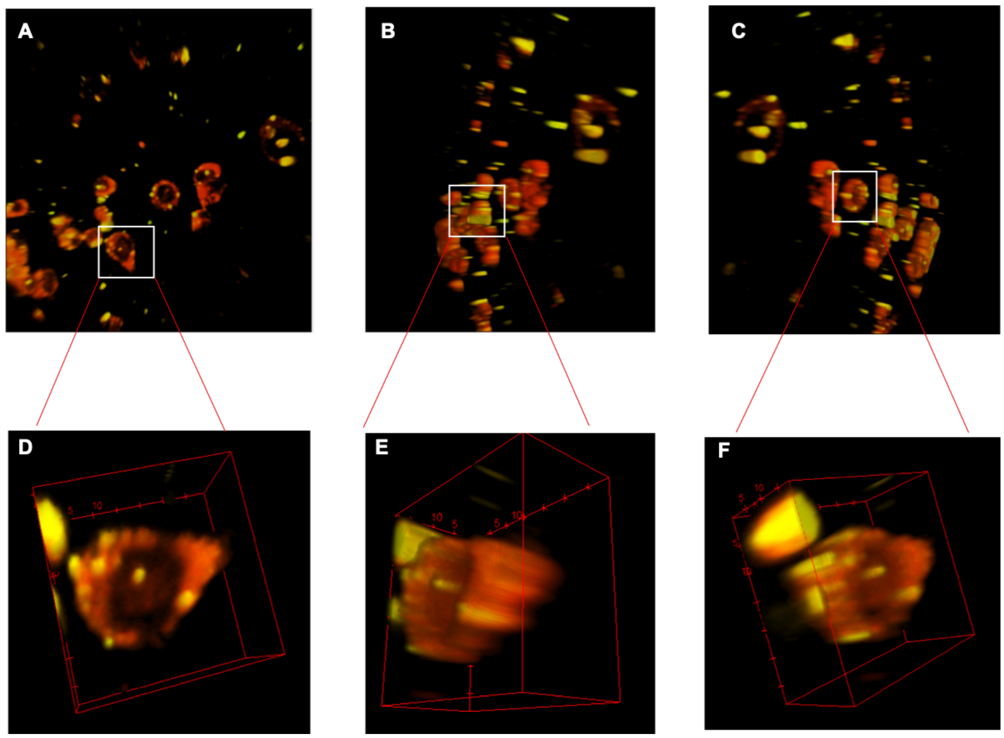

Figure 3-8: Multi-photon pictures of cells after exposed to bHNT, pictures are analyzed by ImageJ. CT26WT cells co-cultured with bHNT for 24 hours, then DiR dye was added for another 2 hours incubation. Cell membranes were stained by DiR dye and exhibited a red color at wavelength of 850nm. At this wavelength FITC exhibited a yellow color. The red circular rings represent cell membranes, and the yellow particles represent bHNT. The 3D pictures were captured for 36 microns in z with a 2 micron in each z step. A is the front view of the 3D picture for multiple cells, B and C are the side view of the 3D picture. D, E, and F are the zoom in pictures of the marked cell.

3.3.7 FTIR Analysis-Methotrexate and Drug Release

The above experiments indicate that our functionalized HNTs were successfully taken up by colon carcinoma cells (CT26WT). As it designed as a drug delivery system, we selected methotrexate (MTX) as drug model and loaded it into our functionalized FA/FITC-HNTs. Methotrexate is a commonly used anticancer drug to osteosarcoma. However, it is well-known for severe side effects. A cancer target drug delivery system is a promising strategy to reduce side effects and improve drug efficiency.

The modification of FA/FITC-HNTs were detected by FTIR. Halloysite is an aluminosilicate clay mineral ($Al_2Si_2O_5(OH)_4$), the Si-O stretching vibrations and Al-OH vibrations were represented at 1000-1130 cm^{-1}. Folic acid, FITC and MTX containing -NH and -OH bonds, their characteristic absorption is in the range of 3300-3500 cm^{-1}. The transmittance changes at 3300-3500 cm^{-1} indicated the successful grafting of FA, FITC, and MTX (**Figure 3-9**). The loading efficiency of MTX into HNTs is 34.74% ± 3.5%, its drug release profile is presented in **Figure 3-10**. Even through a burst release occurred in the first 20 hours, this drug delivery system extended drug release time to more than 96 hours.

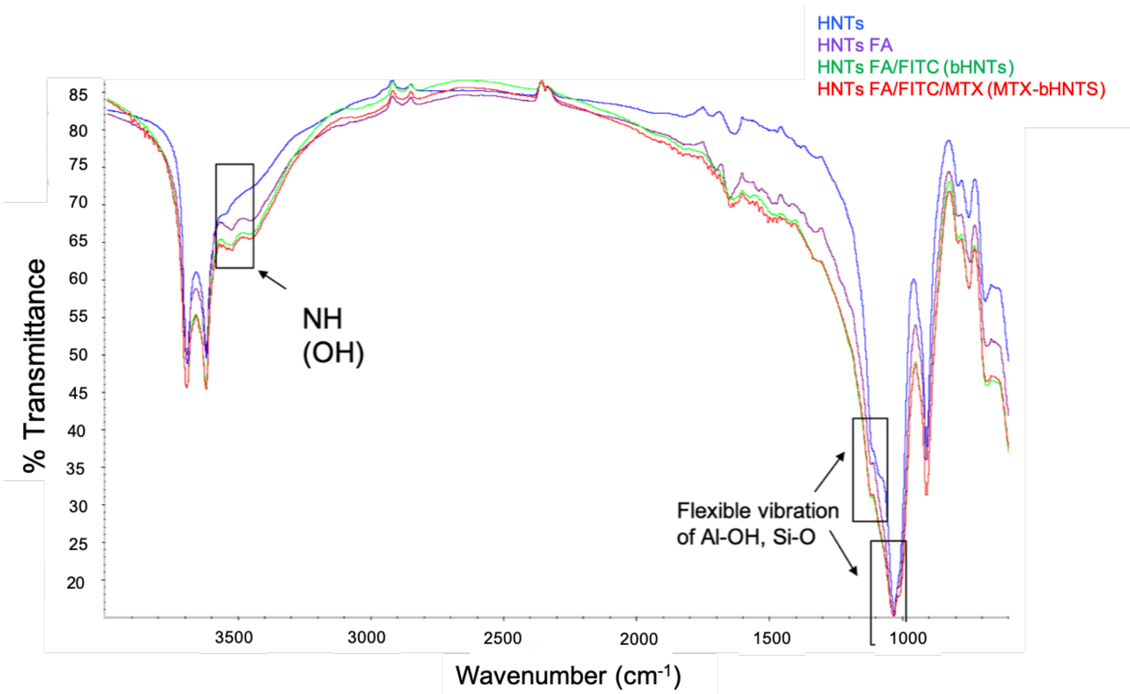

Figure 3-9: FTIR detection of pure HNTs (blue), HNTs-FA (purple), FA/FITC-HNTs (green) and FA/FTIC/MTX-HNTs (red).

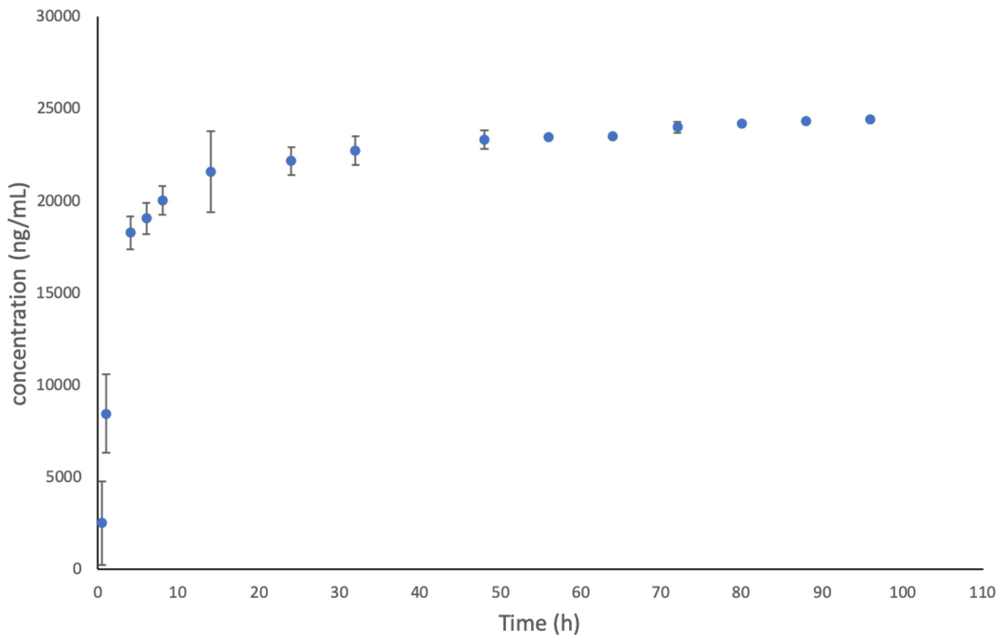

Figure 3-10: Accumulated drug release profile of methotrexate in 96 hours. (Error bar with standard deviation, n=3).

3.3.8 Cancer Target Drug Release

The bHNT (FA/FITC-HNTs) were developed to deliver drugs to specific cancer cells. One untransformed cell line, preosteoblast (MC3T3-E1), and two cancer cell lines, colon cancer cells (CT26.WT) and osteosarcoma (K7M2 wt.), were selected to assess specific target ability of bHNT and drug efficiency on cell growth inhibition. The results are presented in **Figure 3-11**. Methotrexate is one of the most active drugs used to treat osteosarcoma, but it has multiple side effects. In our study, methotrexate-loaded bHNT (FA/FITC/MTX-HNTs) significantly inhibited osteosarcoma cells (K7M2WT) proliferation at low concentration (50 µg/ml). Simultaneously, other types of cells were not hardly harmed at this condition. Most importantly, the bHNT did not show an aggressive attack to normal cells (MC3T3). In order to verify that the cell growth inhibition was caused by the loading drugs instead of the drug carriers (bHNT), we analyzed the cell viability by co-culturing cells with bHNT without drugs (FA/FITC-HNTs). The results showed that none of osteosarcoma or pre-osteoblast cultures were affected by the bHNT (**Figure 3-11** C). This finding is consistent to the previous study of CT26WT, that low dosage of bHNT did not present cytotoxicity (**Figure 3-4**).

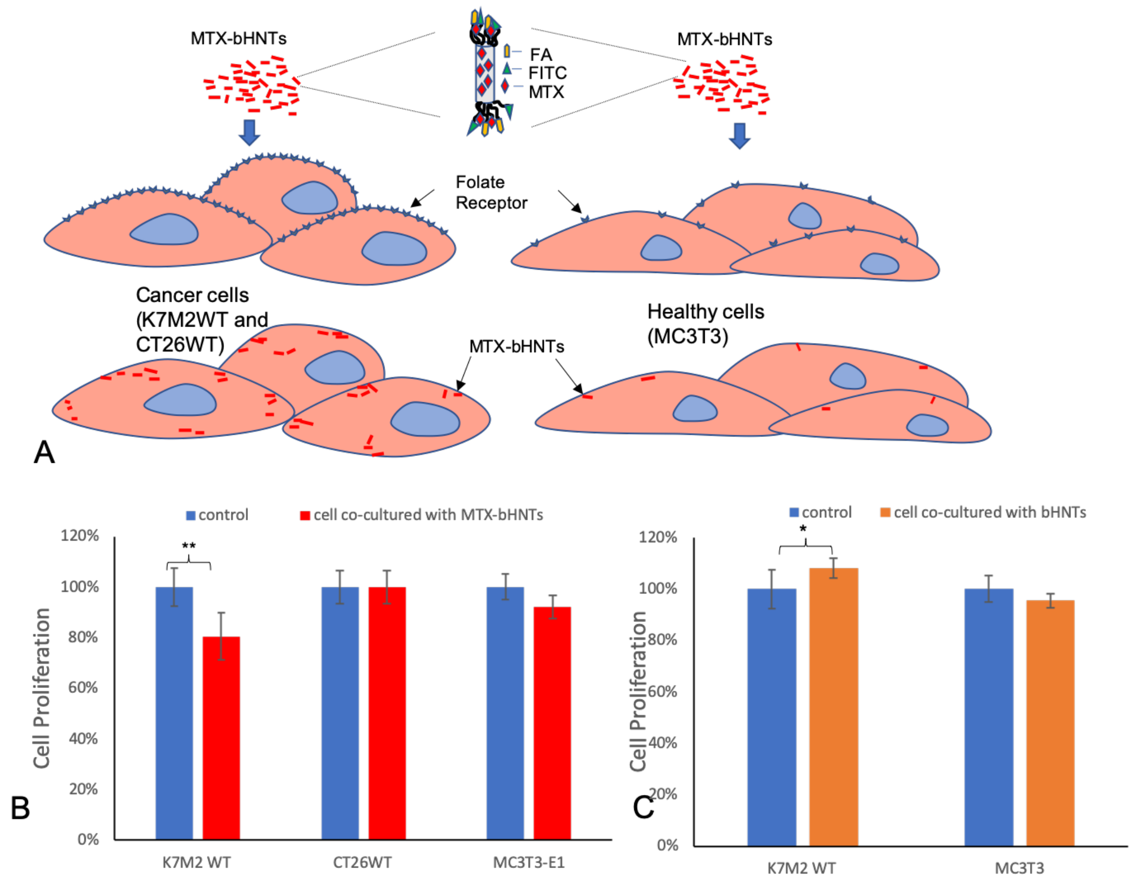

Figure 3-11: A. Schematic representation of osteosarcoma cells (K7M2WT), murine colon carcinoma cells (CT26WT) and preosteoblast cells (MC3T3) co-culturing with bHNT. B. Cell proliferation of above 3 types of cells after co-cultured with 50 µg/ml drug loaded bHNT for 24 hours. C. Cell proliferation of above 3 types of cells after co-cultured with 50 µg/ml bHNT for 24 hours

3.4 Discussion

Targeted drug delivery aims to decrease the side effects of highly toxic drugs through the delivery specifically to the target sites without harming surrounding healthy cells. The use of targeted drug delivery systems in chemotherapy has attracted a great deal of research interest. Various biomaterials have been used in developing drug delivery systems with targeting capabilities. Liposomes are small self-assembled spherical vesicles consisting of bilayer phospholipids. Due to their intrinsic biocompatibility, size, hydrophobic and hydrophilic character, and ease of fabrication, liposomes are a promising system for drug delivery [128], and several liposomal-based drugs have been approved [129]. However, liposomes are often unstable [130]. In order to improve their stability, excessive modification processes are often required [131]. which increases labor, material, and cost. Nanoparticles generated with biodegradable polymers belong to another group of potential drug delivery systems. In the process of nanoparticles production, the size, structure, physicochemical properties, drug loading and releasing mechanism can be modified as needed. However, toxic chemicals are usually involved in the fabrication of nanoparticles. These are hazardous to the environment and to the body's physiology [131]. Furthermore, most nanoparticle fabrication procedures are suitable for laboratory-scale fabrication but often are not scalable for industrial production.

Halloysite nanotubes are inexpensive, naturally formed eco-friendly nanoparticles with many desirable material properties [107]. Their physical and chemical stability, biocompatibility, and modifiable surfaces enable HNTs to be a key component in drug delivery [109,110,132]. Cationic therapeutic agents can be entrapped on the polyanionic surface of HNTs by chemisorption or encapsulated into their hollow lumens by vacuuming. Additional surface modification is often implemented to make multifunctional halloysite nanotubes [99,109]. HNTs can be functionalized with $-NH_2$ group using aminopropyltriethoxysilane (APTES) and then conjugated with folic acid. In a study of Guo et al., (2012) FA and magnetite nanoparticles (Fe_3O_4) were successfully grafted onto the HNT surface. The coated Fe_3O_4@HNTs exhibited a pH-sensitive drug release behavior under the electrostatic interaction between the cationic drug and the HNTs. [13] Wu et. al., (2018) also functionalized HNT with APTES and conjugated its surface with PEG and folic acid, and then drugs were loaded by physical adsorption. The final product (DOX@HNTs-PEG-FA) effectively inhibited tumor growth with reduced side effects observed in the heart, spleen, lung, and kidney [133].

However, one limitation of HNTs-PEG-FA is their drug loading efficiency is very low, only 3% for doxorubicin [133]. In contrast, our FA/FITC-HNTs system had a much higher drug loading efficiency, with methotrexate-loading over 30%. Another limitation is that the HNTs-PEG-FA drug delivery systems can target tumor cell but cannot avoid potentially impacting other healthy tissues. In contrast, FA/FITC/MTX-HNTs only inhibited the growth of osteosarcoma (K7M2WT) without inhibiting the growth of MC3T3-E1 and CT26WT cells. This result may be due to the use of different drugs, different methods for drug loading, or the different types of cells studied.

The intracellular pathway of HNTs was previously studied by Liu et al [126]. They also modified HNTs with APTES and labeled HNTs by FITC. Cells were treated by four different inhibitors respectively and cocultured with functionalized HNTs. They found both clathrin- and caveolae- dependent endocytosis take part in cells internalization of HNTs [126]. Also, Liu's group found that HNTs were transported by microtubules and actin microfilaments with involvement by the Golgi apparatus and lysosome [126]. Our finding is consistent with their study, but we observed that caveolae-mediated endocytosis took the major role and clathrin-mediated endocytosis only worked as a supplementary mechanism in HNT-DAS-FITC/FA endocytosis. This difference between our results and Liu's results may be due to different surface modification strategies.

A significant body of research has been done to in developing targeted drug delivery using HNTs [7,13,126,133,134]. Previously our lab has conducted studies on drug loading and release of MTX from HNTs from a polymer, nylon-6 [11].This study directly targeted delivery of MTX specifically to osteosarcoma cells and inhibited osteosarcoma cell growth without inhibiting proliferation in other cells types. We modified HNTs with DAS instead of the traditional modification of HNTs with APTES, which has several advantages [135]. The system developed by the Hu et al., (2017) uses FA-conjugated to PEG deposited on the HNT surface. Our system prevents the dissociation of FA from the surface by covalently linking it to DAS. HNT-DAS-FA/FITC has both an imaging and targeting agent covalently attached to the surface of the HNTs. By incorporating an imaging moiety in the system, the efficacy of the treatment option can be monitored. Additionally, the HNT-DAS-FITC/FA is modular, allowing the system to be applied to a range of targets.

Our HNT-based drug delivery system has the potential to provide localized and targeted therapy for the treatment of osteosarcoma that limits or reduces potential negative side effects, reducing patient costs and length of treatment and improving quality of life. The HNT interior can be loaded with a variety of anti-cancer drugs (or other chemotherapeutics) that serve as a "death cargo" designed to kill cancer cells while providing feedback imaging data on drug efficacy. The surface of the HNT can be modified with copper, iron or silver nanoparticles and used in photothermal therapy by converting light to heat inside tumor cells.

3.5 Conclusion

In summary, DAS-functionalized HNTs have a high drug loading efficiency (34.74% ± 3.5%). They are taken up by cells primarily though caveolae-mediated endocytosis and assisted by clathrin-mediated endocytosis. As far as authors are aware, we are the first to analyze the effects of HNT particle size on cell viability and have demonstrated smaller HNT size leads to increased cytotoxicity leading to cellular apoptosis. Compared to the typical size of HNTs, HNTs reduced in overall length were taken up by cells in greater amounts leading to cellular apoptosis. After conjugation with FA, MTX was effectively delivered to osteosarcoma. Most importantly, this is a specific target drug delivery; only osteosarcomas were affected, while the cell growth of murine colon carcinoma cells and pre-osteoblasts were not inhibited. All these results suggest that the DAS functionalized FA/FITC/MTX-HNTs may have a potential in targeting therapy for the treatment of osteosarcoma.

CHAPTER 4

ZINC LOADED HALLOYSITE COPPERATING WITH POLYLACTIC ACID FOR BONE REGENERATION

4.1 Introduction

Three-dimensional (3D) printing has been a popular technology used in bone tissue engineering due to its ability to print out porous scaffold with designed structure with desired porosity and pore size. 3D printing associates with computer-aided design (CAD) to generate a 3-dimentional solid object from a digital data file, which can be used to create highly detailed and patient-specific models for surgical planning. Biomaterials commonly used in 3D printing are polymers (synthetic and natural), ceramics, and metals. Each biomaterial has specific physicochemical properties, processing methods, and cell-material interactions [136]. Polymer materials are more popular than others due to their tunable properties, low melting point, low weight and processing flexibility. Although polymers can be printed for complicated geometric structure, lack of mechanical strength and functionality limited their wide applications; therefore, development of composite materials that are compatible with available printers and that provide desirable mechanical and functional properties has attracted tremendous attention.

Polylactic acid (PLA) is a popular biomaterial used for 3D printing. It is a thermoplastic polymer that is derived from fermented corn starch, cassava starch or sugarcane. It is an ecofriendly bioplastic as it is completely biodegradable and consists of renewable raw materials [137]. PLA has two optical isomers, D and L. PLLA has a melting point of 175-178°C and a glass transition temperature of 60-65°C. This material exhibits high tensile strength, low elongation and high modulus, which enable it to be a good candidate for load-bearing applications, such as orthopedic fixation and sutures [137]. PLLA can last more than 2 years in the body [137]. PDLA is an amorphous polymer, which has a lower tensile strength, higher elongation and faster degradation time. Those features make it more attractive as a drug delivery system [137].

Bone is a porous tissue, and its interconnected pores allow cell migration and proliferation, as well as vascularization. Scaffold properties such as adequate pore size, porosity, interconnectivity, and bioactivity have strong influence on bone engineering as well. In addition, the porous structure helps biomaterial to interlock native bone tissue, providing a greater mechanical stability at insert site [138]. Porous bone scaffolds can be made by a variety of methods: salt leaching [139], chemical/gas foaming [140], freeze-drying [141], and sintering [142]. However, pore size, pore distribution, porosity, and pore interconnectivity cannot be precisely controlled in these approaches [143]. Such scaffolds can be designed and fabricated using 3D printing.

In order to optimize the integration between scaffolds and native tissue, osteogenic scaffold should mimic bone morphology, structure and functions. Bone consisted by 10% of bone cells and 90% of bone matrix [144145]. The main components of bone matrix are hydroxyapatite [$Ca_{10}(PO_4)_6(OH)_2$] (50-70%) and organic matrix (20-40%) [146]. Collagen type I takes 95% of total organic matrix [147]. Trabecular bones have a porous structure with 50-90% porosity and pore size of 1 mm in diameter [148], while cortical bones has a solid structure with a lower porosity of 3-12% [149].

From a previous study, porosity did not affect cell attachment, but high porosity promotes cell proliferation, due do its bigger pore space and facilitation of oxygen and nutrients transportation [150]. In contrast, lower porosity stimulates alkaline phosphatase activity and more osteocalcin secretion [150]. Pore size also plays an important role in extracellular matrix production and the progression of osteogenesis. Small pores (90-120μm) generate hypoxic conditions and induce osteochondral ossification, while large pores (350μm) allow high oxygenation and vascularization which lead to direct osteogenesis [151]. Smaller pores (<100μm) enhance cell proliferation [152153]. while larger pores (>100 μm) are good for cell migration. Based on the study of Hublber et al., the minimum requirement of pore size is 100 μm for cell growth and migration [154], however, pore sizes >300 μm are recommended due to enhanced bone formation and vascularization [155156].

The pore size and porosity also play an important role in implants degradation. A proper balance between bone regeneration and degradation of biomaterial is desired [157]. However, the mechanical properties of implants are decreasing with the degradation of biomaterials. Therefore, various hybrid materials have been explored to build 3D structure to archive desirable properties. For instance, the reinforcement for polymer usually archived by addiction of particle [158], nanocomposites [159] and fibers [160]. In this study we used halloysite nanotubes (HNTs) to improve PLA mechanical properties. HNTs are naturally formed nanotubes with a hollow tubular lumen. Their inner diameters are 10-30nm and their outer diameters are 50-70nm. Their lengths typically vary in the range of 0.5-1.5 μm [2]. HNTs have been incorporated with variety of polymers, such as poly(butylene succinate) [161], rubber [162], epoxy [163], poly(methyl-methacrylate) [10], alginate [51] and chitosan [49]. HNTs improved their mechanical strength, increased surface toughness and thermal stability. Therefore, we also employed HNTs as our filler to reinforce PLA 3D scaffold.

Besides pore size, geometry, porosity and mechanical strength, surface properties such as surface charge, topography, and chemistry are also critical parameters to affect the success of the implanted scaffolds. At an early stage, bone ingrowth generated from the periphery of scaffolds and presents a negative gradient in mineralization toward the inner parts [164]. Thus cell adhesion is the premier stage for bone regeneration. Many studies have proved that surface charge [165166], roughness[167], surface adsorbed proteins, and hydrophilicity/hydrophobicity [168] greatly influence on the cell attachment and direct cell behaviors. PLLA is a versatile, biodegradable, and FDA approved biomaterial [137], but an extra process is required to neutralize its hydrophobicity and low surface energy to improve cell adhesion.

In this study, PLA was blended with metal-doped halloysite nanotubes (HNTs) in order to improve the mechanical properties of 3D printed scaffold, simultaneously, halloysite nanotubes have been reported to enhance osteogenic differentiation [169]. As previously mentioned large pores and high porosity result in direct osteogenesis [151,155,156]. Therefore, we printed the scaffold for 60% porosity with an average of 600 μm pore size. Scaffold mechanical properties and cell-material interactions were studied. The aim of this study is to generate a 3D printed scaffold to support bone regeneration and prevent bacterial contamination, which may be potentially used for bone defect therapy in a clinic. Therefore, we also coated the 3D printed scaffold with antibody to prevent surgical contamination. The antibacterial ability of drug coated scaffold was assessed after 3 weeks stock time.

4.2 Materials and Methods

4.2.1 Material Preparation

Four compositions were tested in this study: PLA, PLA+HNTs, PLA+HNTs/Zn, and PLA+HNTs/Zn+Gentamicin. In order to print them by 3D printer, all the above materials were made into filaments. PLA were extruded by Noztek at 175°C and resulted in the filaments with diameter of 1.75±0.05mm. In order to archive a uniform distribution of HNTs in PLA, 10 μl of silicon oil were added into 20g PLA and vortexed for 10 minutes, then 1.2g of HNTs were added and continually vortexed for another 10 minutes. The mixture of PLA+HNTs were poured into Noztek and extruded at 170 °C. Filaments of PLA+HNTs/Zn made in the same way as PLA+HNTs, the difference is HNTs loaded with Zn, the Zn loading percentage is 30% w/w. The mixture of PLA+HNTs/Zn was extruded at 165 °C. Group of PLA+HNTs/Zn+Gentamicin were fabricated as dipping the 3D printed PLA+HNTs/Zn discs into 100mg/ml gentamicin solution for 24 hours.

4.2.2 Zinc Loaded into HNTs

Zinc nanoparticles (Zn nps) were deposited on HNTs by thermal decomposition of the metal acetate, as depicted in **Figure 4-1.** Zinc oxide (ZnO) and excess of acetic acid was reacted using a magnetic stirrer at 50°C. Acetic acid was replenished in the system over time for 12h, and the mixture was boiled. The zinc acetate ($Zn(OAc)_2$) obtained was filtered using Whatman NO.1 filter paper[170].

20g of ($Zn(OAc)_2$) were mixed with 10g of HNTs in 50 ml water and magnetically stirred for 12h. The product was decanted and separated using centrifugation and heated at 350°C for 2h which led to thermal decomposition of the metal acetate attached to the HNTs to ZnO-HNTs[171].

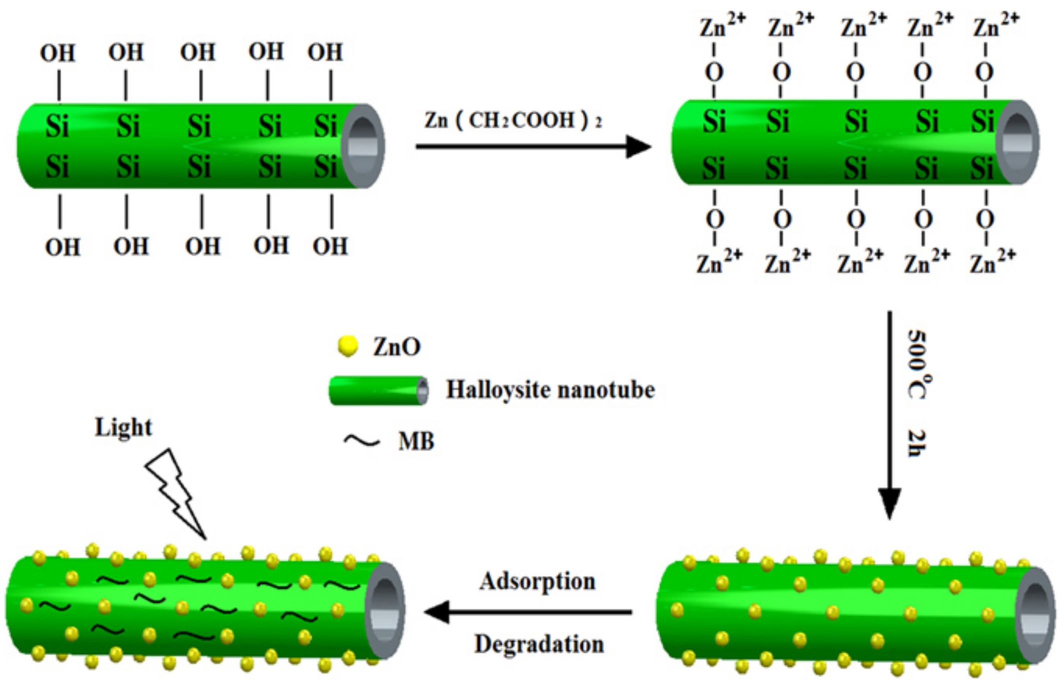

Figure 4-1: Facile synthesis and characterization of ZnO nanoparticles grown on halloysite nanotubes for enhanced photocatalytic properties.

4.2.3 <u>3D Printing</u>

The above produced filaments were 3D printed into desired structure by ENDER 3 printer at 225°C. The discs were designed to be 6×6×2 mm with a pore size with 0.6mm (**Figure 4-2**). The diameter of inside lattice girders is 0.6mm.

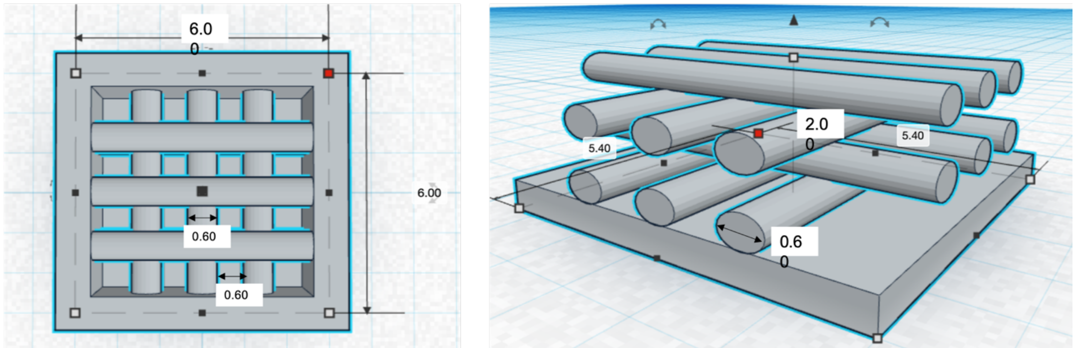

Figure 4-2: The CAD graph of 3D printing structure.

4.2.4 Compressive Test

Compression testing was applied by CellScale Unit. 3D printed discs were compressed at a speed of 10 mm/min with a 200 N load cell. The strain and stress prolife were collected. At least 3 tests were performed for each composition.

4.2.5 Morphology and Surface Characterization

The morphology of 3D printed scaffolds was observed by scanning electron microscope (SEM) and laser confocal microscope. The surface coatings were confirmed by EDS and FTIR. The hydrophilicity change with coating was determined with contact angle measurement.

4.2.6 Porosity

The open porosity of 3D printed scaffold was calculated though liquid displacement. One 3D scaffold was immerged into 1.0 ml (V_1) of DI water, then a series of vortexing and sonication were applied to force the liquid get into the pores of the scaffold. The total volume of scaffold and DI water was measured (V_2), after the water was removed, the scaffold and the remain volume of DI water was measured (V_3). The final porosity of the scaffold was calculated as below:

$$\text{porosity} = \frac{V1 - V3}{V2 - V3} \qquad \text{Equation 4-1}$$

4.2.7 Cell Culture

Pre-osteoblast (MC3T3-E1) cells were selected to analyze cell differentiation when they were cultured in the 3D printed scaffold. MC-3T3 E1 (ATCC) were cultured in alpha modification of Eagle's medium (α-MEM, Hyclone) with 10% fetal bovine serum (FBS) and 1% Pen/Strep antibiotic (Life Technologies). Cells were cultured in a humidified incubator at 37 °C and 5% CO_2 level.

4.2.8 Surface Treatment of 3D Printed Scaffold for Cell Culture

Three strategies were used to improve scaffold surface hydrophilicity: 1) 3D printed scaffolds were immersed into the Fetal Bovine Serum (FBS) for 24 hours, which labeled as FBS in below. 2) 3D printed scaffolds were treated as Strategy 1 then immerged into 10 N NaOH for 30 minutes and washed by DI water, which were labled as FBS+NaOH. 3) After 3D printed scaffolds were treated as in Strategy 2, they were incubated in FBS again for 24 hours, which are labeled as FBS+NaOH+FBS.

Pre-treated 3D printed scaffold was put into 48 wells plate. Each well had one disc and was seeded by MC3T3 cells at 1×10^5/well. Cells were cultured in a humidified incubator at 37 °C and 5% CO_2. Cell behaviors were evaluated at Days 7, 14 and 21.

4.2.9 Cell Attachment Stain

Cells were incubated with scaffold for 24 hours and co-cultured with Hoechst 33342 for 30 minutes at 37 °C and 5% CO_2. Then cells were fixed by 4% paraformaldehyde for 15 minutes and stained by actin-stain 488 phalloidin according to the manufacture's protocols. Cell nucleus and actin filaments were observed by fluorescent microscope under DAPI and FITC filter, respectively.

4.2.10 Cell Proliferation

Cell proliferation was tested by MTS reagent. Cell were incubated as above, and at Day 14 and 21, 40 μl of MTS was added into cell culture plates and incubated for 2 hours at 37 °C in darkness. 200 μl of supernatant of each sample were transferred to 96-well plates and read absorbance values at 490nm by microplate reader. Cells cultured without scaffold used as the control.

4.2.11 Cell Differentiation

Osteocalcin Quantikine ELISA kit (R&D system) was employed to measure osteocalcin (OC) as a marker for osteogenic differentiation. Three scaffolds were assessed for each condition. Cell culture supernatant were collected for ELISA analysis. ELISA plates were processed according to manufacturer's protocols. A standard curve was generated to determine osteocalcin concentration. Controls scaffolds were incubated without cells set as negative control and cells cultured in regular 2D condition were used as positive controls.

4.2.12 Mineralization-Alizarin Red Staining

Matrix mineralization will be assessed by Alizarin Red S (ARS) staining. Cells on scaffolds were fixed with 4% paraformaldehyde for 15 minutes at room temperature, then stained with 2% ARS for 30 minutes. The samples were washed by DI water 4 times and observed under a microscope. Digital images of stained scaffolds were acquired using a brightfield microscope. Cells cultured in regular 2D condition were set as controls.

For quantification, 3D printed discs were transferred to 1.5 ml microcentrifuge tubes and immersed in 200 µl of 10% acetic acid, after which they were incubated for 30 minutes at a horizontal shaker at speed of 500 rpm/min. All the microcentrifuge tubes were vortexed for 30 seconds, and after 10 minutes incubation at 85°C, they were cooled down in ice for 5 minutes. Tubes were centrifuged at 20,000xg for 15 minutes, 200 µL of the supernatant were transferred to a new 1.5 ml microcentrifuge tube and neutralized the pH with ~75 µL 10% Ammonium hydroxide to make pH in the range of 4.1-4.5. A standard curve was generated to determine the Alizarin Red Staining. 50 µL of standard and sample were added into a 96-well plate and read at OD405.

4.2.13 Picrosirius Red Staining

Picrosirius Red is a specific collagen fiber stain that is capable of detecting thin fibers. Media was removed from the cell culture plates and washed with DPBS before being fixed by 4% paraformaldehyde. These fixed cells were stained with Picrosirius Red for quantifying the amount of collagen secreted. Picrosirius stain was added into each well and removed after an hour incubation at room temperature. The cells were rinsed with 0.5% acetic acid solution twice and absolute alcohol twice. Digital images of stained scaffolds were acquired using a brightfield microscope. Cells cultured in regular 2D condition were used as controls.

4.2.14 Antibacterial Efficiency

Staphylococcus aureus (*S.aureus*) gram positive bacteria maintained in tryptic soy agar was used in this study. For testing, the bacterial strain was cultured in nutrient broth and plated on Muller-Hinton agar plates at 37°C overnight after which a single colony was picked up using a sterile toothpick and suspended in saline solution and diluted to 0.5

McFarland standard (1.5 x 10^8 CFU/ml). The antibacterial potential was evaluated against *S. aureus* using a microdilution broth assay. 3D scaffolds were immersed in 24 well plates containing 1ml/well Muller Hinton broth with 20µL of 0.5 McFarland standard *S. aureus*, the plates were put on a shaker at 37°C. The absorbance of 100µL solution at 630nm was recorded after 12 hours incubation.

4.2.15 Statistical Analysis

One-way ANOVA or Student T-test was used for statistical analysis. Data were expressed as mean ± standard error. A p-value less than 0.05 was considered statistically significant.

4.3 Results

4.3.1 Morphology of 3D Printed Scaffold and Surface Characteristics

All the filaments were printed into pre-designed structure with a pore size of 600 µm*600 µm and a layer height of 600 µm (**Figure 4-2**). However, due to the limitation of the 3D printer, the resolution changed slightly. The precisely pore size was determined by laser confocal microscope (**Figure 4-3**). Based on measurement of 60 pores from 20 3D printed scaffolds the final pore size is 584.16±95.28µm in vertical distance and 620.39±93.03µm in horizontal distance and with a porosity of 60.22±9.5%.

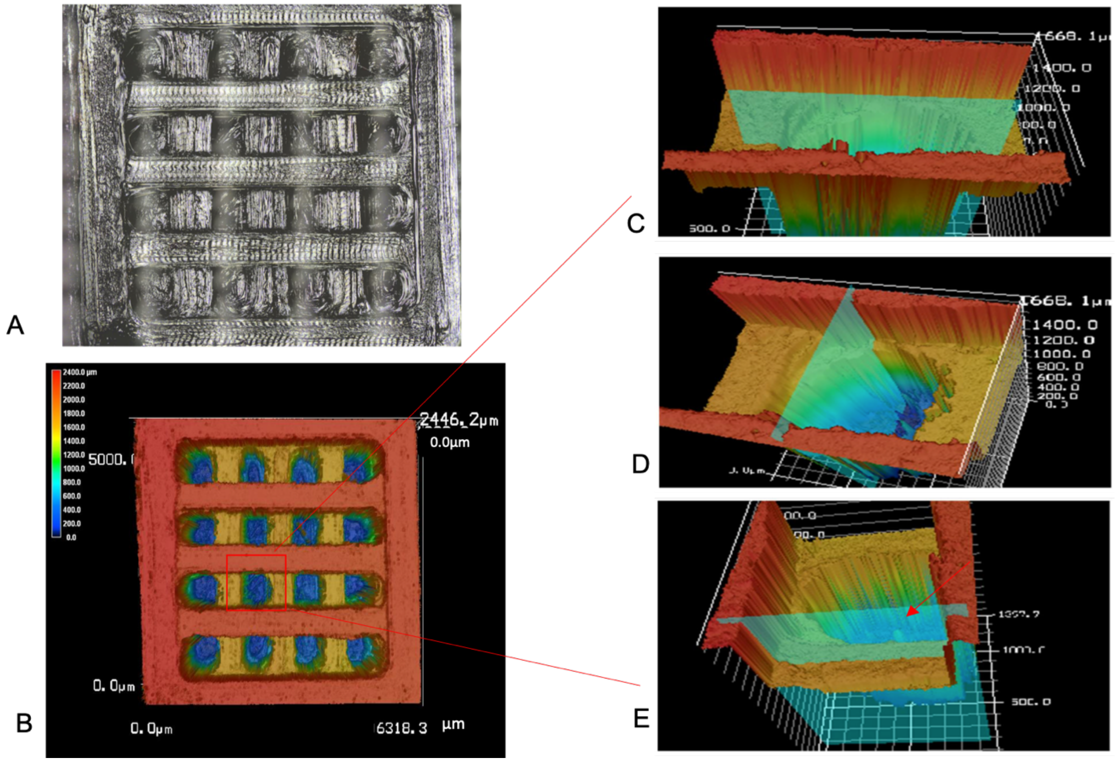

Figure 4-3: A. optical & laser combined picture of 3D printed disc. B. Laser confocal image of 3D printed disc. C. Horizontal section of selected pore, the horizontal distance was measured (584.16±95.28 μm, n=60). D. Vertical section of selected pore, the vertical distance was measured (620.39±93.03μm, n=60). E. Vertical section of selected pore, the layer thickness was measured (423.15±82.7μm, n=60).

In order to improve cell adhesion, the hydrophobic surface of scaffolds was treated by FBS, FBS+NaOH and FBS+NaOH+FBS respectively. The deposition of each treatments was determined by EDS and their affection on surface was observed by SEM (**Figure 4-4**). At least 3 samples were detected for each treatment. Fetal bovine serum is the most commonly used serum to support cell growth *invtro*; it contains a variety of proteins and inorganic ions, such as sodium (Na), chlorine (Cl), and nitrogen (N). In order to confirm the deposition of FBS and NaOH, we detected them on the surface of the 3D printed scaffold. Their distribution on the surface is presented in **Figure 4-4**. Carbon (C) and oxygen (O) were distributed all over the scaffold, as they are the main components of PLA. Na, Cl, and N can hardly be detected on the surface of naked PLA, while their deposition on other three groups varies due to different coating strategies. In order to accurately assessment of the surface modification efficiency for each strategy, we compared their deposition amount of Na (**Figure 4-5**), because both FBS and NaOH have Na. In our hypothesis, the deposition of Na would increase with each treatment. However, compared to the group modified with FBS along (1.65±0.3%, n=3), the addition treatment of NaOH (FBS+NaOH) decreased, rather than instead, the Na deposition it decreased (1.39±0.2%, n=3).The surface modified by FBS+NaOH+FBS has the highest accumulation of Na (2.45±0.15%, n=3), indicating that even though Na^+ from NaOH did not deposit on the surface, its remains attracted more deposition of third layer of FBS.

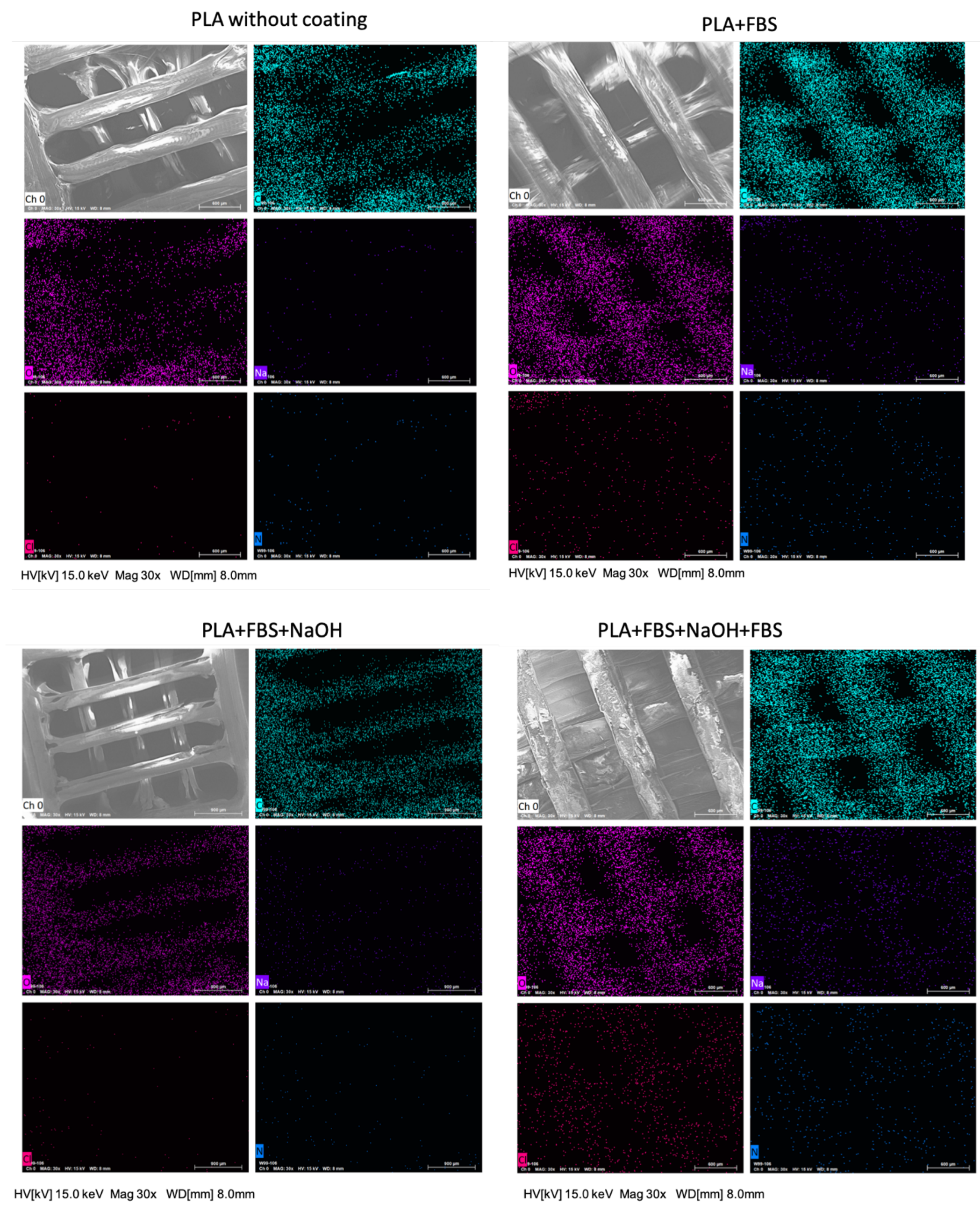

Figure 4-4: The SEM images and EDS element analysis for 3D printed scaffold. The first picture of each group is the SEM images. Then the EDS graph for each element distribution. The distribution of C and O presented the similar pattern as the scaffold, due to they are the main elements consist PLA. In the EDS pictures of Na, Cl, and N, there are only few dots are presented in the group of PLA without coating and PLA+FBS+NaOH. In contrast, those elements presented a scaffold pattern in the group PLA+FBS and PLA+FBS+NaOH+FBS.

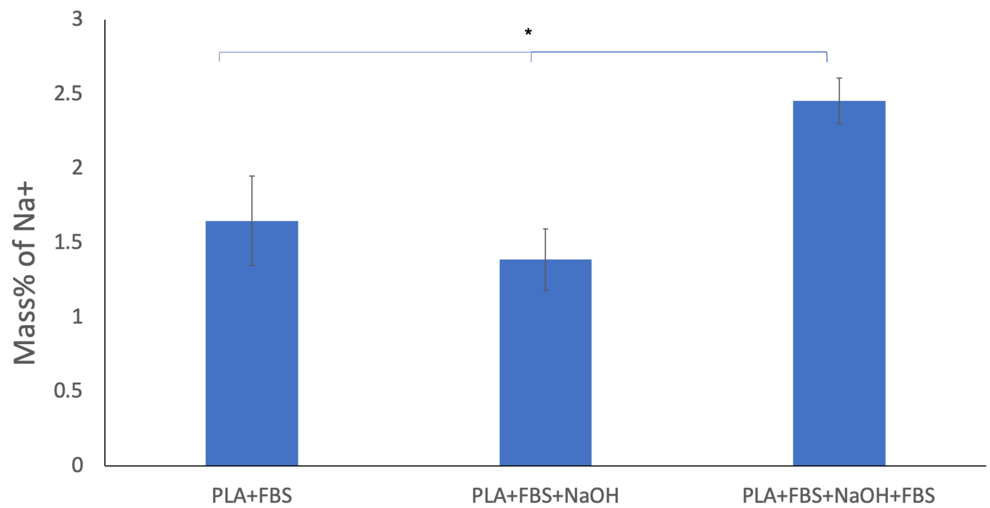

Figure 4-5: Deposition of Na for three modifications. (error bar with standard deviation, n=3, p<0.05).

Surface modification aims to increase the hydrophilicity of scaffold, which can be detected by contact angle. In our hypothesis, the contact angle would keep decreasing as the hydrophilicity would be improved with each treatment. However, the changes of contact angle showed the similar change trendline as the Na deposition. The scaffold hydrophilicity increased after FBS treatment, but decreased with the treatment of FBS+NaOH, and increased again with the treatment of FBS+NaOH+FBS (**Figure 4-6**). One interesting phenomenon happened in the test of FBS+NaOH+FBS group, when water was dropped on the scaffold surface, it spread on the disc surface so fast. Because the surface turned to be highly hydrophilic.

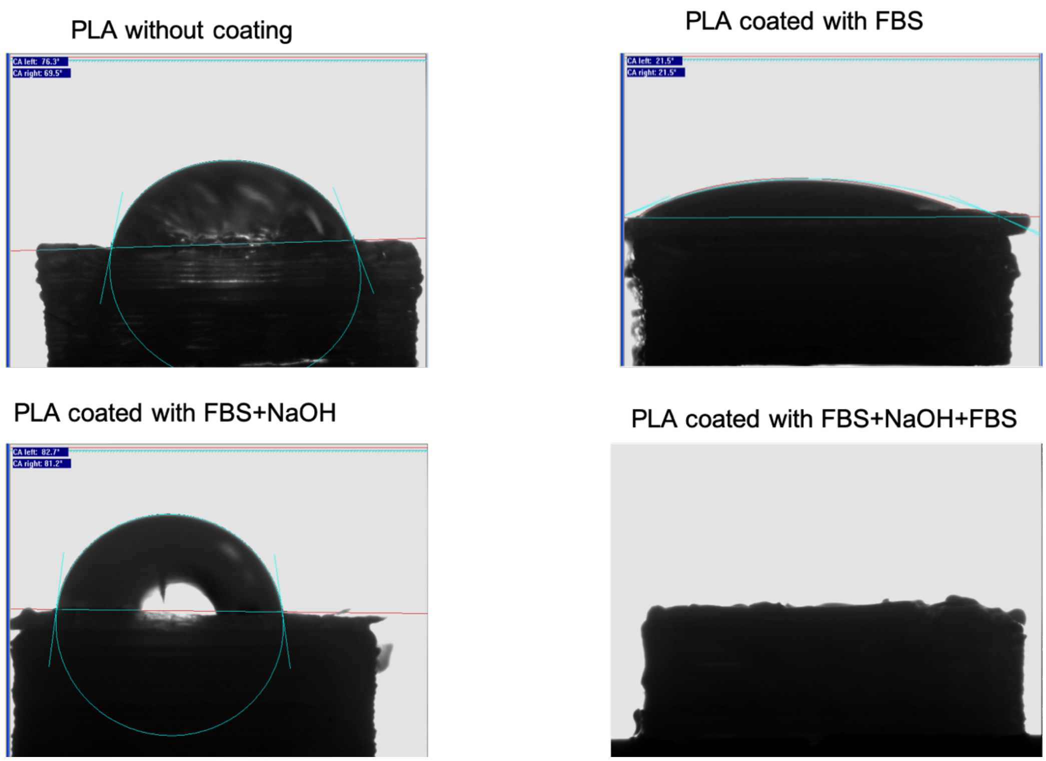

Figure 4-6: Contact angle of different surface modifications. The average contact angle for PLA without coating is 66.4°±9.8° (left) and 61.7°±7.2° (right); for PLA coated with FBS is 24.4°±5.2° (left) and 26.2°±4.1° (right); for PLA coated with FBS+NaOH is 82.5°±9.8° (left) and 82.4°±10.4° (right); and for PLA coated with FBS+NaOH+FBS, no data could be recorded due to the highly hydrophilicity.

4.3.2 Compressive Strength

In order to improve the mechanical properties of 3D scaffold, we added HNTs into PLA. Several studies have reported HNTs were able to improve biomaterials' mechanical properties [49,163,169]. Therefore, we expected the addition of HNTs and zinc loaded HNTs to increase PLA compressive strength. However, due to the limitation of the instrument, the maximum force it can provide is 200N, and at this force, none of the scaffolds broke. Compressive modulus was calculated from stress and strain (**Figure 4-7**). ANOVA analysis showed no significant difference among the three groups.

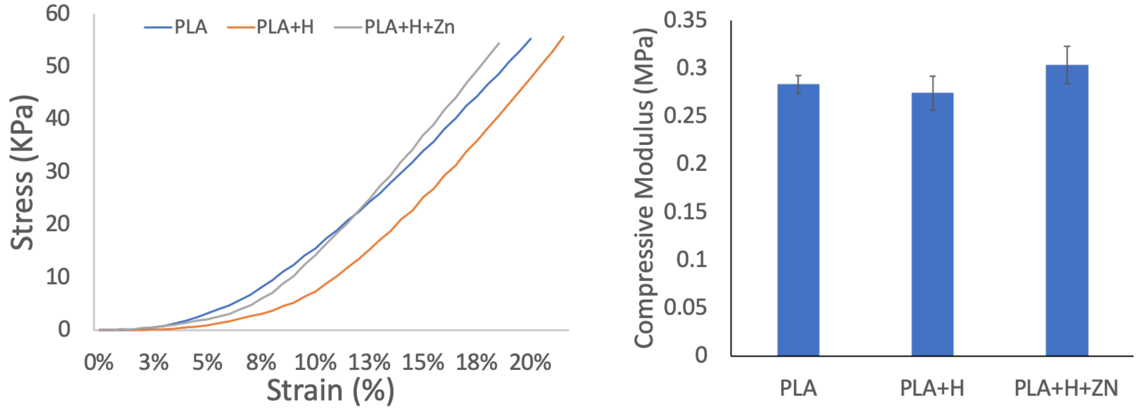

Figure 4-7: Stress vs. Strain profile and the compressive modulus of PLA, PLA+H, and PLA+H+Zn. The compressive modulus: PLA=0.28±0.01 MPa, PLA+H=0.27±0.02 Mpa, PLA+H+Zn=0.30±0.02 Mpa. (error bar with standard deviation, n=5).

4.3.3 Cell Adhesion

Three modification strategies exhibited different surface characters. Their influence on cell adhesion was studied by incubating cells with PLA, PLA+FBS, PLA+FBS+NaOH, PLA+FBS+NaOH+FBS for 24 hours and staining the cell nucleus and actin filaments. No cells detected on the uncoated surface of PLA, so we did not include a picture of this group. In contrast, all three coating strategies attracted cell adhesion, as shown in **Figure 4-8**. In addition, cell growth follows the scaffold direction. By comparing the cell nucleus number (DAPI) and actin fiber (FTIC) exhibition, it can be easily found PLA+FBS+NaOH+FBS has the best performance, while PLA+FBS+NaOH has the least cell adhesion. This finding is consistent to our previous surface character studies. Therefore, we coated all of our 3D scaffolds with FBS+NaOH+FBS for further cell behavior studies.

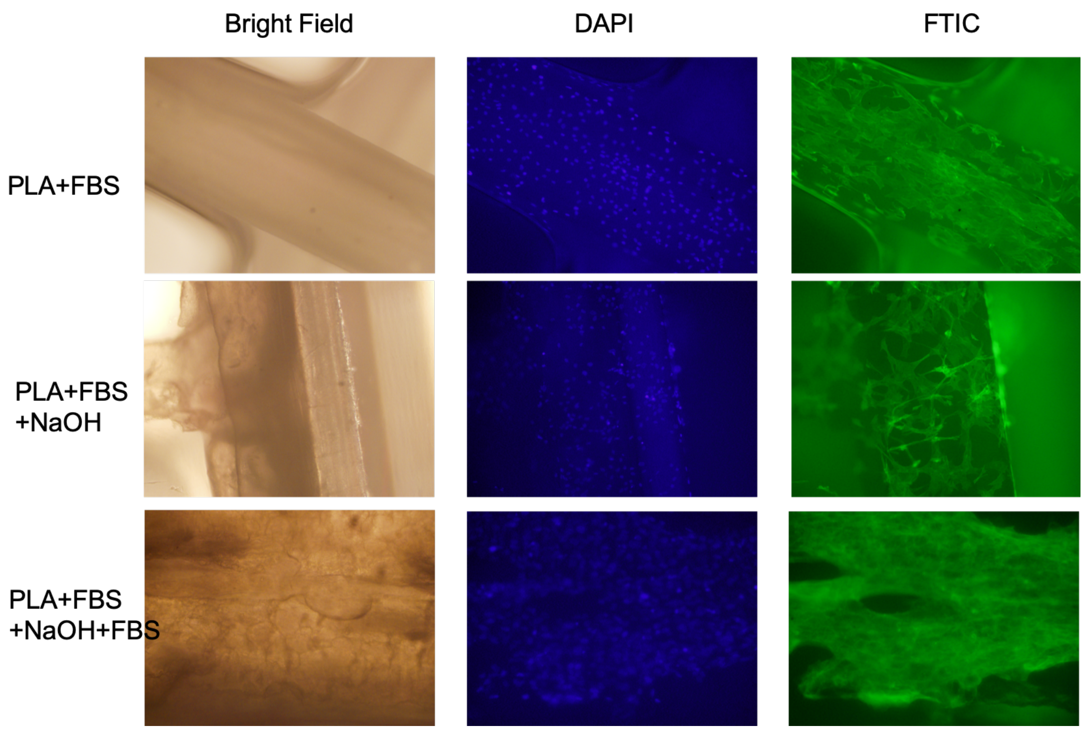

Figure 4-8: Cell adhesion on PLA with three coating strategies. First column is the bright phase. Second column is fluorescent pictures under DAPI filter, which represents cell nucleus. Third column is the fluorescent pictures under FTIC filter, which represents the actin fibers

4.3.4 Cell Proliferation

Cell proliferation was assessed after 7, 14, and 21 days incubation (**Figure 4-9**). In first week (D7), cell proliferation on 3D scaffold is not as good as conventional 2D cell culture, except scaffold composed by PLA. As incubation time increased, cell proliferation ability increased. After three weeks (D21) incubation, 2D and 3D cell cultures were significantly different. This is because 3D structure enables cell migration to the extra vertical plane, compared to 2D, the 3D structure has more adhesion surface. In order to decrease the risk of contamination, we coated the 3D printed scaffold with an antibiotic, gentamicin. Gentamicin inhibited cell growth in first 2 weeks, but in the third week, the control group and gentamicin coated ones (PLA+H+ZN+G) are not significantly different.

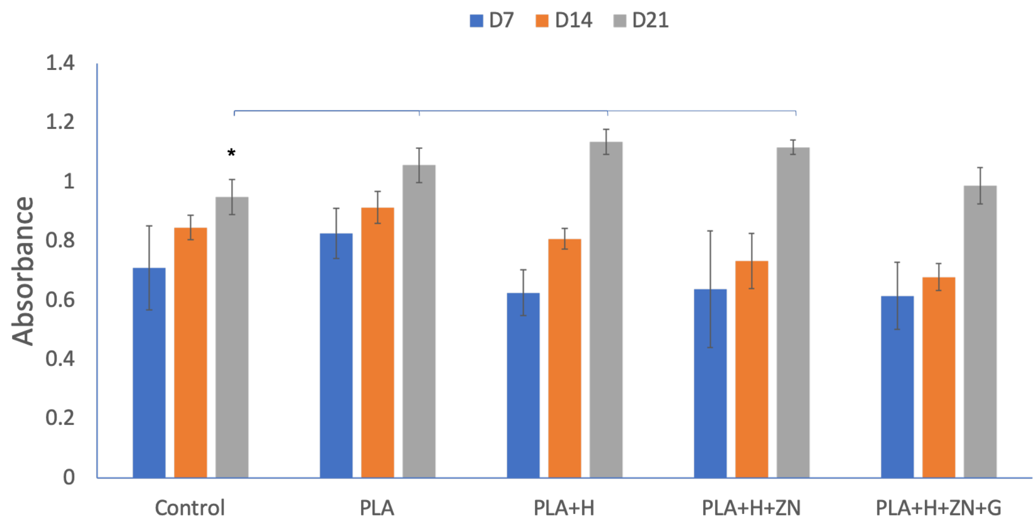

Figure 4-9: Cell proliferation ability when culture on conventional 2D surface (control) and 3D cultures that composed by PLA, PLA blended with HNTs (PLA+H), HNTs loaded with zince and blended with PLA (PLA+H+ZN) and scaffold made by PLA+H+ZN coated by gentamicin (PLA+H+ZN+G).

4.3.5 Mineralization

The potential application of this 3D printed scaffold is to regenerate bone formation. Thus, we studied the osteogenesis by assessing cell mineralization, collagen synthesis and protein secretion.

Calcium deposition is an indication of bone formation, which can be identified by Alizarin Red S staining. The Alizarin Red S-calcium complex results in the chelation between calcium and Alizarin Red S stain and presents red color under a microscope at bright field. As shown in **Figure 4-10**, there is little calcium deposition in 2D cell culture condition (control), while calcium deposition appears in 3D culture structure as early as 7 days incubation (Day 7). Calcium deposition increased with incubation time.

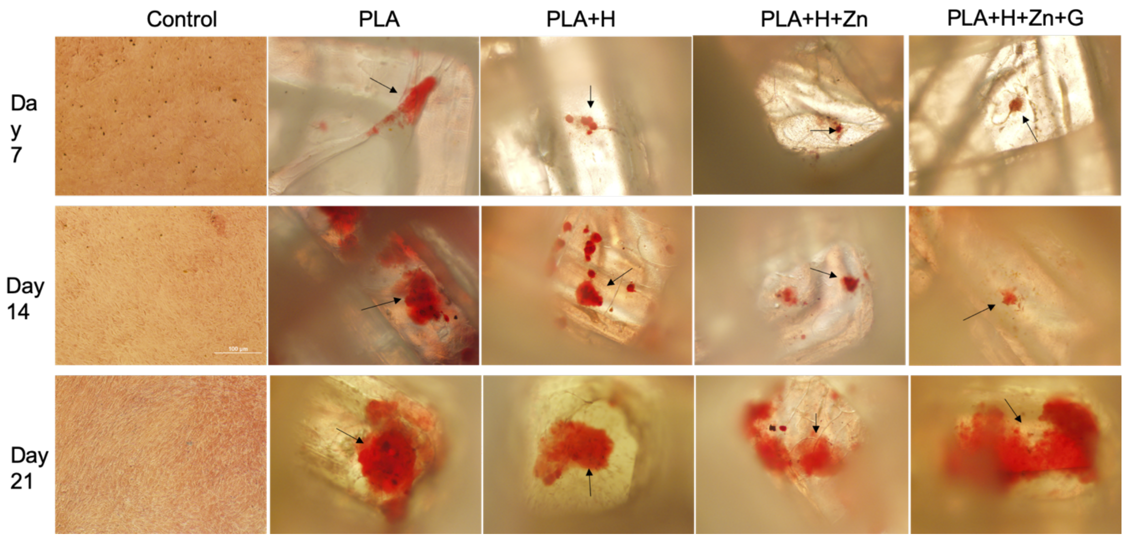

Figure 4-10: Alizarin Red S Staining of cells after 7, 14, and 21 days incubation. Each column represents cell culture with each group of scaffolds for 3 weeks. Arrows point to calcium deposition.

4.3.6 Collagen Synthesis

Even though the mechanical property enhancement is not significant with the addition of HNTs, its influence on type I collagen formation is distinct. Picro-sirius Red could stain type III collagen to be red and type I collagen to be yellow. Type I collagen is the major component of bone tissue extra cellular matrix (ECM), which is mainly synthesized by osteoblasts. The synthesis of type I collagen is one of the markers that indicates osteogenic differentiation.

In this study, when cells were cultured in 2D condition (control), a few collagens were synthesized in 7 days, and over incubation time more collagens were formed. Based on to the appearance of colors, most collagens produced in the 2D condition are type III, and only a few of type I collagens occurs after 21 days incubation. Comparing to 2D cell culture, more collagens were formed in 3D scaffolds (**Figure 4-11**and **Figure 4-12**). In addition, the appearance of type I collagen in 3D scaffold arose in 14 days with the scaffolds that contained HNTs. At that time, type I collagen only appears at the bottom layer of the scaffold (**Figure 4-12**), after one more week incubation (Day 21), type I collagen also formed at the inner space (**Figure 4-11**).

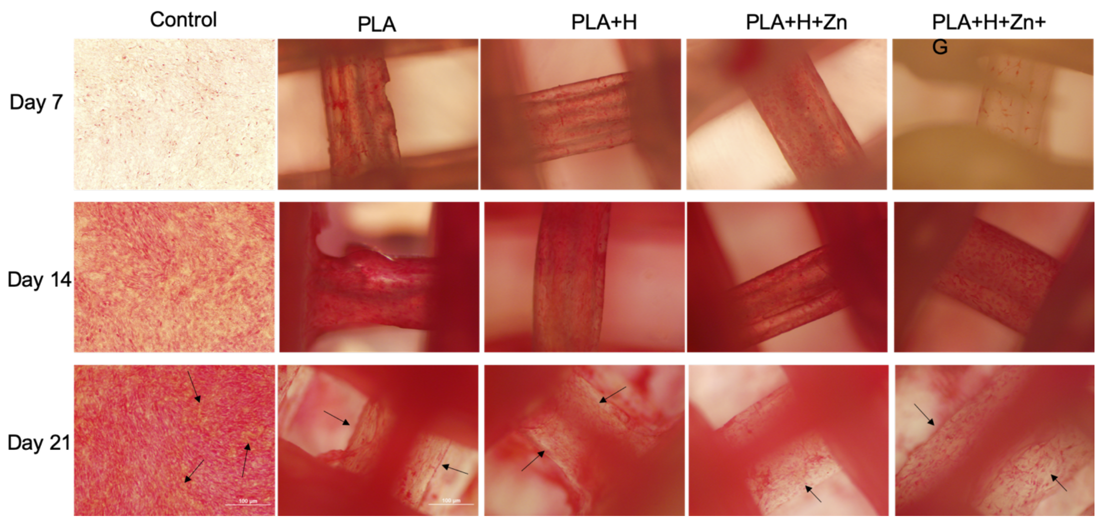

Figure 4-11: Picro-sirius Red Stain for inter space of 3D scaffolds. Arrows point to type I collagen.

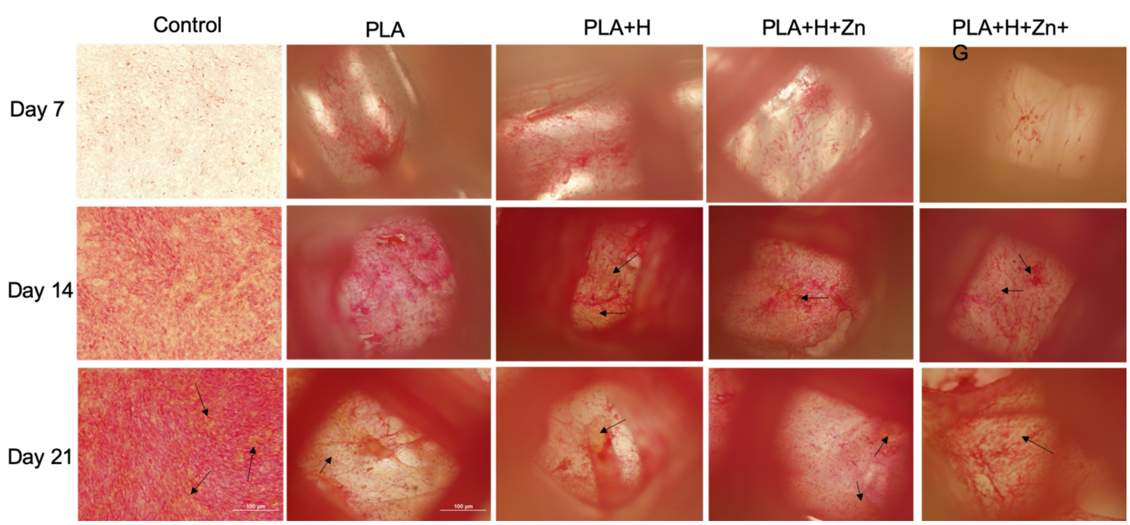

Figure 4-12: Picro-sirius Red Stain for bottom layer of 3D scaffolds. Arrows point to type I collagen.

4.3.7 Osteocalcin

Osteocalcin is another protein that is widely found in bone tissue and that can be secreted only by osteoblasts. Therefore, it is another indication for osteogenic differentiation. Since the mineralization and type I collagen widely happened after 14 days incubation, we quantified the osteocalcin at day 14 (D14) and day 21 (D21). **Figure 4-13** shows no significant difference among all groups at day 14. After one more week incubation, the increment of osteocalcin secretion of 3D scaffold with PLA+H, PLA+H+Zn is relatively higher than in 2D culture (control). In addition, cells grown on scaffold PLA+H+Zn+G secreted much more osteocalcin than any other groups.

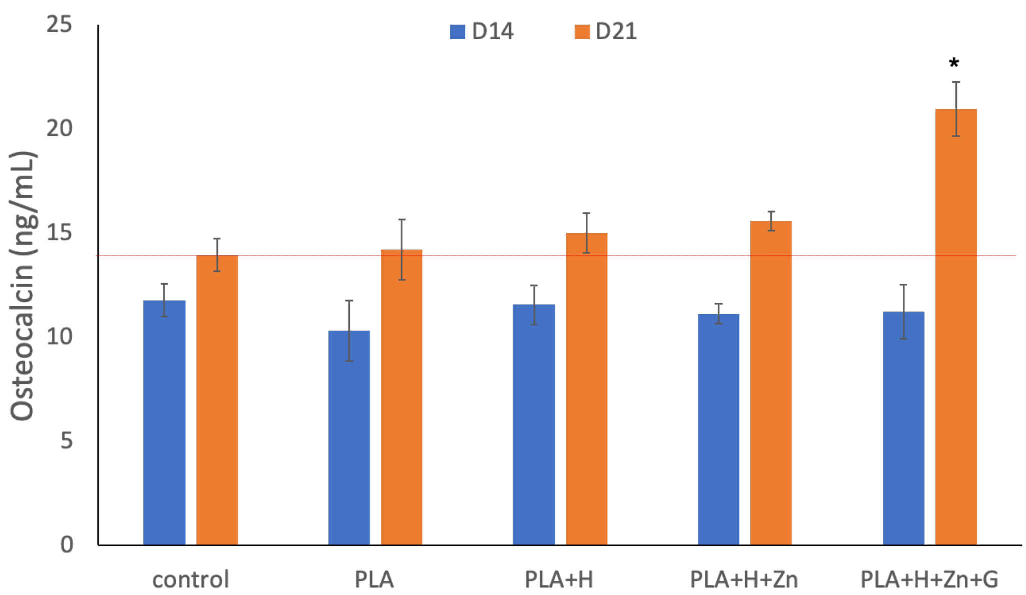

Figure 4-13: Osteocalcin concentration secreted by cell after 14 days (D14) and 21 days (D21) incubation. (error bar with standard deviation, n=3, $p<0.05$).

4.3.8 Antibacterial Efficiency

In order to reduce the risk of contamination in clinic application, we coated the 3D scaffold with gentamicin and co-cultured with *S. aureus* for 12 hours. Bacterial growth was measured by microplate reader at 630nm (**Figure 4-14**). In our hypothesis, zinc-included 3D scaffold may also exhibit antibacterial ability. However, maybe due to the deep submergence of zinc, the group of PLA+H+Zn did not inhibit bacterial growth. In contrast, the gentamicin-coated 3D scaffold prevented bacterial growth, as expected.

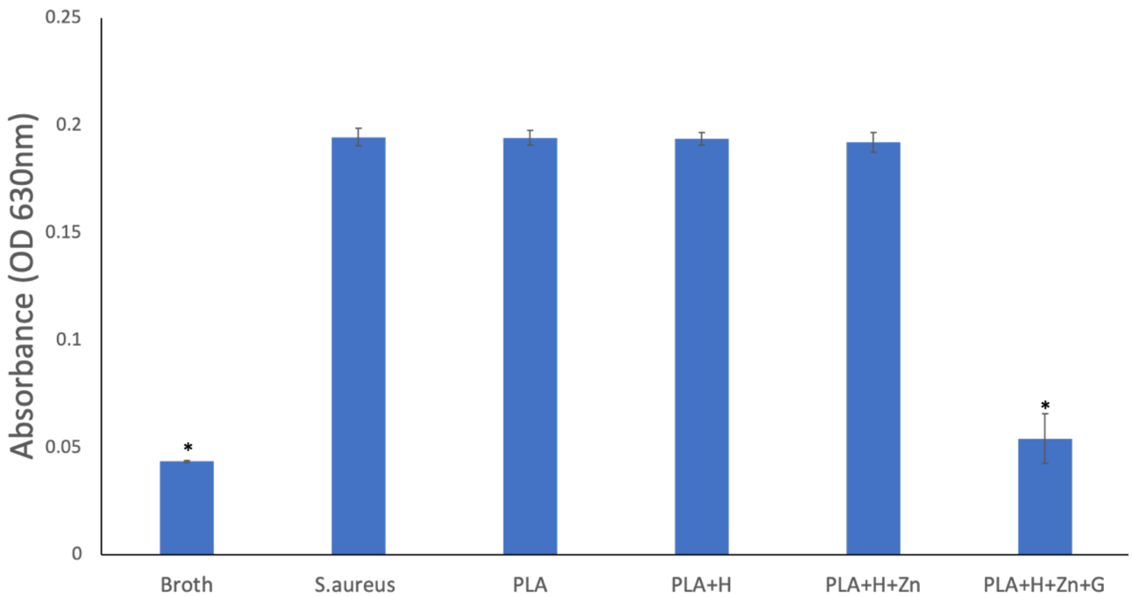

Figure 4-14: Bacterial growth inhibition efficiency. Broth without any sample and bacterial set as negative control (Broth). *S.aureus* culture in broth set as positive control (*S.aureus*). Same amount of *S.aureus* suspension was co-cultured with scaffold composed by PLA, HNTs included PLA (PLA+H), Zn loaded PLA (PLA+H+Zn), and gentamicin coated PLA (PLA+H+Zn+G). (error bar with standard deviation, n=3, $p<0.05$).

4.4 Conclusion and Discussion

In summary, surface modification of FBS+NaOH+FBS successfully improved PLA hydrophilicity and provided a friendly and attractive surface for cell growth. In this study, we aim to stimulate pre-osteoblasts to differentiate to osteoblast in 3D environment by utilizing the osteogenesis properties of HNTs. Osteogenic cell culture medium was excluded in this study due to its strong stimulation in osteogenic differentiation. After 3 weeks incubation, early bone formation was detected. Calcium deposition and type I collagen formation initiated from the bottom layer of 3D scaffold and gradually happened in the inner space. This phenomenon is consistent with another work of Jones et. al [164].

In our hypothesis, the addition of HNTs could improve PLA mechanical properties and stimulate cell differentiation. However, mechanical property enhancement is not significant, in contrast, HNTs exhibited osteogenesis by promoting type I collagen formation in a short incubation time and stimulating the osteocalcin secretion.

Even though the coating of gentamicin affected cell growth in early stage, cells recovered from its affection and exhibited a strong osteogenesis in the third week. Furthermore, after 3 weeks storage, it still efficiently restricted bacterial growth.

In conclusion, 3D scaffold made by PAL+H+Zn+G composed dual effect in stimulating bone formation and preventing bacterial contamination. This bi-functionalized scaffold has a great potential application in clinical bone defect treatment.

CHAPTER 5

CONCLUSION AND FUTURE WORK

5.1 Conclusions

All three projects have been conducted to explore the application of halloysite nanotubes in medical devices for bone disease remediation and bone regeneration.

The reinforcement properties of halloysite nanotubes for polymer material have been demonstrated in Chapter 2. As early as 1980's, chitosan has been used as pharmaceutical material [172]. The unique properties of chitosan, including its biocompatibility, biodegradation, gelation characteristics, and relative antimicrobial ability, have enabled its applications in pharmaceutical products, such as wound dressing [173] and controlled drug release [174,175]. However, it is difficult to control the mechanical properties of chitosan-derived hydrogels, which limits its application in tissue engineering. In this study, the addition of HNTs provided strong material support to chitosan hydrogel. Chitosan hydrogel film surface toughness, tensile strength, and outer and inner morphology were enhanced as well. In the study described in Chapter 2, we explored different combination ratios of chitosan and HNTs and found 2% w/w of HNTs provided the highest tensile strength. Because excessive addition of HNTs results in interfacial gaps, this weakens the composites' toleration for force loading and limits how much HNTs can be added.

Halloysite nanotubes application in drug delivery has been reported in many studies [4,51,176]. HNTs can significantly extend drug release time. When they are encapsulated by polymers, the drug release time can be extended longer, which was shown as Chapter 2, chitosan/HNTs provides sustained drug release for over 104 hours.

Recently, development of drug delivery systems based on halloysite nanotubes has archived major advance through surface modification in order to increase drug loading efficiency [5,177] and target drug delivery to cancer tumors [115,133]. In Chapter 3, HNTs were modified by DAS and conjugated with folic acid and fluorescein isothiocyanate. The final product of FA/FITC-HNTs had a 34.74% drug loading efficiency of methotrexate, which is much higher than normal treatment with a 10-20% drug loading efficiency [133,178]. In addition, our biofunctionalized HNTs successfully target cancer cells without harm to normal cell.

Even though, the addition of HNTs did not show a significant improvement in the mechanical property to 3D printed PLA scaffold as discussed in Chapter 4, HNTs showed an osteogenesis potential. In the presence of HNTs, pre-osteoblasts synthesized an early formation of type I collagen matrix and osteocalcin secretion. Gentamicin coating also did not significantly inhibit cell growth. Gentamicin-coated scaffold showed an increased and comparable cell proliferation ability with control groups by day 21. Unexpectedly, pre-osteoblast exhibited a strong osteogenic response in the presence of gentamicin. Therefore, gentamicin-coated PLA/HNTs scaffold could not only prevent bacterial contamination but also promote bone regeneration.

5.2 Future Work

After we have confirmed the proper combination ratio of chitosan and HNTs, there are much room to explore its application in biomedical engineering. Chitosan/HNTs hydrogels can be produced in different structures, such as microspheres and films, or cast into designed molds. In addition, instead of antibodies, halloysite nanotubes can be loaded with other biological factors, such as transforming growth factor β1 (TGF-β1), bone morphogenic protein 2 (BMP-2), activin-A, epidermal growth factor (EGF), and hepatocyte growth factor (HGF) to exploring its potential in tissue engineering.

HNTs modified with DAS-FA/FITC have a high drug loading efficiency of methotrexate, this may due to the similar chemical structure of folic acid and methotrexate. The drug loading efficiency for other anticancer drugs remains to be assessed. Their influence on healthy tissues and anticancer ability *in vivo* study is also waiting to be discovered.

Many obstacles remain to be overcome in the application of metal-loaded HNTs in 3D printing. In the study of Chapter 4, halloysite loaded with zinc, which is known as osteoconductive agent, was studied. However, this property did not appear in our study. This may be due to the deep encapsulation of zinc as it was loaded into HNTs and coated by PLA. Future studies should focus on how to improve the release of metal particles from a 3D printed scaffold.

BIBLIOGRAPHY

1. Liu M, Jia Z, Jia D, Zhou C. Recent advance in research on halloysite nanotubes-polymer nanocomposite. *Prog Polym Sci*. 2014;1498-1525. doi:10.1016/j.progpolymsci.2014.04.004

2. Joussein E, Petit S, Churchman J, Theng B, Righi D, Delvaux B. Halloysite clay minerals — a review. *Clay Miner*. 2005;40:383-426. doi:10.1180/0009855054040180

3. Garcia-Garcia D, Ferri JM, Ripoll L, Hidalgo M, Lopez-Martinez J, Balart R. Characterization of selectively etched halloysite nanotubes by acid treatment. *Appl Surf Sci*. 2017;422:616-625. doi:10.1016/j.apsusc.2017.06.104

4. Patel S, Jammalamadaka U, Sun L, Tappa K, Mills D. Sustained Release of Antibacterial Agents from Doped Halloysite Nanotubes. *Bioengineering*. 2015;3(1):1-14. doi:10.3390/bioengineering3010001

5. Abdullayev E, Lvov Y. Halloysite clay nanotubes for controlled release of protective agents. *J Nanosci Nanotechnol*. 2011;11(11):10007-10026. doi:10.1166/jnn.2011.5724

6. Liu M, Chang Y, Yang J, et al. Functionalized halloysite nanotube by chitosan grafting for drug delivery of curcumin to achieve enhanced anticancer efficacy. *J Mater Chem B*. 2016;b4:2253-2263. doi:10.1039/c5tb02725j

7. Shi YF, Tian Z, Zhang Y, Shen HB, Jia NQ. Functionalized halloysite nanotube-based carrier for intracellular delivery of antisense oligonucleotides. *Nanoscale Res Lett*. 2011;6(1):608. doi:10.1186/1556-276X-6-608

8. Kamble R, Ghag M, Gaikawad S, Panda B. Halloysite Nanotubes and Applications: A Review. *J Adv Sci Res*. 2012;3:25-29.

9. Boyer CJ, Ambrose J, Das S, et al. Antibacterial and antibiofouling clay nanotube - silicone composite. *Med Devices Evid Res*. 2018;11:123-137. doi:10.2147/MDER.S146248

10. Wei W, Abdullayev E, Hollister A, Mills D, Lvov YM. Clay nanotube/poly(methyl methacrylate) bone cement composites with sustained

antibiotic release. *Macromol Mater Eng*. 2012;297(7):645-653. doi:10.1002/mame.201100309

11. Sun L, Boyer C, Grimes R, Mills DK. Drug Coated Clay Nanoparticles for Delivery of Chemotherapeutics. *Curr Nanosci*. 2015;12(2):207-214. doi:10.2174/1573413711666151008014051

12. Liu M, Guo B, Du M, Cai X, Jia D. Properties of halloysite nanotube-epoxy resin hybrids and the interfacial reactions in the systems. *Nanotechnology*. 2007;18(45):455703. doi:10.1088/0957-4484/18/45/455703

13. Guo M, Wang A, Muhammad F, et al. Halloysite nanotubes, a multifunctional nanovehicle for anticancer drug delivery. *Chinese J Chem*. 2012;30:2115-2120. doi:10.1002/cjoc.201200657

14. Yah WO, Takahara A, Lvov YM. Selective modification of halloysite lumen with octadecylphosphonic acid: New inorganic tubular micelle. *J Am Chem Soc*. 2012;134:1853-1859. doi:10.1021/ja210258y

15. Naumenko EA, Guryanov ID, Yendluri R, Lvov YM, Fakhrullin RF. Clay nanotube-biopolymer composite scaffolds for tissue engineering. *Nanoscale*. 2016;8(13):7257-7271. doi:10.1039/c6nr00641h

16. Bhowmik D, Bhanot R, Gautam D, Rai P, Kumar KPS. Osteomyelitis-Symptoms, Causes and Treatment. *Res J Sci Technol*. 2018;10(2):165. doi:10.5958/2349-2988.2018.00024.4

17. Múñez Rubio E, Pintos Pascual I, Ramos Martínez A. Osteomyelitis. *Med*. 2018;12(55):3262-3271. doi:10.1016/j.med.2018.04.013

18. Picci P. Osteosarcoma (Osteogenic sarcoma). *Orphanet J Rare Dis*. 2007;1:6. doi:10.1186/1750-1172-2-6

19. Finkel MP, Reilly CA Jr B. *Pathogenesis of Radiation and Virus-Induced Bone Tumors, Recent Results Cancer Res*.; 1976.

20. Huvos AG. *Bone Tumors : Diagnosis, Treatment, and Prognosis*. W.B. Saunders Co; 1981. https://inis.iaea.org/search/search.aspx?orig_q=RN:18094791.

21. McIntyre JF, Smith-Sorensen B, Friend SH, et al. Germline mutations of the p53 tumor suppressor gene in children with osteosarcoma. *J Clin Oncol*. 1994;12(5):925-930. doi:10.1200/JCO.1994.12.5.925

22. (US) O of the SG. *Bone Health and Osteoporosis*. Office of the Surgeon General (US); 2004. http://www.ncbi.nlm.nih.gov/pubmed/20945569.

23. Kumar V, Abbas AK, Fausto N, Mitchell R. Robbins Basic Pathology ((8th ed.) ed.). *Saunders Elsevier*. 2007:810-811.

24. Grimer RJ, Taminiau AM, Cannon SR. Surgical outcomes in osteosarcoma. *J Bone Jt Surg*. 2003;84(3):395-400. doi:10.1302/0301-620x.84b3.12019

25. McHorney CA, Schousboe JT, Cline RR, Weiss TW. The impact of osteoporosis medication beliefs and side-effect experiences on non-adherence to oral bisphosphonates. In: *Current Medical Research and Opinion*. ; 2007:3137-3152. doi:10.1185/030079907X242890

26. Dimitriou R, Jones E, McGonagle D, Giannoudis P V. Bone regeneration: Current concepts and future directions. *BMC Med*. 2011:66. doi:10.1186/1741-7015-9-66

27. Campana V, Milano G, Pagano E, et al. Bone substitutes in orthopaedic surgery: from basic science to clinical practice. *J Mater Sci Mater Med*. 2014;25:2445-2461. doi:10.1007/s10856-014-5240-2

28. Bauer TW, Muschler GF. Bone graft materials. An overview of the basic science. *Clin Orthop Relat Res*. 2000;371:10-27.

29. Sanchez CJ, Ward CL, Romano DR, et al. Staphylococcus aureus biofilms decrease osteoblast viability, inhibits osteogenic differentiation, and increases bone resorption in vitro. *BMC Musculoskelet Disord*. 2013;14:187. doi:10.1186/1471-2474-14-187

30. De Long WG, Einhorn TA, Koval K, et al. Bone grafts and bone graft substitutes in orthopaedic trauma surgery: A critical analysis. *J Bone Jt Surg - Ser A*. 2007:649-658. doi:10.2106/00004623-200703000-00026

31. Hatzenbuehler J, Pulling TJ. Diagnosis and Management of Osteomyelitis - American Family Physician. *Am Fam Physician*. 2011;84(9):1027-1033. doi:10.2165/00019053-199916060-00003

32. Burge R, Dawson-Hughes B, Solomon DH, Wong JB, King A, Tosteson A. Incidence and economic burden of osteoporosis-related fractures in the United States, 2005-2025. *J Bone Miner Res*. 2007;22:465-475. doi:10.1359/jbmr.061113

33. Poveda Roda R, Bagan JV, Sanchis Bielsa JM, Carbonell Pastor E. Antibiotic use in dental practice. A review. *Med Oral Patol Oral Cir Bucal*. 2007:186-192.

34. Chen M, Yu Q, Sun H. Novel strategies for the prevention and treatment of biofilm related infections. *Int J Mol Sci*. 2013:18488-18501. doi:10.3390/ijms140918488

35. Allahverdiyev AM, Kon KV, Abamor ES, Bagirova M, Rafailovich M. Coping

with antibiotic resistance: Combining nanoparticles with antibiotics and other antimicrobial agents. *Expert Rev Anti Infect Ther*. 2011:1035-1052. doi:10.1586/eri.11.121

36. Rinaudo M. Chitin and chitosan: Properties and applications. *Prog Polym Sci*. 2006:603-632. doi:10.1016/j.progpolymsci.2006.06.001

37. Muzzarelli RAA. Human enzymatic activities related to the therapeutic administration of chitin derivatives. *Cell Mol Life Sci*. 1997:131-140. doi:10.1007/PL00000584

38. Prabaharan M, Mano JF. Chitosan-based particles as controlled drug delivery systems. *Drug Deliv J Deliv Target Ther Agents*. 2005:41-57. doi:10.1080/10717540590889781

39. Divya K, Vijayan S, George TK, Jisha MS. Antimicrobial properties of chitosan nanoparticles: Mode of action and factors affecting activity. *Fibers Polym*. 2017;18:221. doi:10.1007/s12221-017-6690-1

40. Dash M, Chiellini F, Ottenbrite RM, Chiellini E. Chitosan - A versatile semi-synthetic polymer in biomedical applications. *Prog Polym Sci*. 2011:981-1014. doi:10.1016/j.progpolymsci.2011.02.001

41. Kashyap M, Archana D, Semwal A, et al. Chitosan: A Promising Substrate for Regenerative Medicine in Drug Formulation Abbreviations PEC Polyelectrolyte complex PVA Poly(vinyl alcohol) AgNPs Silver nanoparticles NPs Nanoparticles MCNs Magnetic-Chitosan Nanogels. In: *Chitin and Chitosan for Regenerative Medicine*. ; 2016;261-277. doi:10.1007/978-81-322-2511-9_10

42. Di Martino A, Sittinger M, Risbud M V. Chitosan: A versatile biopolymer for orthopaedic tissue-engineering. *Biomaterials*. 2005;5983-5990. doi:10.1016/j.biomaterials.2005.03.016

43. Wu T, Li Y, Lee DS. Chitosan-based composite hydrogels for biomedical applications. *Macromol Res*. 2017:480-488. doi:10.1007/s13233-017-5066-0

44. Yao, Kangde; Li, Junjie; Yao, Fnglian; Jin Y. *CHITOSAN-BASED HYDROGELS : Functions and Applications.* CRC Press; 2017.

45. Wang SF, Shen L, Zhang W De, Tong YJ. Preparation and mechanical properties of chitosan/carbon nanotubes composites. *Biomacromolecules*. 2005;6:3067-3072. doi:10.1021/bm050378v

46. Chatterjee S, Lee MW, Woo SH. Enhanced mechanical strength of chitosan hydrogel beads by impregnation with carbon nanotubes. *Carbon N Y*. 2009:2933-2936. doi:10.1016/j.carbon.2009.06.043

47. Hong SI, Lee JH, Bae HJ, et al. Effect of shear rate on structural, mechanical, and barrier properties of chitosan/montmorillonite nanocomposite film. *J Appl Polym Sci*. 2011;119(5):2742-2749. doi:10.1002/app.31767

48. Park H, Guo X, Temenoff J, Kasper F, Mikos A. Effect of Swelling Ratio of Intectable Hydrogel Composites on Chondrongenix Differentiation of Encapsculated Rabbit Marrow Mesenchymal Stem Cells In Vitro (Author Manuscript). *Biomacromolecules*. 2010;10(3):541-546. doi:10.1021/bm801197m.Effect

49. Liu M, Zhang Y, Wu C, Xiong S, Zhou C. Chitosan/halloysite nanotubes bionanocomposites: Structure, mechanical properties and biocompatibility. *Int J Biol Macromol*. 2012;51:566-575. doi:10.1016/j.ijbiomac.2012.06.022

50. Chen Y, Murphy A, Scholz D, Geever LM, Lyons JG, Devine DM. Surface-modified halloysite nanotubes reinforced poly(lactic acid) for use in biodegradable coronary stents. *J Appl Polym Sci*. 2018;135:46521. doi:10.1002/app.46521

51. Karnik S, Hines K, Mills DK. Nanoenhanced hydrogel system with sustained release capabilities. *J Biomed Mater Res - Part A*. 2015;103A:2416-2426. doi:10.1002/jbm.a.35376

52. Bordeepong S, Bhongsuwan D, Pungrassami T, Bhongsuwan T. Characterization of halloysite from thung yai district, Nakhon Si Thammarat Province, in Southern Thailand. *Songklanakarin J Sci Technol*. 2011;33(5):599-607.

53. Ahmed FR, Shoaib MH, Azhar M, et al. In-vitro assessment of cytotoxicity of halloysite nanotubes against HepG2, HCT116 and human peripheral blood lymphocytes. *Colloids Surfaces B Biointerfaces*. 2015;135:50-55. doi:10.1016/j.colsurfb.2015.07.021

54. Fakhrullina GI, Akhatova FS, Lvov YM, Fakhrullin RF. Toxicity of halloysite clay nanotubes in vivo: A Caenorhabditis elegans study. *Environ Sci Nano*. 2015;2:54-59. doi:10.1039/c4en00135d

55. Lai X, Agarwal M, Lvov YM, Pachpande C, Varahramyan K, Witzmann FA. Proteomic profiling of halloysite clay nanotube exposure in intestinal cell co-culture. *J Appl Toxicol*. 2013:1316-1329. doi:10.1002/jat.2858

56. Albdiry MT, Yousif BF. Role of silanized halloysite nanotubes on structural, mechanical properties and fracture toughness of thermoset nanocomposites. *Mater Des*. 2014;57:279-288. doi:10.1016/j.matdes.2013.12.017

57. Deen I, Pang X, Zhitomirsky I. Electrophoretic deposition of composite chitosan-halloysite nanotube-hydroxyapatite films. *Colloids Surfaces A Physicochem Eng Asp*. 2012;410:38-44. doi:10.1016/j.colsurfa.2012.06.011

58. GarcÁ FJG, Rodríguez SG, Kalytta A, Reller A. Study of natural halloysite from the Dragon Mine, Utah (USA). *Zeitschrift fur Anorg und Allg Chemie*. 2009;635:790-795. doi:10.1002/zaac.200900076

59. Karthik, Tappa; Udayabhanu, Jammalamadaka; David KM. Formulation and Evaluation of Nanoenhanced Anti-bacterial Calcium Phosphate Bone Cements. *Orthop Biomater*. 2017:85-108. doi:10.1007/978-3-319-73664-8

60. Rooj S, Das A, Thakur V, Mahaling RN, Bhowmick AK, Heinrich G. Preparation and properties of natural nanocomposites based on natural rubber and naturally occurring halloysite nanotubes. *Mater Des*. 2010;31(4):2151-2156. doi:10.1016/j.matdes.2009.11.009

61. Lvov Y, Wang W, Zhang L, Fakhrullin R. Halloysite Clay Nanotubes for Loading and Sustained Release of Functional Compounds. *Adv Mater*. 2016;28:1227-1250. doi:10.1002/adma.201502341

62. Shukla SK, Mishra AK, Arotiba OA, Mamba BB. Chitosan-based nanomaterials: A state-of-the-art review. *Int J Biol Macromol*. 2013:46-58. doi:10.1016/j.ijbiomac.2013.04.043

63. Pishbin F, Mouriño V, Gilchrist JB, et al. Single-step electrochemical deposition of antimicrobial orthopaedic coatings based on a bioactive glass/chitosan/nano-silver composite system. *Acta Biomater*. 2013;9:7469-7479. doi:10.1016/j.actbio.2013.03.006

64. Wang Y, Deen I, Zhitomirsky I. Electrophoretic deposition of polyacrylic acid and composite films containing nanotubes and oxide particles. *J Colloid Interface Sci*. 2011;362:367-374. doi:10.1016/j.jcis.2011.07.007

65. De Silva RT, Pasbakhsh P, Goh KL, Chai SP, Ismail H. Physico-chemical characterisation of chitosan/halloysite composite membranes. *Polym Test*. 2013;32:265-271. doi:10.1016/j.polymertesting.2012.11.006

66. Liu M, Wu C, Jiao Y, Xiong S, Zhou C. Chitosan-halloysite nanotubes nanocomposite scaffolds for tissue engineering. *J Mater Chem B*. 2013;1(15):2078-2089. doi:10.1039/c3tb20084a

67. Massaro M, Colletti CG, Lazzara G, Riela S. The use of some clay minerals as natural resources for drug carrier applications. *J Funct Biomater*. 2018;9:58. doi:10.3390/jfb9040058

68. Aguzzi C, Cerezo P, Viseras C, Caramella C. Use of clays as drug delivery systems: Possibilities and limitations. *Appl Clay Sci*. 2007;36:22-36. doi:10.1016/j.clay.2006.06.015

69. M.E. A, A. L-G, M. S, M.M. E-R, C.V. I. Kaolinite in pharmaceutics and biomedicine. *Int J Pharm*. 2017;533(1):34-48. doi:10.1016/j.ijpharm.2017.09.056

70. Zhang Y, Long M, Huang P, et al. Emerging integrated nanoclay-facilitated drug delivery system for papillary thyroid cancer therapy. *Sci Rep*. 2016. doi:10.1038/srep33335

71. Holešová S, Hundáková M, Pazdziora E. Antibacterial Kaolinite Based Nanocomposites. *Procedia Mater Sci*. 2016;12:124-129. doi:10.1016/j.mspro.2016.03.022

72. Zhang Y, Long M, Huang P, et al. Intercalated 2D nanoclay for emerging drug delivery in cancer therapy. *Nano Res*. 2017;10(8):2633-2643. doi:10.1007/s12274-017-1466-x

73. Kim MH, Choi G, Elzatahry A, Vinu A, Choy Y Bin, Choy JH. Review of clay-drug hybrid materials for biomedical applications: Administration routes. *Clays Clay Miner*. 2016;64:115-130. doi:10.1346/CCMN.2016.0640204

74. Jayrajsinh S, Shankar G, Agrawal YK, Bakre L. Montmorillonite nanoclay as a multifaceted drug-delivery carrier: A review. *J Drug Deliv Sci Technol*. 2017:200-209. doi:10.1016/j.jddst.2017.03.023

75. Aguzzi C, Sandri G, Bonferoni C, et al. Solid state characterisation of silver sulfadiazine loaded on montmorillonite/chitosan nanocomposite for wound healing. *Colloids Surfaces B Biointerfaces*. 2014;113:152-157. doi:10.1016/j.colsurfb.2013.08.043

76. Sharma A, Puri V, Kakkar V, Singh I. Formulation and evaluation of silymarin-loaded chitosan-montmorilloite microbeads for the potential treatment of gastric ulcers. *J Funct Biomater*. 2018;9(3):52. doi:10.3390/jfb9030052

77. Bothiraja C, Thorat UH, Pawar AP, Shaikh KS. Chitosan coated layered clay montmorillonite nanocomposites modulate oral delivery of paclitaxel in colonic cancer. *Mater Technol*. 2014;29:B120-B126. doi:10.1179/1753555714y.0000000174

78. Thakur G, Singh A, Singh I. Chitosan-montmorillonite polymer composites: Formulation and evaluation of sustained release tablets of aceclofenac. *Sci Pharm*. 2015;84:603-617. doi:10.3390/scipharm84040603

79. Salcedo I, Aguzzi C, Sandri G, et al. In vitro biocompatibility and mucoadhesion of montmorillonite chitosan nanocomposite: A new drug delivery. *Appl Clay Sci*. 2012;55:131-137. doi:10.1016/j.clay.2011.11.006

80. Shchukin DG, Sukhorukov GB, Price RR, Lvov YM. Halloysite nanotubes as

biomimetic nanoreactors. *Small*. 2005;1:510-513. doi:10.1002/smll.200400120

81. Vergaro V, Abdullayev E, Lvov YM, et al. Cytocompatibility and uptake of halloysite clay nanotubes. *Biomacromolecules*. 2010;11:820-826. doi:10.1021/bm9014446

82. Wei W, Minullina R, Abdullayev E, Fakhrullin R, Mills D, Lvov Y. Enhanced efficiency of antiseptics with sustained release from clay nanotubes. *RSC Adv*. 2014;4:488-494. doi:10.1039/c3ra45011b

83. Du M, Guo B, Jia D. Newly emerging applications of halloysite nanotubes: A review. *Polym Int*. 2010;59(5):574-582. doi:10.1002/pi.2754

84. Lvov YM, Shchukin DG, Möhwald H, Price RR. Halloysite clay nanotubes for controlled release of protective agents. *ACS Nano*. 2008;2:814-820. doi:10.1021/nn800259q

85. Abdullayev E, Price R, Shchukin D, Lvov Y. Halloysite tubes as nanocontainers for anticorrosion coating with benzotriazole. *ACS Appl Mater Interfaces*. 2009;1:437-443. doi:10.1021/am9002028

86. Srinatha A, Pandit J, Singh S. Ionic cross-linked chitosan beads for extended release of ciprofloxacin: In vitro characterization. *Indian J Pharm Sci*. 2008;70:16-21. doi:10.4103/0250-474x.40326

87. Berger J, Reist M, Mayer JM, Felt O, Peppas NA, Gurny R. Structure and interactions in covalently and ionically crosslinked chitosan hydrogels for biomedical applications. *Eur J Pharm Biopharm*. 2004:19-34. doi:10.1016/S0939-6411(03)00161-9

88. Huang B, Liu M, Zhou C. Chitosan composite hydrogels reinforced with natural clay nanotubes. *Carbohydr Polym*. 2017;175:689-698. doi:10.1016/j.carbpol.2017.08.039

89. Chiu YC, Kocagöz S, Larson JC, Brey EM. Evaluation of Physical and Mechanical Properties of Porous Poly (Ethylene Glycol)-co-(L-Lactic Acid) Hydrogels during Degradation. *PLoS One*. 2013;8(4):e60728. doi:10.1371/journal.pone.0060728

90. Fisher JP, Timmer MD, Holland TA, Dean D, Engel PS, Mikos AG. Photoinitiated cross-linking of the biodegradable polyester poly(propylene fumarate). Part I. Determination of network structure. *Biomacromolecules*. 2003;4:1335-1342. doi:10.1021/bm030028d

91. Sokic S, Papavasiliou G. Controlled Proteolytic Cleavage Site Presentation in Biomimetic PEGDA Hydrogels Enhances Neovascularization In Vitro. *Tissue Eng*

Part A. 2012;18:2477-2486. doi:10.1089/ten.tea.2012.0173

92. Howlader N, Noone AM, Krapcho M, Neyman N, Aminou R, Waldron W, Altekruse SF, Kosary CL, Ruhl J, Tatalovich Z, Cho H, Mariotto A, Eisner MP, Lewis DR, Chen HS, Feuer EJ, Cronin KA EB (Eds). SEER Cancer Statistics Review 1975-2008 National Cancer Institute SEER Cancer Statistics Review 1975-2008 National Cancer Institute. *Cancer*. 2011.

93. Seigel R, Jemal A. American Cancer Society: Cancer Facts and Figures. 2015. doi:10.3322/caac.21254

94. Caraglia M, De Rosa G, Abbruzzese A, Leonetti C. Nanotechnologies: New Opportunities for Old Drugs. The Case of Aminobisphosphonates. *J Nanomedine Biotherapeutic Discov*. 2011;1:103e. doi:10.4172/2155-983x.1000103e

95. Luk BT, Zhang L. Current advances in polymer-based nanotheranostics for cancer treatment and diagnosis. *ACS Appl Mater Interfaces*. 2014;6:21859-21873. doi:10.1021/am5036225

96. Ma L, Kohli M, Smith A. Nanoparticles for combination drug therapy. *ACS Nano*. 2013:9518-9525. doi:10.1021/nn405674m

97. Chen L, Malhotra A. Combination Approach: the Future of the War Against Cancer. *Cell Biochem Biophys*. 2015;72(3):637-641. doi:10.1007/s12013-015-0549-0

98. Markman JL, Rekechenetskiy A, Holler E, Ljubimova JY. Nanomedicine therapeutic approaches to overcome cancer drug resistance. *Adv Drug Deliv Rev*. 2013:65,1866-1879. doi:10.1016/j.addr.2013.09.019

99. Yang X, Du H, Liu J, Zhai G. Advanced nanocarriers based on heparin and its derivatives for cancer management. *Biomacromolecules*. 2015;16:423-436. doi:10.1021/bm501532e

100. Wang X, Li J, Wang Y, et al. A folate receptor-targeting nanoparticle minimizes drug resistance in a human cancer model. *ACS Nano*. 2011;5(8):6184-6194. doi:10.1021/nn200739q

101. Allen TM, Cullis PR. Drug Delivery Systems: Entering the Mainstream. *Science (80-)*. 2004;303:1818-1822. doi:10.1126/science.1095833

102. Abdullayev E, Lvov Y. Halloysite clay nanotubes as a ceramic “skeleton” for functional biopolymer composites with sustained drug release. *J Mater Chem B*. 2013;1:2894-2903. doi:10.1039/c3tb20059k

103. Qi R, Guo R, Shen M, et al. Electrospun poly(lactic-co-glycolic acid)/halloysite

nanotube composite nanofibers for drug encapsulation and sustained release. *J Mater Chem*. 2010;20(47):10622-10629. doi:10.1039/c0jm01328e

104. Abdullayev E, Lvov Y. Halloysite for Controllable Loading and Release. In: *Developments in Clay Science*. ; 2016:554-605. doi:10.1016/B978-0-08-100293-3.00022-4

105. Paola M Di, Quarta A, Pisani P, et al. Surface coating highly improves cytocompatibility of halloysite nanotubes: A metabolic and ultrastructural study. *IEEE Trans Nanotechnol*. 2016;15(5):770-774. doi:10.1109/TNANO.2016.2546955

106. Fakhrullina G, Khakimova E, Akhatova F, Lazzara G, Parisi F, Fakhrullin R. Selective Antimicrobial Effects of Curcumin@Halloysite Nanoformulation: A Caenorhabditis elegans Study. *ACS Appl Mater Interfaces*. 2019. doi:10.1021/acsami.9b07499

107. Yuan P, Tan D, Annabi-Bergaya F. Properties and applications of halloysite nanotubes: Recent research advances and future prospects. *Appl Clay Sci*. 2015;112:75-93. doi:10.1016/j.clay.2015.05.001

108. Lvov Y, Abdullayev E. Functional polymer-clay nanotube composites with sustained release of chemical agents. *Prog Polym Sci*. 2013:1690-1719. doi:10.1016/j.progpolymsci.2013.05.009

109. Tharmavaram M, Pandey G, Rawtani D. Surface modified halloysite nanotubes: A flexible interface for biological, environmental and catalytic applications. *Adv Colloid Interface Sci*. 2018:82-101. doi:10.1016/j.cis.2018.09.001

110. Yang Y, Chen Y, Leng F, Huang L, Wang Z, Tian W. Recent advances on surface modification of halloysite nanotubes for multifunctional applications. *Appl Sci*. 2017;7(12):1215. doi:10.3390/app7121215

111. Massaro M, Lazzara G, Milioto S, Noto R, Riela S. Covalently modified halloysite clay nanotubes: synthesis, properties, biological and medical applications. *J Mater Chem B*. 2017;5:2867-2882. doi:10.1039/c7tb00316a

112. Massaro M, Amorati R, Cavallaro G, et al. Direct chemical grafted curcumin on halloysite nanotubes as dual-responsive prodrug for pharmacological applications. *Colloids Surfaces B Biointerfaces*. 2016;140:505-513. doi:10.1016/j.colsurfb.2016.01.025

113. Grimes W, Luo Y, McFarland A, Mills D. Bi-Functionalized Clay Nanotubes for Anti-Cancer Therapy. *Appl Sci*. 2018;8(2):281. doi:10.3390/app8020281

114. Luo X, Peng X, Hou J, Wu S, Shen J, Wang L. Folic acid-functionalized

polyethylenimine superparamagnetic iron oxide nanoparticles as theranostic agents for magnetic resonance imaging and PD-L1 siRNA delivery for gastric cancer. *Int J Nanomedicine*. 2017;12:5331-5343. doi:10.2147/IJN.S137245

115. Hu Y, Chen J, Li X, et al. Multifunctional halloysite nanotubes for targeted delivery and controlled release of doxorubicin in-vitro and in-vivo studies. *Nanotechnology*. 2017;28(37):375101. doi:10.1088/1361-6528/aa8393

116. Ramasamy T, Ruttala HB, Gupta B, et al. Smart chemistry-based nanosized drug delivery systems for systemic applications: A comprehensive review. *J Control Release*. 2017:226-253. doi:10.1016/j.jconrel.2017.04.043

117. Leamon CP, Reddy JA. Folate-targeted chemotherapy. *Adv Drug Deliv Rev*. 2004;56(8):1127-1141. doi:10.1016/j.addr.2004.01.008

118. Lu Y, Low PS. Immunotherapy of folate receptor-expressing tumors: Review of recent advances and future prospects. In: *Journal of Controlled Release*. ; 2003:17-29. doi:10.1016/S0168-3659(03)00215-3

119. Kansara V, Paturi D, Luo S, Gaudana R, Mitra AK. Folic acid transport via high affinity carrier-mediated system in human retinoblastoma cells. *Int J Pharm*. 2008;355:210-219. doi:10.1016/j.ijpharm.2007.12.008

120. Barrientos-Ramírez S, Oca-Ramírez GM De, Ramos-Fernández E V., Sepúlveda-Escribano A, Pastor-Blas MM, González-Montiel A. Surface modification of natural halloysite clay nanotubes with aminosilanes. Application as catalyst supports in the atom transfer radical polymerization of methyl methacrylate. *Appl Catal A Gen*. 2011;406:22-23. doi:10.1016/j.apcata.2011.08.003

121. Sun P, Liu G, Lv D, Dong X, Wu J, Wang D. Effective activation of halloysite nanotubes by piranha solution for amine modification via silane coupling chemistry. *RSC Adv*. 2015;5:52916-52925. doi:10.1039/c5ra04444h

122. Cavallaro G, Lazzara G, Milioto S, Parisi F. Hydrophobically Modified Halloysite Nanotubes as Reverse Micelles for Water-in-Oil Emulsion. *Langmuir*. 2015;31:7472-7478. doi:10.1021/acs.langmuir.5b01181

123. Yoon S-A, Choi JR, Kim J-O, Shin J-Y, Zhang X, Kang J-H. Influence of Reduced Folate Carrier and Dihydrofolate Reductase Genes on Methotrexate-Induced Cytotoxicity. *Cancer Res Treat*. 2010;42:163-171. doi:10.4143/crt.2010.42.3.163

124. Costa Lima SA, Gaspar A, Reis S, Durães L. Multifunctional nanospheres for co-delivery of methotrexate and mild hyperthermia to colon cancer cells. *Mater Sci Eng C*. 2017;75:1420-1426. doi:10.1016/j.msec.2017.03.049

125. Jang J-H, Jeong S-H, Lee Y-B. Preparation and In Vitro/In Vivo Characterization

of Polymeric Nanoparticles Containing Methotrexate to Improve Lymphatic Delivery. *Int J Mol Sci*. 2019;20:3312. doi:10.3390/ijms20133312

126. Liu H, Wang ZG, Liu SL, et al. Intracellular pathway of halloysite nanotubes: potential application for antitumor drug delivery. *J Mater Sci*. 2019;54(1):693-704. doi:10.1007/s10853-018-2775-5

127. Rong R, Xu X, Zhu S, Li B, Wang X, Tang K. Facile preparation of homogeneous and length controllable halloysite nanotubes by ultrasonic scission and uniform viscosity centrifugation. *Chem Eng J*. 2016;291:20-29. doi:10.1016/j.cej.2016.01.082

128. Torchilin VP. Recent advances with liposomes as pharmaceutical carriers. *Nat Rev Drug Discov*. 2005:145. doi:10.1038/nrd1632

129. Soppimath KS, Aminabhavi TM, Kulkarni AR, Rudzinski WE. Biodegradable polymeric nanoparticles as drug delivery devices. *J Control Release*. 2001:1-20. doi:10.1016/S0168-3659(00)00339-4

130. Akbarzadeh A, Rezaei-Sadabady R, Davaran S, et al. Liposome: Classification, preparation, and applications. *Nanoscale Res Lett*. 2013;8:102. doi:10.1186/1556-276X-8-102

131. Birnbaum DT, Kosmala JD, Henthorn DB, Brannon-Peppas L. Controlled release of β-estradiol from PLAGA microparticles: The effect of organic phase solvent on encapsulation and release. *J Control Release*. 2000;65:375-387. doi:10.1016/S0168-3659(99)00219-9

132. Lvov Y, Abdullayev E. Polymer - clay nanotube composites with sustained release of bioactive agents. *Prog Polym Sci*. 2012;38:1690-1719.

133. Wu Y-P, Yang J, Gao H-Y, et al. Folate-Conjugated Halloysite Nanotubes, an Efficient Drug Carrier, Deliver Doxorubicin for Targeted Therapy of Breast Cancer. *ACS Appl Nano Mater*. 2018;1(2):595-608. doi:10.1021/acsanm.7b00087

134. Yang J, Wu Y, Shen Y, et al. Enhanced Therapeutic Efficacy of Doxorubicin for Breast Cancer Using Chitosan Oligosaccharide-Modified Halloysite Nanotubes. *ACS Appl Mater Interfaces*. 2016;8(40):26578-26590. doi:10.1021/acsami.6b09074

135. Grimes WR, Luo Y, McFarland AW, Mills DK. Bi-functionalized clay nanotubes for anti-cancer therapy. *Appl Sci*. 2018;8(2):281. doi:10.3390/app8020281

136. Chia HN, Wu BM. Recent advances in 3D printing of biomaterials. *J Biol Eng*. 2015;9(1):4. doi:10.1186/s13036-015-0001-4

137. Middleton JC, Tipton AJ. Synthetic biodegradable polymers as orthopedic devices. *Biomaterials*. 2000;21:2335-2346. doi:10.1016/S0142-9612(00)00101-0

138. Karageorgiou V, Kaplan D. Porosity of 3D biomaterial scaffolds and osteogenesis. *Biomaterials*. 2005;26(27):5474-5491. doi:10.1016/j.biomaterials.2005.02.002

139. Cao H, Kuboyama N. A biodegradable porous composite scaffold of PGA/β-TCP for bone tissue engineering. *Bone*. 2010;46(2):386-395. doi:10.1016/j.bone.2009.09.031

140. Kucharska M, Butruk B, Walenko K, Brynk T, Ciach T. Fabrication of in-situ foamed chitosan/β-TCP scaffolds for bone tissue engineering application. *Mater Lett*. 2012;85:124-127. doi:10.1016/j.matlet.2012.07.002

141. Sultana N, Wang M. Fabrication of HA/PHBV composite scaffolds through the emulsion freezing/freeze-drying process and characterisation of the scaffolds. In: *Journal of Materials Science: Materials in Medicine*. ; 2008;19:2555. doi:10.1007/s10856-007-3214-3

142. Tarafder S, Balla VK, Davies NM, Bandyopadhyay A, Bose S. Microwave-sintered 3D printed tricalcium phosphate scaffolds for bone tissue engineering. *J Tissue Eng Regen Med*. 2013;7(8):631-641. doi:10.1002/term.555

143. Bose S, Vahabzadeh S, Bandyopadhyay A. Bone tissue engineering using 3D printing. *Mater Today*. 2013;16(12):496-504. doi:10.1016/j.mattod.2013.11.017

144. Clarke B. Normal bone anatomy and physiology. *Clin J Am Soc Nephrol*. 2008;3:S131-S139. doi:10.2215/CJN.04151206

145. Buck DW, Dumanian GA. Bone biology and physiology: Part I. the fundamentals. *Plast Reconstr Surg*. 2012:1314-1320. doi:10.1097/PRS.0b013e31824eca94

146. Buckwalter JA, Glimcher MJ, Cooper RR, Recker R. Bone biology. Part I: Structure, blood supply, cells, matrix, and mineralization. *J Bone Jt Surg - Ser A*. 1995:1256-1275. doi:10.2106/00004623-199508000-00019

147. MARKSJR S, ODGREN P. Structure and Development of the Skeleton. In: *Principles of Bone Biology*. ; 2002:3-15. doi:10.1016/b978-012098652-1/50103-7

148. Keaveny TM, Morgan EF, Niebur GL, Yeh OC. Biomechanics of Trabecular Bone. *Annu Rev Biomed Eng*. 2001;3:307-333. doi:10.1146/annurev.bioeng.3.1.307

149. Cooper DML, Matyas JR, Katzenberg MA, Hallgrimsson B. Comparison of Microcomputed Tomographic and Microradiographic Measurements of Cortical Bone Porosity. *Calcif Tissue Int*. 2004. doi:10.1007/s00223-003-0071-z

150. Takahashi Y, Tabata Y. Effect of the fiber diameter and porosity of non-woven PET fabrics on the osteogenic differentiation of mesenchymal stem cells. *J Biomater Sci Polym Ed*. 2004;15(1):41-57. doi:10.1163/156856204322752228

151. Jin QM, Takita H, Kohgo T, Atsumi K, Itoh H, Kuboki Y. Effects of geometry of hydroxyapatite as a cell substratum in BMP- induced ectopic bone formation. *J Biomed Mater Res*. 2000;51(3):491-499. doi:10.1002/1097-4636(20000905)51:3<491::AID-JBM25>3.0.CO;2-1

152. Ahu Akin F, Zreiqat H, Jordan S, Wijesundara MBJ, Hanley L. Preparation and analysis of macroporous TiO2 films on Ti surfaces for bone-tissue implants. *J Biomed Mater Res*. 2001;57(4):588-596. doi:10.1002/1097-4636(20011215)57:4<588::AID-JBM1206>3.0.CO;2-Y

153. Akay G, Birch MA, Bokhari MA. Microcellular polyHIPE polymer supports osteoblast growth and bone formation in vitro. *Biomaterials*. 2004. doi:10.1016/j.biomaterials.2003.10.086

154. Hulbert SF, Young FA, Mathews RS, Klawitter JJ, Talbert CD, Stelling FH. Potential of ceramic materials as permanently implantable skeletal prostheses. *J Biomed Mater Res*. 1970;4(3):433-456. doi:10.1002/jbm.820040309

155. Xue W, Krishna BV, Bandyopadhyay A, Bose S. Processing and biocompatibility evaluation of laser processed porous titanium. *Acta Biomater*. 2007;3(6):1007-1018. doi:10.1016/j.actbio.2007.05.009

156. Otsuki B, Takemoto M, Fujibayashi S, Neo M, Kokubo T, Nakamura T. Pore throat size and connectivity determine bone and tissue ingrowth into porous implants: Three-dimensional micro-CT based structural analyses of porous bioactive titanium implants. *Biomaterials*. 2006;27(35):5892-5900. doi:10.1016/j.biomaterials.2006.08.013

157. Wang X, Jiang M, Zhou Z, Gou J, Hui D. 3D printing of polymer matrix composites: A review and prospective. *Compos Part B Eng*. 2017;110:442-458. doi:10.1016/j.compositesb.2016.11.034

158. Nikzad M, Masood SH, Sbarski I. Thermo-mechanical properties of a highly filled polymeric composites for Fused Deposition Modeling. *Mater Des*. 2011;32(6):3448-3456. doi:10.1016/j.matdes.2011.01.056

159. Gu J, Li N, Tian L, Lv Z, Zhang Q. High thermal conductivity graphite nanoplatelet/UHMWPE nanocomposites. *RSC Adv*. 2015;5(46):36334-36339. doi:10.1039/c5ra03284a

160. Zhong W, Li F, Zhang Z, Song L, Li Z. Short fiber reinforced composites for fused deposition modeling. *Mater Sci Eng A*. 2001;301(2):125-130. doi:10.1016/S0921-

5093(00)01810-4

161. Wang X, Yang H, Song L, Hu Y, Xing W, Lu H. Morphology, mechanical and thermal properties of graphene-reinforced poly(butylene succinate) nanocomposites. *Compos Sci Technol*. 2011. doi:10.1016/j.compscitech.2011.05.007

162. Guo B, Chen F, Lei Y, Liu X, Wan J, Jia D. Styrene-butadiene rubber/halloysite nanotubes nanocomposites modified by sorbic acid. *Appl Surf Sci*. 2009. doi:10.1016/j.apsusc.2009.03.092

163. Deng S, Zhang J, Ye L. Halloysite-epoxy nanocomposites with improved particle dispersion through ball mill homogenisation and chemical treatments. *Compos Sci Technol*. 2009;69:2497-2505. doi:10.1016/j.compscitech.2009.07.001

164. Jones AC, Arns CH, Sheppard AP, Hutmacher DW, Milthorpe BK, Knackstedt MA. Assessment of bone ingrowth into porous biomaterials using MICRO-CT. *Biomaterials*. 2007;28(15):2491-2504. doi:10.1016/j.biomaterials.2007.01.046

165. Shelton RM, Rasmussen AC, Davies JE. Protein adsorption at the interface between charged polymer substrata and migrating osteoblasts. *Biomaterials*. 1988;9:24-29. doi:10.1016/0142-9612(88)90065-8

166. van Wachem PB, Hogt AH, Beugeling T, et al. Adhesion of cultured human endothelial cells onto methacrylate polymers with varying surface wettability and charge. *Biomaterials*. 1987;8:323-328. doi:10.1016/0142-9612(87)90001-9

167. Chehroudi B, Gould TRL, Brunette DM. Titanium-coated micromachined grooves of different dimensions affect epithelial and connective-tissue cells differently in vivo. *J Biomed Mater Res*. 1990;24:1202-1219. doi:10.1002/jbm.820240906

168. Webb K, Hlady V, Tresco PA. Relative importance of surface wettability and charged functional groups on NIH 3T3 fibroblast attachment, spreading, and cytoskeletal organization. *J Biomed Mater Res*. 1998;41:422-430. doi:10.1002/(SICI)1097-4636(19980905)41:3<422::AID-JBM12>3.0.CO;2-K

169. Huang K, Ou Q, Xie Y, et al. Halloysite Nanotube Based Scaffold for Enhanced Bone Regeneration. *ACS Biomater Sci Eng*. 2019;5(8):4037-4047. doi:10.1021/acsbiomaterials.9b00277

170. Poshkus AC. Improved synthesis of basic zinc acetate, hexakis (. mu.-acetato)-. mu.-oxotetrazinc. *Ind Eng Chem Prod Res Dev*. 1983;22(2):380-381.

171. Peng H, Liu X, Tang W, Ma R. Facile synthesis and characterization of ZnO nanoparticles grown on halloysite nanotubes for enhanced photocatalytic properties. *Sci Rep*. 2017;7(1):2250.

172. Sparkes, Brian G. and DGM. Chitosan based wound dressing materials. *US Pat 4,572,906*. 1986;Feb 25. doi:10.1016/0375-6505(85)90011-2

173. Jayakumar R, Prabaharan M, Sudheesh Kumar PT, Nair S V., Tamura H. Biomaterials based on chitin and chitosan in wound dressing applications. *Biotechnol Adv*. 2011;29(3):322-337. doi:10.1016/j.biotechadv.2011.01.005

174. Bernkop-Schnürch A, Dünnhaupt S. Chitosan-based drug delivery systems. *Eur J Pharm Biopharm*. 2012;81(3):463-469. doi:10.1016/j.ejpb.2012.04.007

175. Bhattarai N, Gunn J, Zhang M. Chitosan-based hydrogels for controlled, localized drug delivery. *Adv Drug Deliv Rev*. 2010;62(1):83-99. doi:10.1016/j.addr.2009.07.019

176. Sun L, Mills DK. Halloysite nanotube-based drug delivery system for treating osteosarcoma. In: *2014 36th Annual International Conference of the IEEE Engineering in Medicine and Biology Society, EMBC 2014*. ; 2014:2920-2923. doi:10.1109/EMBC.2014.6944234

177. Abdullayev E, Joshi A, Wei W, Zhao Y, Lvov Y. Enlargement of halloysite clay nanotube lumen by selective etching of aluminum oxide. *ACS Nano*. 2012;6(8):7216-7226. doi:10.1021/nn302328x

178. Joshi A, Abdullayev E, Vasiliev A, Volkova O, Lvov Y. Interfacial modification of clay nanotubes for the sustained release of corrosion inhibitors. *Langmuir*. 2013;29(24):7439-7448. doi:10.1021/la3044973